University of Southampton

Photonic Crystal Modelling using Finite Element Analysis

Ben Hiett

A thesis submitted for the degree of Doctor of Philosophy

Faculty of Engineering and Applied Science
School of Engineering Sciences

December 2002

UNIVERSITY OF SOUTHAMPTON

ABSTRACT

FACULTY OF ENGINEERING AND APPLIED SCIENCES
SCHOOL OF ENGINEERING SCIENCES

Doctor of Philosophy

Photonic Crystal Modelling using Finite Element Analysis

By Ben Hiett

This thesis presents an efficient finite element method for computing spectra of photonic band gap materials. These periodic dielectric crystals exhibit a photonic band gap analogous to the electronic band gap present in semiconductors. Photons in the frequency range of the band gap are completely excluded so that atoms within such materials are unable to spontaneously absorb and re-emit light in this region. Photonic band gap devices offer enormous potential in the development of highly efficient narrow band lasers, integrated optical computing and high-speed optical communication networks, particularly in the production of purely optical circuits for dense wavelength division multiplexing.

Computational modelling of photonic band gap devices has traditionally been approached using plane wave expansion techniques. These have the disadvantages of being expensive in terms of computation and memory. By contrast, the finite element method is considerably more efficient since the eigensystem matrices are very sparse and the discontinuous dielectric constant is handled in real space. We have developed finite element software and used it to compute the band structure for a variety of common photonic crystal structures along with more novel structures such as the 12-fold symmetric quasicrystal.

We compare our results with those obtained from other sources, including plane wave expansion techniques, finite difference methods and experimental data. The performance of the algorithm is analysed in terms of memory and computational cost confirming the $O(n)$ problem scaling. Photonic band gap device optimisation is performed via multi-dimensional minimisation algorithms and the analysis of a canonical set of lattice arrangements. High-performance grid-enabled compute resources were utilised due to the computationally intensive nature of the process. This research has ascertained those crystal structures that produce the largest, most robust photonic band gaps with the best being the simple triangular lattice with a high filling fraction.

Acknowledgements

I would like to thank my supervisor, Professor Simon Cox, for his constructive input and support. I would also like to thank a number of other people who have contributed to this work including Dr. J. M. Generowicz, Dr. K. S. Thomas, Mr. M. Molinari and Mr. D. H. Beckett. I am also grateful for the assistance of Dr. M. E. Zoorob and Dr. M. D. B. Charlton from the microelectronics group. I would also like to express my gratitude towards EPSRC and the Department of Electronics and Computer Science, University of Southampton, for funding this work.

Contents

ABSTRACT II

ACKNOWLEDGEMENTS III

AUTHOR'S DECLARATION IV

1 INTRODUCTION 1

1.1 PHOTONIC CRYSTALS – AN OVERVIEW 1

1.2 PHYSICS OVERVIEW 4

1.3 FINITE ELEMENT OVERVIEW 6

1.4 CONTRIBUTIONS 8

1.5 OUTLINE OF THESIS 10

2 THE FINITE ELEMENT METHOD 12

2.1 DOMAIN DISCRETISATION 12

2.2 INTERPOLATION FUNCTIONS 13

2.3 GOVERNING MATHEMATICAL EQUATIONS 16

2.4 TWO-DIMENSIONAL SCALAR CASE 17

2.5 THREE-DIMENSIONAL VECTOR CASE 19

2.6 CURL-CONFORMING ELEMENTS 21

2.7 MAXWELL VECTOR WAVE EQUATION 24

2.8 APPROXIMATION OF THE DIFFERENTIAL EQUATION 25

2.9 ASSEMBLY OF THE SYSTEM OF EQUATIONS 27

2.10 RECIPROCAL LATTICE SPACE AND THE BRILLOUIN ZONE 29

2.11 SOLUTION OF THE SYSTEM OF EQUATIONS 33

2.12 DATA VISUALISATION 34

2.13 COMMENTS ON THE FEM 37

3 RESULTS 41

3.1 COMPARISON WITH ANALYTICAL RESULTS 41
3.2 COMPARISON WITH NUMERICAL RESULTS 42
3.3 COMPARISON WITH EXPERIMENTAL RESULTS 49
3.4 BAND GAP MAPS 50
3.5 THREE DIMENSIONAL FE ANALYSIS 52
3.6 FREE-SPACE PROPAGATION AT THE GAMMA POINT 53
3.7 FABRICATION CONSTRAINTS 59

4 PERFORMANCE 64

4.1 ACCURACY AND CONVERGENCE 64
4.2 OPTIMISING 2D ALGORITHM PERFORMANCE 65
4.3 OBJECT-ORIENTED SOFTWARE APPROACH 69
4.4 CLASSES AND INTERFACES 70
4.5 COMPUTING RESOURCES 72
4.6 IRIDIS: THE BEOWULF CLUSTER 72
4.7 IRIDIS: THE WINDOWS CONDOR CLUSTER 73
4.8 DGL: THE BEOWULF CLUSTER 73

5 12-FOLD SYMMETRIC PHOTONIC QUASICRYSTALS 75

5.1 QUASICRYSTAL CONFIGURATIONS 75
5.2 RESULTS 76
5.3 INTRODUCTION OF CRYSTAL DEFECTS 82
5.4 CONCLUSIONS 83

6 PHOTONIC CRYSTAL DESIGN OPTIMISATION 84

6.1 AUTOMATED MESH GENERATION 84
6.2 EIGENVALUE ANALYSIS 87
6.3 FUNCTION MINIMISATION: THE DOWNHILL SIMPLEX METHOD 87
6.4 PBG DEVICE OPTIMISATION: BRUTE FORCE APPROACH 90

6.5 PBG DEVICE OPTIMISATION: CANONICAL FORMS APPROACH 94
6.6 OPTIMISATION FOR A HOMOGENEOUS FILLING FRACTION 101
6.7 CONCLUSION 102

7 CONCLUSION 104

7.1 SUMMARY 104
7.2 FUTURE WORK 112

REFERENCES 113

APPENDIX A: GALERKIN'S METHOD 119

APPENDIX B: SIMPLEX ELEMENTS 121

B.1 SIMPLEX COORDINATES 121
B.2 2-DIMENSIONAL CARTESIAN-SIMPLEX CONVERSION 122
B.3 3-DIMENSIONAL CARTESIAN-SIMPLEX CONVERSION 123
B.4 DIFFERENTIATION IN SIMPLEX COORDINATES 124
B.5 INTEGRATION IN SIMPLEX COORDINATES 125

APPENDIX C: 2D ELEMENTAL MATRICES 128

C.1 DERIVATION OF $\int_{\Omega} \alpha_m \alpha_n d\Omega$ 128
C.2 DERIVATION OF $\int_{\Omega} \nabla \alpha_m . \nabla \alpha_n d\Omega$ 129
C.3 DERIVATION OF $\int_{\Omega} \alpha_m \nabla \alpha_n d\Omega$ 131

APPENDIX D: ANALYTICAL SOLUTION IN FREE-SPACE 134

APPENDIX E: THE LEVI-CIVITA TENSOR 135

APPENDIX F: 3D ELEMENTAL MATRICES 136

F.1 DERIVATION OF $\int_{\Omega} (\nabla \times \mathbf{N}_i) \cdot (\nabla \times \mathbf{N}_j) d\Omega$ 137
F.2 DERIVATION OF $\int_{\Omega} \mathbf{N}_i \cdot \mathbf{N}_j d\Omega$ 138

F.3 DERIVATION OF $\int_{\Omega}\left(\mathbf{N}_i \times \nabla \times \mathbf{N}_j\right) - \left(\mathbf{N}_j \times \nabla \times \mathbf{N}_i\right) d\Omega$ 138

F.4 DERIVATION OF $\int_{\Omega}\left(\mathbf{k} \cdot \mathbf{N}_i\right)\left(\mathbf{k} \cdot \mathbf{N}_j\right) d\Omega$ 139

APPENDIX G: FEMLIB CLASS DIAGRAMS 141

List of Tables

TABLE 2-1 EDGE TO VERTEX MAPPING FOR A TETRAHEDRAL ELEMENT. 22
TABLE 2-2 LOCAL TO GLOBAL NODE MAP 28
TABLE 3-1 THE VALUES OF λ (RECIPROCAL LATTICE VECTOR MAGNITUDE SQUARED) AND THE NUMBER OF TIMES, N, THAT VALUE OCCURS 54
TABLE 3-2 THE VALUES OF λ (RECIPROCAL LATTICE VECTOR MAGNITUDE SQUARED) AND THE NUMBER OF TIMES, N, THAT VALUE OCCURS 56
TABLE 3-3 THE PROBABILITY OF A TRIANGULAR LATTICE PHOTONIC CRYSTAL EXHIBITING A PHOTONIC BAND GAP FOR A GIVEN RELATIVE ERROR IN THE ROD RADIUS. 62
TABLE 6-1 BAND-GAP OPTIMISATION RESULTS FOR THE TOP TWENTY MESHES. 91
TABLE 6-2 OPTIMISATION DATA FOR THE TOP-TEN CANONICAL FORMS. 97
TABLE 6-3 THE SET OF RANDOMLY GENERATED MESHES THAT EXHIBIT A PHOTONIC BAND GAP GROUPED INTO THOSE OF EQUAL FILLING FRACTION. 101
TABLE B-1 3-DIMENSIONAL SIMPLEX COORDINATE COEFFICIENTS 123

List of Figures

FIGURE 1-1 PHOTO OF A PHOTONIC CRYSTAL – COURTESY OF MARTIN CHARLTON ET AL (SOUTHAMPTON MICROELECTRONICS RESEARCH GROUP). 2
FIGURE 1-2 COMPUTATIONAL MODELLING OF PHOTONIC CRYSTALS. 2
FIGURE 1-3 BREAKDOWN OF THE FINITE ELEMENT METHOD. 7
FIGURE 2-1 PERIODIC DOMAIN DISCRETISATION EXAMPLES IN TWO DIMENSIONS (A) AND THREE DIMENSIONS (B). 12
FIGURE 2-2 UNIT CELL (A); PERIODIC TILING (B), SHOWING 9 UNIT-CELLS TILED TOGETHER. 13
FIGURE 2-3 TRIANGULAR ELEMENT WITH CUBIC INTERPOLATION. 14
FIGURE 2-4 TETRAHEDRAL ELEMENT WITH QUADRATIC INTERPOLATION. 15
FIGURE 2-5 LINEAR AND QUADRATIC INTERPOLATION FUNCTIONS. 16
FIGURE 2-6 A CURL-CONFORMING VECTOR INTERPOLATION FUNCTION. 21
FIGURE 2-7 EDGE AND VERTEX DEFINITION FOR A TETRAHEDRAL ELEMENT. 23
FIGURE 2-8 GLOBAL AND LOCAL NODE NUMBERING. 28
FIGURE 2-9 LOCAL TO GLOBAL MATRIX ELEMENTS. 29
FIGURE 2-10 A TWO-DIMENSIONAL CRYSTAL LATTICE (A) AND THE CORRESPONDING UNIT CELL (B). THE LATTICE VECTORS, $\mathbf{A}_1$ AND $\mathbf{A}_2$ ARE HIGHLIGHTED WITH ARROWS. 29
FIGURE 2-11 LATTICE VECTORS IN REAL SPACE (A) AND RECIPROCAL LATTICE SPACE (B). THE DIRECTION AND MAGNITUDE OF THE RECIPROCAL LATTICE VECTORS ARE GOVERNED BY EQUATIONS (2.50) AND (2.51) RESPECTIVELY. 30
FIGURE 2-12 BRILLOUIN ZONE CONSTRUCTION FOR A TRIANGULAR LATTICE (A) DIMENSIONS OF THE BRILLOUIN ZONE IN TERMS OF THE REAL-SPACE LATTICE PITCH LENGTH (B). THE 1ST BRILLOUIN ZONE IS HIGHLIGHTED IN GREY WITH THE IRREDUCIBLE BRILLOUIN ZONE CROSS-HATCHED. 31
FIGURE 2-13 A SOBOL SEQUENCE; A QUASI-RANDOM DISTRIBUTION OF POINTS (A) AND THE LINKING OF ADJACENT POINTS HIGHLIGHTING THEIR CLOSE PROXIMITY (B). 33
FIGURE 2-14 EXAMPLE OF A BAND DIAGRAM FOR A PHOTONIC CRYSTAL. THE FREQUENCY RANGE THAT NONE OF THE BANDS INTERSECT IS HIGHLIGHTED, THIS REPRESENTS A PHOTONIC BAND GAP. 35
FIGURE 2-15 EXAMPLE OF A DENSITY OF STATES DIAGRAM FOR A PHOTONIC CRYSTAL. THE FREQUENCY RANGE FOR WHICH THE DENSITY OF STATES DROPS TO ZERO REPRESENTS A PHOTONIC BAND GAP. 36

FIGURE 2-16 EXAMPLE GAP-MAP FOR A TRIANGULAR LATTICE PLOTTING THE BAND-GAP FREQUENCY RANGES FOR BOTH THE TE(DASHED) AND TM (SOLID) MODES AGAINST THE ROD RADIUS. 36
FIGURE 2-17 EXAMPLE OF A FIELD INTENSITY PLOT. THE MAGNITUDE OF THE FIELD IS PLOTTED AT MESH NODE POINTS 37
FIGURE 2-18 SPARSE GLOBAL MATRIX: 800 X 800 = 640, 000 ELEMENTS. 12460 NON-ZERO ELEMENTS GIVES A SPARSITY OF APPROXIMATELY 2% 39
FIGURE 2-19 H-REFINEMENT FOR A TRIANGULAR LATTICE UNIT CELL. MESH (A) IS COMPOSED OF 200 ELEMENTS, MESH (B) IS COMPOSED OF 1000 ELEMENTS. 39
FIGURE 3-1 UNSTRUCTURED TRIANGULAR MESH REPRESENTATION OF A SQUARE FREE-SPACE UNIT-CELL 41
FIGURE 3-2 ANALYTICAL, (A), AND FINITE ELEMENT, (B), FREE-SPACE BAND DIAGRAMS 42
FIGURE 3-3 A TYPICAL TWO-DIMENSIONAL PHOTONIC CRYSTAL STRUCTURE CONSISTING OF CYLINDRICAL RODS ARRANGED PERIODICALLY IN A SUBSTRATE MATERIAL. 43
FIGURE 3-4 SQUARE LATTICE ROD ARRANGEMENT (A) AND THE SQUARE LATTICE GEOMETRY (B). SINGLE (C) AND TILED (D) UNIT-CELLS FOR A SQUARE CRYSTAL LATTICE OF RODS IN A SUBSTRATE MATERIAL 44
FIGURE 3-5 PHOTONIC BAND STRUCTURES PRODUCED BY (A) THE FINITE ELEMENT CODE CODE WITH THE SOLID AND DASHED LINES REPRESENTING THE TM AND TE MODES RESPECTIVELY AND (B) REPRODUCED COURTESY OF JOANNOPOULUS ET AL. FOR A SQUARE LATTICE ARRANGEMENT OF ALUMINA RODS (ε=8.9) IN AIR WITH A RELATIVE ROD RADIUS, R/A, OF 0.2. 44
FIGURE 3-6 TRIANGULAR LATTICE ROD ARRANGEMENT (A) AND THE TRIANGULAR LATTICE GEOMETRY (B). SINGLE (C) AND TILED (D) UNIT-CELLS FOR A TRIANGULAR CRYSTAL LATTICE OF RODS IN A SUBSTRATE MATERIAL. 45
FIGURE 3-7 PHOTONIC BAND STRUCTURES PRODUCED BY (A) THE FINITE ELEMENT CODE WITH THE SOLID AND DASHED LINES REPRESENTING THE TM AND TE MODES RESPECTIVELY AND (B) REPRODUCED COURTESY OF JOANNOPOULUS ET AL. FOR A TRIANGULAR LATTICE ARRANGEMENT OF AIR RODS WITH A RELATIVE RADIUS, R/A, OF 0.48 IN A SUBSTRATE MATERIAL, ε=13. 46
FIGURE 3-8 FINITE ELEMENT ANALYSIS (A) AND PLANE WAVE ANALYSIS COURTESY OF VILLENEUVE ET AL. (B) OF A TRIANGULAR LATTICE OF AIR RODS (FILLING FRACTION = 80%) SET IN A SUBSTRATE WITH A REFRACTIVE INDEX OF 3.5. THE SOLID AND DASHED LINES REPRESENT THE TM AND TE MODES RESPECTIVELY. 46

FIGURE 3-9 BAND DIAGRAM FOR A TRIANGULAR LATTICE OF AIR RODS IN SILICON NITRIDE, DIELECTRIC CONSTANT = 4.0804, FILLING FRACTION = 30%. 47

FIGURE 3-10 (A) SQUARE ARRAY OR 'WOODPILE' PHOTONIC CRYSTAL STRUCTURE; A SQUARE GRID OF DIELECTRIC VEINS IS SET IN A SUBSTRATE MATERIAL. (B) THE UNIT CELL MESH REPRESENTATION AND (C) AN EXAMPLE OF 4 UNIT CELLS TILED PERIODICALLY. 48

FIGURE 3-11 PHOTONIC BAND STRUCTURES PRODUCED BY (A) THE FINITE ELEMENT CODE WITH THE SOLID AND DASHED LINES REPRESENTING THE TM AND TE MODES RESPECTIVELY AND (B) REPRODUCED COURTESY OF JOANNOPOULUS ET AL. FOR A SQUARE GRID LATTICE OF ALUMINA (=8.9) IN AIR, FILLING FRACTION EQUALS 36%. 48

FIGURE 3-12 EXAMPLE OF A TRIANGULAR LATTICE OF AIR RODS IN A HIGH DIELECTRIC CONSTANT SUBSTRATE. NOTE THE HIGHLIGHTED AREAS OF HIGH DIELECTRIC CONSTANT (SHADED RED) CONNECTED BY NARROW VEINS OF SUBSTRATE MATERIAL (HIGHLIGHTED GREEN). 49

FIGURE 3-13 BRIDGE WAVEGUIDE STRUCTURE (PITCH=300NM) COURTESY OF MARTIN CHARLTON, SOUTHAMPTON MICROELECTRONICS RESEARCH GROUP 50

FIGURE 3-14 (A) TRANSMISSION DIAGRAM FOR A TRIANGULAR LATTICE PC CONSISTING OF AIR RODS IN A GAAS SUBSTRATE WITH A FILLING FRACTION OF 80%. (B) FEM ANALYSIS OF THE SAME STRUCTURE. A TRIANGULAR LATTICE UNIT CELL MESH OF CIRCULAR RODS WAS USED. THE ROD MATERIAL WAS AIR (ε=1) AND THE SUBSTRATE MATERIAL WAS GAAS (ε=11.4). 50

FIGURE 3-15 BAND GAP MAPS FOR PHOTONIC CRYSTAL STRUCTURES: (A) SQUARE LATTICE OF GAAS RODS IN AIR (B) SQUARE LATTICE OF AIR RODS IN A GAAS SUBSTRATE (C) TRIANGULAR LATTICE OF GAAS RODS IN AIR (D) TRIANGULAR LATTICE OF AIR RODS IN A GAAS SUBSTRATE. TE POLARISATION BAND GAPS ARE HIGHLIGHTED IN RED, TM POLARISATION BAND GAPS ARE HIGHLIGHTED IN BLUE AND COMPLETE BAND GAPS ARE HIGHLIGHTED IN YELLOW. 52

FIGURE 3-16 THE FIRST 20 **G**-VECTORS IN RECIPROCAL LATTICE SPACE CORRESPONDING TO A SQUARE UNIT-CELL REPRESENTATION OF FREE-SPACE. 54

FIGURE 3-17 A PLOT OF THE LOWEST 30 EIGENVALUES (A) COMPUTED FOR FREE-SPACE AT THE GAMMA POINT (**K** = [0 0]) AND THE CORRESPONDING MESH REPRESENTATION OF FREESPACE (B). 55

FIGURE 3-18 RECIPROCAL LATTICE SPACE FOR A CUBIC UNIT CELL. (A) REPRESENTS THE FIRST 6 RECIPROCAL LATTICE VECTORS OF EQUAL MAGNITUDE (B) REPRESENTS THE NEXT 12 RECIPROCAL LATTICE VECTORS OF EQUAL MAGNITUDE. 56

FIGURE 3-19 PLOT OF THE ANALYTICAL SOLUTION AT THE GAMMA-POINT FOR FREE-SPACE IN THREE-DIMENSIONS. 57
FIGURE 3-20 A PLOT OF THE LOWEST 74 EIGENVALUES, (A), FOR A THREE-DIMENSIONAL MESH REPRESENTATION OF FREE-SPACE CONSISTING OF 106 VERTICES AND 310 TETRAHEDRAL ELEMENTS, (B). 58
FIGURE 3-21 A PLOT OF THE LOWEST 195 EIGENVALUES, (A), FOR A THREE-DIMENSIONAL MESH REPRESENTATION OF FREE-SPACE CONSISTING OF 225 VERTICES AND 822 TETRAHEDRAL ELEMENTS, (B). 58
FIGURE 3-22 A PLOT OF THE LOWEST 230 EIGENVALUES, (A), FOR A THREE-DIMENSIONAL MESH REPRESENTATION OF FREE-SPACE CONSISTING OF 260 VERTICES AND 958 TETRAHEDRAL ELEMENTS, (B). 59
FIGURE 3-23 THE ERROR ASSOCIATED WITH(A) THE ROD RADIUS AND (B) THE ROD POSITION. 60
FIGURE 3-24 A RHOMBIC UNIT-CELL CONTAINING NINE RODS. THE RADIUS OF THESE RODS VARY RANDOMLY WITHIN A PRESCRIBED PERCENTAGE ERROR CONSTRAINT. 61
FIGURE 3-25 A PLOT OF THE UPPER AND LOWER BOUNDS OF THE BAND GAP AGAINST THE RELATIVE ERROR IN THE ROD RADIUS. THE ERROR BARS REPRESENT ONE STANDARD DEVIATION EITHER SIDE OF THE MEAN. 61
FIGURE 3-26 THE NORMAL DISTRIBUTIONS OF THE POSITIONS OF THE LOWER (RED) AND UPPER (BLUE) BOUNDS OF THE PHOTONIC BAND GAP FREQUENCY RANGE FOR A RELATIVE ERROR IN THE ROD RADIUS OF (A) 1 % AND (B) 5 %. 62
FIGURE 3-27 PROBABILITY OF THE PHOTONIC CRYSTAL EXHIBITING A BAND GAP FOR VARIOUS RELATIVE ERRORS IN THE ROD POSITION. EACH LINE CORRESPONDS TO A DIFFERENT RELATIVE ERROR IN THE ROD RADIUS AS EXPLAINED IN THE LEGEND. 63
FIGURE 4-1 CONVERGENCE OF THE FEM FOR FREE-SPACE. THE MAXIMUM RELATIVE ERRORS FOR THE LOWEST 9 EIGENVALUES ARE PLOTTED AGAINST MESH GRANULARITY. 64
FIGURE 4-2 CONVERGENCE OF THE FEM FOR A TRIANGULAR LATTICE. THE MAXIMUM RELATIVE ERRORS FOR THE LOWEST NINE EIGENVALUES ARE PLOTTED AGAINST MESH GRANULARITY. 65
FIGURE 4-3 COMPARISON OF COMPUTATION TIME WITH MESH SIZE (NO. OF ELEMENTS) FOR INTERPOLATION ORDERS ONE TO FOUR. 66
FIGURE 4-4 COMPARISON OF NO. OF NON ZERO MATRIX VALUES WITH MESH SIZE (NO. OF ELEMENTS) FOR INTERPOLATION ORDERS ONE TO FOUR. 67
FIGURE 4-5 COMPARISON OF RELATIVE ERROR WITH THE NO. OF NON ZERO MATRIX VALUES FOR INTERPOLATION ORDERS ONE TO FOUR. 68

FIGURE 4-6 COMPARISON OF RELATIVE ERROR WITH COMPUTATION TIME FOR INTERPOLATION ORDERS ONE TO FOUR. 68
FIGURE 4-7 FEM CLASS STRUCTURE. 70
FIGURE 4-8 POINTER BASED MESH STORAGE STRUCTURE. 71
FIGURE 4-9 PERIODIC BOUNDARY CONDITIONS. 71
FIGURE 5-1 12-FOLD SYMMETRIC QUASICRYSTAL CONFIGURATIONS: (A) 'TRIANGLE-TRIANGLE' AND (B) 'SQUARE-SQUARE'. 75
FIGURE 5-2 UNSTRUCTURED TRIANGULAR MESH REPRESENTATIONS OF THE RHOMBIC UNIT-CELLS: (A) 'TRIANGLE-TRIANGLE' AND (B) 'SQUARE-SQUARE' CONFIGURATIONS. 76
FIGURE 5-3 THE IRREDUCIBLE BRILLOUIN ZONE PATH, $K \rightarrow \Gamma \rightarrow X \rightarrow K$, USED IN THE ANALYSIS OF THE QUASICRYSTAL PHOTONIC BAND-GAP DEVICES. 76
FIGURE 5-4 DISPERSION RELATIONS FOR: (A) 'TRIANGLE-TRIANGLE' CONFIGURATION OF AIR RODS IN SIN SUBSTRATE; (B) 'TRIANGLE-TRIANGLE' CONFIGURATION OF AIR RODS IN A GAAS SUBSTRATE; (C) 'SQUARE-SQUARE' CONFIGURATION OF AIR RODS IN SIN; (D) 'SQUARE-SQUARE' CONFIGURATION OF AIR RODS IN A GAAS SUBSTRATE. R/A = 0.5 FOR ALL CRYSTALS. THE SOLID AND BROKEN CURVES CORRESPOND TO THE TRANSVERSE ELECTRIC (TE) AND TRANSVERSE MAGNETIC (TM) POLARISATIONS RESPECTIVELY. 77
FIGURE 5-5 DENSITY OF STATES DIAGRAMS FOR TRIANGLE-TRIANGLE (A) AND SQUARE-SQUARE (B) QUASICRYSTAL CONFIGURATIONS. AIR RODS IN A GALLIUM ARSENIDE SUBSTRATE, DIELECTRIC CONSTANT = 11.4, R/A=0.3. THE SOLID AND BROKEN CURVES CORRESPOND TO THE TRANSVERSE ELECTRIC (TE) AND TRANSVERSE MAGNETIC (TM) POLARISATIONS RESPECTIVELY. 78
FIGURE 5-6 DENSITY OF STATES DIAGRAMS FOR A TRIANGLE-TRIANGLE QUASICRYSTAL CONFIGURATION WITH R/A = 0.3: (A) SUBSTRATE DIELECTRIC CONSTANT = 4.1 (SILICON NITRIDE) (B) SUBSTRATE DIELECTRIC CONSTANT = 2.1 (GLASS). 79
FIGURE 5-7 DENSITY OF STATES DIAGRAMS FOR (A) AIR-RODS IN A SUBSTRATE MATERIAL OF DIELECTRIC CONSTANT = 8.9, R/A = 0.47 (B) AIR-RODS IN A SUBSTRATE MATERIAL OF DIELECTRIC CONSTANT = 11.4, R/A =0.40. 80
FIGURE 5-8 GAP-MAPS FOR VARIOUS QUASICRYSTALS: (A) 'TRIANGLE-TRIANGLE' CONFIGURATION OF AIR RODS IN SIN. (B) 'TRIANGLE-TRIANGLE' CONFIGURATION OF AIR RODS IN GAAS, (C) 'SQUARE-SQUARE' CONFIGURATION OF AIR RODS IN GAAS. (D) 'TRIANGLE-TRIANGLE' CONFIGURATION OF GAAS RODS IN AIR. THE FILLING FRACTION IS EXPRESSED AS THE RATIO OF ROD RADIUS TO THE PITCH (R/A). 81
FIGURE 5-9 COMPARISON OF RESULTS FOR A 'TRIANGLE-TRIANGLE' CONFIGURATION QUASICRYSTAL OF AIR RODS IN SILICON NITRIDE, FILLING FRACTION = 30%. (A) FINITE

ELEMENT METHOD, (B) FINITE DIFFERENCE TIME DOMAIN COURTESY OF MAJD ZOOROB, (C) EXPERIMENTAL DATA COURTESY OF MARTIN CHARLTON, CATERINA NETTI, GREG PARKER AND JEREMY BAUMBERG, ECS AND PHYSICS DEPT. UNIVERSITY OF SOUTHAMPTON. 82

FIGURE 5-10 QUASICRYSTAL WITH A CENTRAL ROD DEFECT; MESH AND DENSITY OF STATES DIAGRAM; R/A = 0.3, SUBSTRATE DIELECTRIC CONSTANT = 11.4. 83

FIGURE 6-1 EXAMPLE PHOTONIC CRYSTAL GEOMETRY DEFINITION FILE. 85

FIGURE 6-2 IMPOSITION OF PERIODIC BOUNDARY CONDITIONS UPON THE PHOTONIC CRYSTAL STRUCTURE. 85

FIGURE 6-3 POINT BASED REPRESENTATION OF THE CRYSTAL STRUCTURE AND SUBSEQUENT UNSTRUCTURED TRIANGULAR MESH BASED REPRESENTATION OF THE STRUCTURE. 86

FIGURE 6-4 SCHEMATIC OF THE PHOTONIC CRYSTAL OPTIMISATION PROCESS. 89

FIGURE 6-5 OPTIMISATION RESULTS FOR THE RANDOMLY GENERATED MESH, QUASI_MESH_1_1.7_1. THE DENSITY OF STATES IS PLOTTED FOR THE CRYSTAL BEFORE OPTIMISATION (A) AND AFTER OPTIMISATION (B). THE CONVERGENCE OF THE MINIMISATION ALGORITHM IS SHOWN BY PLOTTING THE BAND-GAP TO MID-GAP RATIO AGAINST THE NUMBER OF ITERATIONS (C). THE INITIAL (ABOVE) AND FINAL (BELOW) MESHES ARE SHOWN IN (D). 92

FIGURE 6-6 OPTIMISATION RESULTS FOR THE RANDOMLY GENERATED MESH, QUASI_MESH_3_1_9. THE DENSITY OF STATES IS PLOTTED FOR THE CRYSTAL BEFORE OPTIMISATION (A) AND AFTER OPTIMISATION (B). THE CONVERGENCE OF THE MINIMISATION ALGORITHM IS SHOWN BY PLOTTING THE BAND-GAP TO MID-GAP RATIO AGAINST THE NUMBER OF ITERATIONS (C). THE INITIAL (ABOVE) AND FINAL (BELOW) MESHES ARE SHOWN IN (D). 93

FIGURE 6-7 OPTIMISATION RESULTS FOR THE RANDOMLY GENERATED MESH, QUASI_MESH_3_1_12. THE DENSITY OF STATES IS PLOTTED FOR THE CRYSTAL BEFORE OPTIMISATION (A) AND AFTER OPTIMISATION (B). THE CONVERGENCE OF THE MINIMISATION ALGORITHM IS SHOWN BY PLOTTING THE BAND-GAP TO MID-GAP RATIO AGAINST THE NUMBER OF ITERATIONS (C). THE INITIAL (ABOVE) AND FINAL (BELOW) MESHES ARE SHOWN IN (D). 94

FIGURE 6-8 EXAMPLES OF THE TYPES OF PERIODIC DOT PATTERNS, REPRODUCED COURTESY OF (GRÜNBAUM AND SHEPHARD 1987) 96

FIGURE 6-9 GAP-MAPS FOR (A) DPS11 AND (B) DPP27 CANONICAL FORMS. THE VERTICAL DASHED LINES REPRESENT THE MAXIMUM ROD RADIUS BEFORE THE RODS OVERLAP AND THE SUBSTRATE BECOMES DISCONNECTED. 97

FIGURE 6-10 OPTIMISATION DATA FOR CANONICAL FROM DPS11. THE DENSITY OF STATES IS PLOTTED FOR THE CRYSTAL BEFORE OPTIMISATION (A) AND AFTER OPTIMISATION (B). THE CONVERGENCE OF THE MINIMISATION ALGORITHM IS SHOWN BY PLOTTING THE BAND-GAP TO MID-GAP RATIO AGAINST THE NUMBER OF ITERATIONS (C). THE INITIAL (ABOVE) AND FINAL (BELOW) MESHES ARE SHOWN IN (D). 98

FIGURE 6-11 OPTIMISATION DATA FOR CANONICAL FROM DPP47. THE DENSITY OF STATES IS PLOTTED FOR THE CRYSTAL BEFORE OPTIMISATION (A) AND AFTER OPTIMISATION (B). THE CONVERGENCE OF THE MINIMISATION ALGORITHM IS SHOWN BY PLOTTING THE BAND-GAP TO MID-GAP RATIO AGAINST THE NUMBER OF ITERATIONS (C). THE INITIAL (ABOVE) AND FINAL (BELOW) MESHES ARE SHOWN IN (D). 99

FIGURE 6-12 OPTIMISATION DATA FOR CANONICAL FROM DPP27. THE DENSITY OF STATES IS PLOTTED FOR THE CRYSTAL BEFORE OPTIMISATION (A) AND AFTER OPTIMISATION (B). THE CONVERGENCE OF THE MINIMISATION ALGORITHM IS SHOWN BY PLOTTING THE BAND-GAP TO MID-GAP RATIO AGAINST THE NUMBER OF ITERATIONS (C). THE INITIAL (ABOVE) AND FINAL (BELOW) MESHES ARE SHOWN IN (D). 100

FIGURE 6-13 THE THREE MESHES EXHIBITING THE LARGEST BAND GAPS FOR 4 RODS IN A RHOMBIC UNIT CELL WITH A FILLING FRACTION OF 0.46; (A) MESH 70: $\Delta\omega/\omega 0 = 0.0108$, (B) MESH 26: $\Delta\omega/\omega 0 = 0.0097$, (C) 43: $\Delta\omega/\omega 0 = 0.0096$. 102

FIGURE 6-14 THE THREE MESHES EXHIBITING THE LARGEST BAND GAPS FOR 4 RODS IN A RHOMBIC UNIT CELL WITH A FILLING FRACTION OF 0.51; (A) MESH 88: $\Delta\omega/\omega 0 = 0.0279$, (B) MESH 60: $\Delta\omega/\omega 0 = 0.0272$, (C) 7: $\Delta\omega/\omega 0 = 0.0235$. 102

FIGURE 6-15 THE THREE MESHES EXHIBITING THE LARGEST BAND GAPS FOR 7 RODS IN A RHOMBIC UNIT CELL WITH A FILLING FRACTION OF 0.67; (A) MESH 1: $\Delta\omega/\omega 0 = 0.0630$, (B) MESH 6: $\Delta\omega/\omega 0 = 0.0417$, (C) 4: $\Delta\omega/\omega 0 = 0.0328$. 102

FIGURE B-1 N-DIMENSIONAL SIMPLEX ELEMENTS. 121

FIGURE B-2 SIMPLEX COORDINATES. 121

1 Introduction

1.1 Photonic Crystals – An Overview

Photonic Band Gap (PBG) Structures exhibit a photonic band gap analogous to the electronic band gap present in semiconductors. A band gap arises due to destructive interference from Bragg like diffraction of waves through the crystal. Photons in the frequency range of the band gap are completely excluded so that atoms within such materials are unable to spontaneously absorb and re-emit light in this region (Yablonovitch 1987) (Yablonovitch 1993). The electric permittivity of a PBG structure varies periodically on a scale comparable to the wavelength of the forbidden photons. Figure 1-1 is a photo of a photonic crystal (PC); note the periodic structure with the rods and cavities having different dielectric constants.

PBG devices offer enormous potential in the development of sharp angle wave guiding, highly efficient single mode lasers, integrated optical computing and high-speed optical communication networks, particularly in the production of purely optical circuits for DWDM (Dense Wavelength Division Multiplexing) (Parker and Charlton 2000) (Yablonovitch 2000). The construction of integrated optical circuits would allow the revolutionary shift from optoelectronic to photonic technology to take place (Yablonovitch 1994). This step is widely viewed as the 'holy grail' in communication technology.

Manufacturing PBG materials that operate in the visible region of the electromagnetic spectrum requires fabrication techniques with a resolution of approximately 5 nm. This is both time consuming and expensive, especially when precise control over the variation in permittivity is required. Hence, it is vital that one can accurately and efficiently model such structures; this allows investigation and optimisation of PBG structures to be performed while keeping manufacturing costs to a minimum. We have developed a library of Finite Element Method (FEM) code to compute the electromagnetic modes of propagation in these structures.

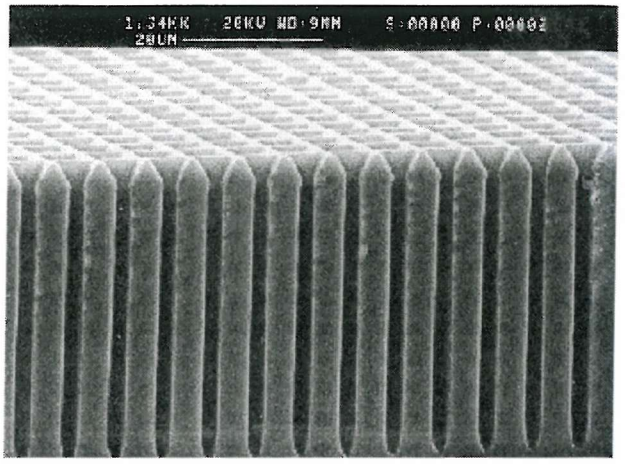

Figure 1-1 Photo of a photonic crystal – courtesy of Martin Charlton et al (Southampton microelectronics research group).

The propagation of light in a photonic crystal is governed by the geometry and permittivity of its constituent dielectric materials. Hence, in order to model a crystal's optical properties, a numerical method is needed as illustrated in Figure 1-2. Traditionally, plane wave expansion has been used as the numerical method (Villeneuve and Piche 1994); this approach has produced successful results but has disadvantages such as slow convergence and high demands for computing power and memory (Villeneuve and Piche 1991). Finite Difference (FD) methods have also been employed with the benefit of yielding transmission information but they generally require structured meshes and produce a discrete rather than continuous solution over the problem domain. A comprehensive review of these methods is provided by (Taflove and Hagness 2000).

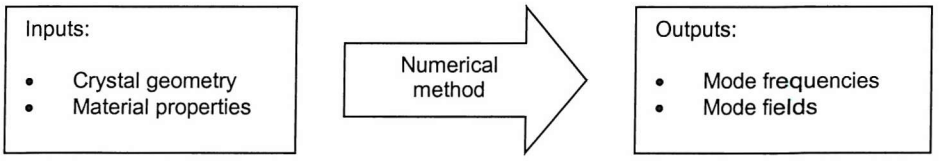

Figure 1-2 Computational modelling of photonic crystals.

The use of finite elements as the numerical method addresses these problems. The finite element formulation gives rise to eigensystems described by sparse matrices; this leads to significant reductions in processor and memory requirements over the dense matrices produced using plane wave techniques. The sharp discontinuities in dielectric constant characteristic of many PBG materials are easily and more importantly exactly represented using the finite element method whereas plane wave techniques suffer from Gibb's phenomena at material boundaries. The

unstructured mesh representation of the crystal structure simplifies the construction of regions of arbitrary shape and also simplifies the application of adaptive mesh refinement allowing concentration of computational resources on key regions of the domain. The advantages of finite elements are discussed in further detail in chapter 2.13.

Various commercial software packages are available for performing photonic crystal analysis. These are typically less specialised and capable of modelling a range of devices all under the umbrella of computational electromagnetics. Ansoft's HFSS (Ansoft 2002) offers second order vector finite elements for modelling complex geometries in radio frequency and optoelectronic design. The package includes a visual mesh development environment, adaptive mesh refinement and solution visualisation. However, whilst it has a number of features that make it well suited to PC modelling (Remski 2000), it is not specifically targeted at PBG devices and generating, for example, a density of states graph requires results from a number of different simulations to be combined. This makes it less efficient than code targeted directly at this problem, which may incorporate the optimisations described in this thesis. Concerto (VectorFields 2002) incorporates a finite difference time domain (FDTD) method. This allows transmission information to be computed but not the band structure of the photonic crystals. FEMLAB (Comsol 2002) is an interactive environment running under MATLAB and used for modelling and simulating scientific and engineering problems based on partial differential equations. FEMLAB has an electromagnetics module that allows simulation of wave propagation and AC-DC electromagnetics in 2 and 3 dimensions. RSoft have recently released BandSolve (BandSOLVE 2002) based on the plane wave method it is designed to automate and simplify the calculation of photonic band structures for photonic crystal (PC) devices. The tool handles a wide range of PC components, including 2D and 3D PC slabs and waveguides, 2D and 3D cavity problems, and photonic crystal fibres. RSOFT also offer BeamPROP (BeamPROP 2002) and FullWAVE (FullWAVE 2002); two packages designed for optical waveguide modelling based on the beam propagation and finite difference time domain method respectively.

The quality of these products is very good and they provide an excellent set of tools for electromagnetic computation. However, none of them are designed primarily and specifically for the analysis of photonic band gap devices. For this reason we have decided to develop a bespoke set of software tools from scratch based on the finite element method. It is also important to note that many of these commercial tools were not available at the time this research commenced. Their subsequent release provides strong evidence that this area of

research is a vibrant one with significant commercial as well as purely academic interest involved with it. Our research group is concurrently developing a suite of highly optimised eigenvalue solvers designed specifically for band-gap modelling to be used in conjunction with the finite element code. This highly specialised approach allows the use of problem specific optimisations to be made. This will allow our software to be tuned to obtain a degree of performance that will allow new avenues to be explored including band-gap design optimisation and the exploration of complex 3 dimensional structures.

1.2 Physics Overview

Investigating the propagation of light in photonic crystals requires the use of Maxwell's equations; these can be stated in their differential, macroscopic form as:

$$\begin{array}{ll} \textit{SI Units} & \textit{Guassian Units} \\ \nabla \cdot \mathbf{B} = 0 & \nabla \cdot \mathbf{B} = 0 \\ \nabla \cdot \mathbf{D} = \rho & \nabla \cdot \mathbf{D} = 4\pi\rho \\ \nabla \times \mathbf{E} = -\dfrac{\partial \mathbf{B}}{\partial t} & \nabla \times \mathbf{E} + \dfrac{1}{c}\dfrac{\partial \mathbf{B}}{\partial t} = 0 \\ \nabla \times \mathbf{H} = \mathbf{J} + \dfrac{\partial \mathbf{D}}{\partial t} & \nabla \times \mathbf{H} - \dfrac{\partial \mathbf{D}}{\partial t} = \dfrac{4\pi}{c}\mathbf{J}, \end{array} \tag{1.1}$$

where **H** and **E** are the magnetic and electric fields, **B** and **D** are the magnetic and electric flux density, **J** is the electric current density and ρ is the electric charge density. These equations can be simplified for the case of electromagnetic propagation in photonic crystals. These crystals are composite materials of different homogeneous dielectric materials. There are no free charges or currents therefore $\mathbf{J} = \rho = 0$.

We assume the materials behave linearly and are isotropic with respect to light propagation hence the electric field and the electric flux density obey the following constitutive relationships, $\mathbf{D} = \varepsilon(\mathbf{r})\mathbf{E}$ where $\varepsilon(\mathbf{r})$ is the relative permittivity. A similar relation exists between the magnetic flux density and the magnetic field, $\mathbf{B} = \mu(\mathbf{r})\mathbf{H}$, but for the majority of dielectric materials, certainly those of interest, the magnetic permeability is very close to unity hence we can use $\mathbf{B} = \mathbf{H}$.

The dielectric materials are assumed to be lossless hence the permittivity is a real number as

opposed to the complex dielectric constants used when absorption is an issue. The frequency dependence of the permittivity $\varepsilon(\mathbf{r})$ is considered to be constant appropriate to the frequency range of the light being modelled. These conditions allow Maxwell's equations to be re-expressed as:

$$\begin{aligned}
&\nabla \cdot \mathbf{H}(\mathbf{r},t) = 0 \\
&\nabla \cdot \varepsilon(\mathbf{r})\mathbf{E}(\mathbf{r},t) = 0 \\
&\nabla \times \mathbf{E}(\mathbf{r},t) + \frac{1}{c}\frac{\partial \mathbf{H}(\mathbf{r},t)}{\partial t} = 0 \\
&\nabla \times \mathbf{H}(\mathbf{r},t) - \frac{\varepsilon(\mathbf{r})}{c}\frac{\partial \mathbf{E}(\mathbf{r},t)}{\partial t} = 0.
\end{aligned} \tag{1.2}$$

The time dependence, t, of the magnetic and electric fields can be separated from the spatial dependence via expansion into a set of harmonically oscillating modes of single frequency. These modes can be expressed as the product of a static field and a complex exponential:

$$\begin{aligned}
\mathbf{H}(\mathbf{r},t) &= \mathbf{H}(\mathbf{r})e^{i\omega t} \\
\mathbf{E}(\mathbf{r},t) &= \mathbf{E}(\mathbf{r})e^{i\omega t},
\end{aligned} \tag{1.3}$$

where ω represents the angular frequency. Suppressing the complex exponential allows the harmonic modes to be written as:

$$\nabla \times \mathbf{E}(\mathbf{r}) + \frac{i\omega}{c}\mathbf{H}(\mathbf{r}) = 0 \tag{1.4}$$

$$\nabla \times \mathbf{H}(\mathbf{r}) - \frac{i\omega}{c}\varepsilon(\mathbf{r})\mathbf{E}(\mathbf{r}) = 0 \tag{1.5}$$

dividing by $\varepsilon(\mathbf{r})$ and then taking the curl gives:

$$\nabla \times \left[\frac{1}{\varepsilon(\mathbf{r})}\nabla \times \mathbf{H}(\mathbf{r})\right] = \frac{i\omega}{c}\nabla \times \mathbf{E}(\mathbf{r}) \tag{1.6}$$

Equation (1.5) can be used to eliminate $\mathbf{E}(\mathbf{r})$ to give an equation entirely in terms of $\mathbf{H}(\mathbf{r})$:

$$\nabla \times \left[\frac{1}{\varepsilon(\mathbf{r})}\nabla \times \mathbf{H}(\mathbf{r})\right] = \left(\frac{\omega}{c}\right)^2 \mathbf{H}(\mathbf{r}) \tag{1.7}$$

Equation (1.7) is an eigenvalue problem. Solving this equation for a given photonic crystal, described by $\varepsilon(\mathbf{r})$ gives the frequencies, ω, and fields $\mathbf{H}(\mathbf{r})$ of the allowable modes of

propagation. The divergence condition, $\nabla \cdot \mathbf{H}(\mathbf{r}) = 0$, must also be enforced. Substituting equation (1.5) back into (1.7) allows one to recover the electric field, $\mathbf{E}(\mathbf{r})$:

$$\mathbf{E}(\mathbf{r}) = \left[\frac{-ic}{\omega\varepsilon(\mathbf{r})}\right]\nabla \times \mathbf{H}(\mathbf{r}). \tag{1.8}$$

1.3 Finite Element Overview

The finite element method is a mature numerical technique for solving boundary value problems. It dates back to the 1940s, originally being used to solve problems in the field of structural mechanics. The first application of finite elements to an electrical engineering problem was made in the late 1960s and since then the technique has been applied to an ever-increasing range of scientific and engineering problems in the domain of computational electromagnetics.

The finite element method involves breaking down the problem domain, in this case the photonic crystal structure, into many small elements of simple shape (e.g. triangles in two dimensions, tetrahedra in three dimensions). Elemental equations are derived from Maxwell's equations that approximate the electromagnetic field over an element. This approximation of the field is expressed as an interpolation function coupled with its coefficients. The choice of interpolation function is a compromise between quality of approximation and the number of function coefficients, also known as the number of degrees of freedom. A high order interpolation function may give a good approximation to the true solution but will require a large number of degrees of freedom thus increasing the computational and storage costs of the simulation. Once the interpolation function is chosen, the function coefficients must be computed for every element, these are stored as elemental matrices. These matrices are subsequently assembled into global matrices by mapping local to global interpolatory node numbers. These global matrices form an eigensystem of sparse matrices. This system of equations is then solved using a subspace iterative technique, the resulting eigenvalues being the frequencies of the allowable modes and the corresponding eigenvectors representing the field strength at the nodes (Fagan 1992) (Zienkiewicz and Taylor 1989). The process can be broken down into steps as illustrated in Figure 1-3.

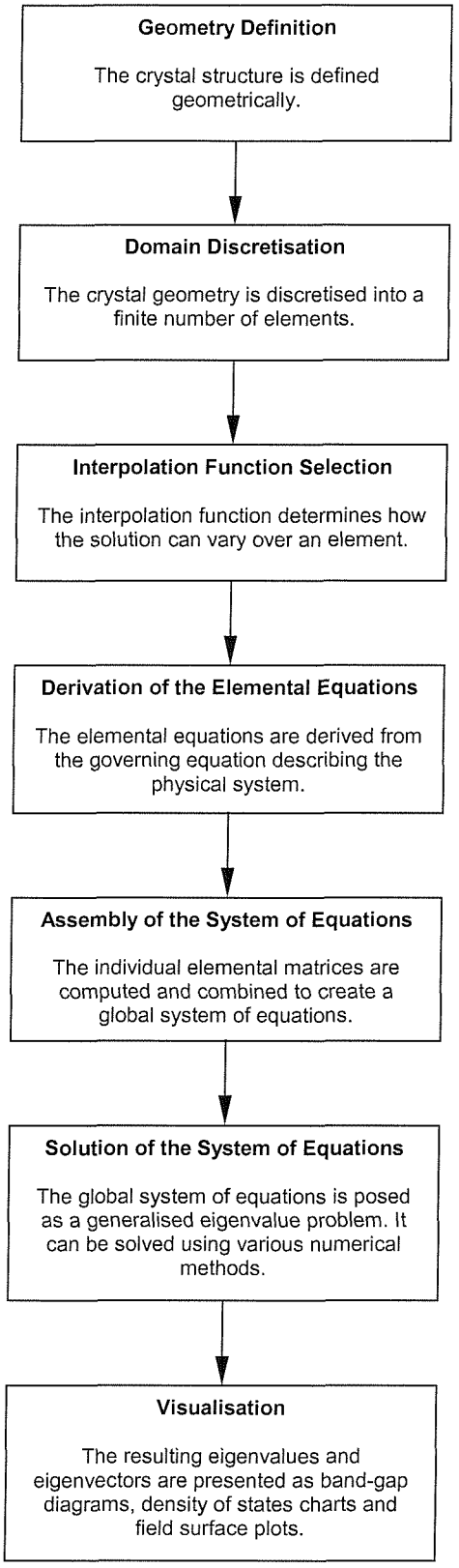

Figure 1-3 Breakdown of the finite element method.

1.4 Contributions

The main contribution of this work has been the creation of a finite element software library specifically designed to model the optical properties of photonic band gap devices. At the time of conception of this project, finite element codes capable of computing the band structure of photonic band gap devices were not available, since then commercial packages have emerged but none are, as yet, optimised specifically for photonic band gap device modelling. In this respect we have produced a novel and genuinely useful product. This thesis presents a detailed description of the finite element method and its application to photonic band gap device modelling; this is essentially the problem of solving Maxwell's equations subject to periodic boundary conditions.

The software has been tested extensively, including comparison with analytical results, results produced from other numerical methods including plane wave expansion and finite difference time domain and experimental results. Algorithm performance has been investigated, specifically the relationship between solution accuracy, mesh granularity, interpolation order, computation time and memory requirements.

The finite element software has been used to model novel crystal geometries including the twelve-fold symmetric quasicrystal. This structure possesses a high degree of rotational symmetry and has been proposed to exhibit a photonic band gap for low filling fractions and low dielectric contrast between the constituent materials. The validity of these claims is explored.

The development of the finite element code has allowed other new contributions to be made including the investigation into the effect of fabrication tolerances on the band structure of photonic band gap devices. Also, design optimisation of photonic band gap structures with respect to maximising the resultant photonic band gap. This involved a brute force approach in which the best of a large selection of randomly generated crystal lattices were subsequently optimised. The other approach involved the investigation of a canonical set of lattices such that all possible rod-based lattice structures were broken down into a set of groups, with the most promising groups then being optimised.

A number of papers have presented theoretical photonic crystal geometries and subsequently computed their band structures. It is often the case that these structures bear little resemblance to

what is actually possible to fabricate. For example, it is well known that crystal structures with a high filling fraction are likely to produce large band gaps, however, this can result in very thin areas of substrate material which would be vulnerable to collapsing when fabricated thus destroying the crystal structure. We investigated the effect of fabrication tolerances on the resulting band structure of PBG devices, this has not been presented before in the literature and we feel that it has an important bearing upon how one interprets the results from the various numerical models with regard to actually fabricating these devices.

The finite element code has been incorporated into a design optimisation process that attempts to find the crystal geometry that maximises the size of the photonic band gap. This involved implementing a minimisation algorithm to explore the crystal structure parameter space in an attempt to find the optimum crystal structure. The optimisation code was run on a Windows based commodity cluster of workstations. The computationally intensive nature of the optimisation process would have been unfeasible without the utilisation of this grid-enabled computational resource.

The work in this thesis has contributed in part or full to the following publications:

- Hiett, BP, Generowicz, J.M, Cox, S.J, Molinari, M, Beckett, D.H, and Thomas, K.S. (2002). *Application of Finite Element Methods to Photonic Crystal Modelling.* IEE. Proc.-Sci. Meas. Technol., Vol. 149, No. 5, p293-296, September 2002

- Hiett, BP, Generowicz, JM, Beckett, DH, Molinari, M, Cox, SJ, Thomas, KS (2002) *Photonic Band Gaps in 12-Fold Symmetric Quasicrystals*. 4th International Conference on Materials for Microelectronics and Nanoengineering. Espoo, (Finland, June 2002).

- Thomas, KS, Cox SJ, Beckett, DH, Hiett, BP, Generowicz, JM, Daniell, GJ, (2001) *Eigenvalue Spectrum Estimation and Photonic Crystals*. Lecture Notes in Computer Science. Proceedings of Euro-Par 2001 Conference, p.578-586 (Manchester 28-31 Aug 2001).

- Hiett, BP, Generowicz, JM, Cox, SJ, Molinari, M, Beckett, DH, Parker, GJ, and Thomas, KS (2001) *Finite Element modelling of Photonic Crystals*. Proc. PREP 2001 EPSRC Conference p.87-88. (Keele University, April 9-11 2001)

- Generowicz, JM, Hiett, BP, Beckett, DH, Molinari, M, Charlton, MDB, Parker, GJ, Cox SJ. (2000). *Modelling Photonic Crystals using Finite Elements*. NATO Advanced Study Institute. Photonic Crystals and Light Localization, (Crete. June 19-30, 2000).

- Generowicz, JM, Hiett, BP, Beckett, DH, Parker, GJ, Cox SJ. (2000). *Modelling 3 Dimensional Photonic Crystals using Vector Finite Elements*. Photonics 2000 (EPSRC, UMIST, Manchester, 4-5 July 2000).

1.5 Outline of Thesis

Chapter 1 – *Introduction*. This chapter introduces the concept and principles behind photonic band gap devices along with a number of potential applications. The finite element method is introduced along with a short recap on the history of its development. The basic steps involved in the procedure are outlined along with some of the technical issues specific to using the finite element method to solve electromagnetic problems.

Chapter 2 - *The Finite Element Method.* The various stages of the finite element method are examined in detail. These include domain decomposition; the process of dividing the crystal structure into a number of smaller sections of simple geometry. The elemental equations are derived based upon the governing differential equation, the periodic boundary conditions and the chosen interpolation functions. These elemental equations can then be applied to each element. The resulting elemental matrices are assembled according to the mesh topology to give the global matrices that comprise a generalised eigenvalue problem. The eigenvalue solver we developed is discussed, with the focus on the problem specific optimisations that we implemented to increase the performance.

Chapter 3 – *Results*. In this chapter we test the accuracy of our two-dimensional finite element code by comparison with an analytical solution for free-space. A number of commonly modelled structures are modelled and subsequently compared with results found in the literature produced with other numerical methods including plane wave expansion and finite difference methods. Finally, we compare our results with actual experimental data to confirm that a two-dimensional model can accurately model a real device.

Chapter 4 – *Performance*. The accuracy and convergence of the finite element code is analysed. Also the relationship between solution accuracy, computation time and memory usage is

examined with respect to mesh granularity and interpolation order. We discuss the programming paradigms and design decisions that were taken during code development. Also the use of high performance, grid-enabled computing facilities is discussed. This was necessary due to the computationally intensive nature of the research, particularly the creation of gap-map data and design optimisation.

Chapter 5 – *The 12-Fold Symmetric Quasicrystal.* The 12-fold symmetric quasicrystal has been proposed as a novel new crystal structure that exhibits a complete band gaps at low filling fractions and low dielectric contrasts. Also, its high degree of rotational symmetry should make it highly inhomogeneous to the angle of incoming light. We investigate these claims by modelling a number of these structures for various crystal configurations, filling fractions substrate materials, etc. and present the results and draw our conclusions.

Chapter 6 – *Optimisation.* We created a photonic crystal design optimisation code, the aim being to automate the process of designing a photonic crystal with a large band gap. This required building a front-end code capable of converting a high-level crystal structure definition into a low level description in a format understandable by the meshing software. We also had to build code to analyse the resulting set of eigenvalues to ascertain the presence and size of any band gaps. We finally implemented a minimisation algorithm to perform the optimisation. This iteratively sought the design parameter set that produced the largest band gap.

Chapter 7 - *Conclusions and Future Work.* We summarise and conclude the work that has been carried out and also explore areas of possible further research.

2 The Finite Element Method

2.1 Domain Discretisation

Many domain discretisation software packages are available, for example, GEOMPACK (Joe 2001), Easymesh (Niceneco 2000), NETGEN (Schöberl 2001) and Triangle (Shewchuk 1996). Each package has its own proprietary format for the input of the domain geometry and other parameters including the type of element (triangle, rectangle, etc.), the number of elements (granularity of discretisation), the dimensionality (2D, 3D), element material properties (dielectric constant) and domain boundary conditions. The software processes this input data and computes the domain discretisation and outputs the vertex coordinates, topology and material properties of the constituent elements. Examples of two-dimensional and three-dimensional domain discretisations (or meshes) are shown below in Figure 2-1.

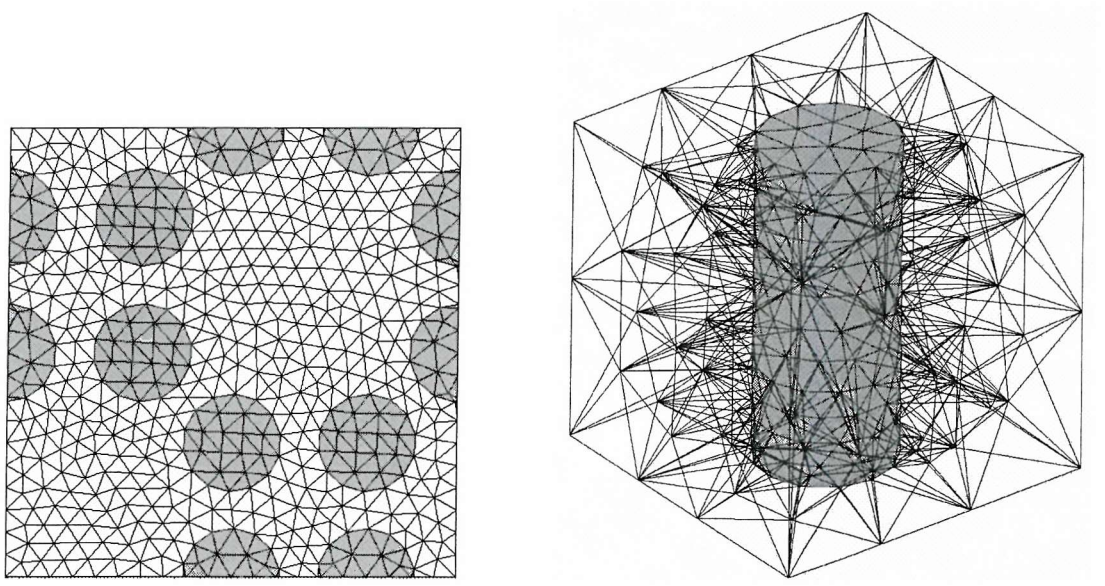

(a) (b)

Figure 2-1 Periodic domain discretisation examples in two dimensions (a) and three dimensions (b).

The meshing software is used to generate a unit cell of finite elements. This represents the 'building block' of the PC structure: a PC of infinite extent can be recreated by periodically tiling the unit cell as shown in Figure 2-2. The implementation of the periodic boundary conditions is covered in detail in chapter 4.4.

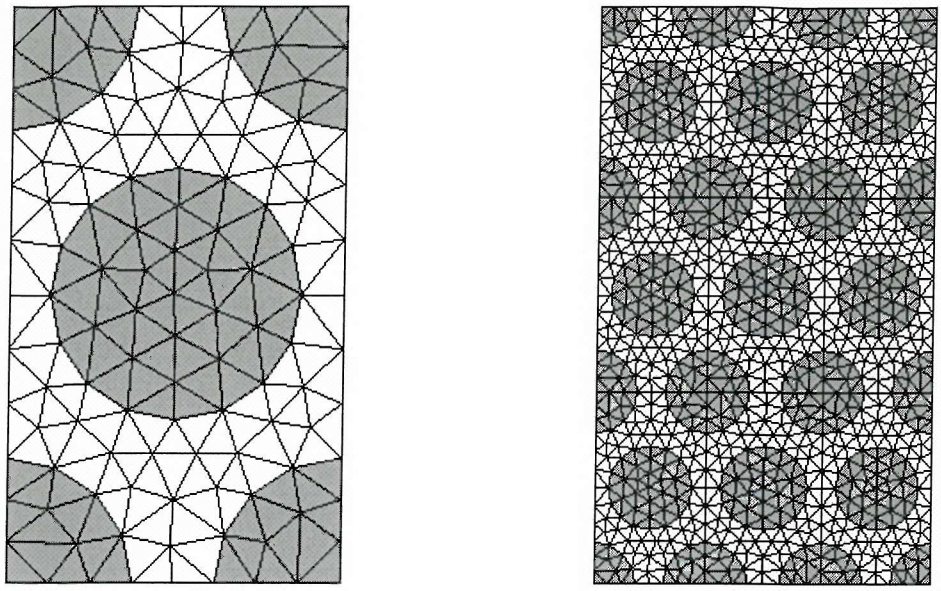

(a) (b)

Figure 2-2 Unit cell (a); Periodic tiling (b), showing 9 unit-cells tiled together.

Each element also stores a material marker, as can be seen by the grey and white triangles in Figure 2-2. This mesh is a two-dimensional representation of a triangular lattice of circular rods in a substrate material. The material markers are substituted with the relevant material permittivity values when the mesh is read into the finite element software.

2.2 Interpolation Functions

Interpolation functions are used to approximate a continuous solution over an element. These functions are most easily developed in terms of simplex coordinates (see Appendix B.1). These coordinates are local to an element and remain unchanged under any translation or rotation in Cartesian space; therefore, general element equations need only be generated once for a prototypal simplex.

The interpolation functions can be constructed using a family of auxiliary polynomial $R_m(n,\xi)$ where n is the degree of the polynomial. The m^{th} member of R is defined as follows:

$$R_m(n,\xi) = \prod_{k=0}^{m-1} \frac{\xi - k/n}{m/n - k/n} = \frac{1}{m!}\prod_{k=0}^{m-1}(n\xi - k), \qquad m > 0$$
$$R_0(n,\xi) = 1 \tag{2.1}$$

For a simplex element of dimensionality, D, the number of interpolatory nodes, M, for a Lagrange interpolation polynomial of order n is defined as follows:

$$M = \frac{1}{D!}\prod_{i=1}^{D}(n+i). \tag{2.2}$$

Figure 2-3 shows a triangular element with interpolatory nodes corresponding to a cubic (third order) interpolation polynomial describing the unknown field quantity across its area. The triangle vertices are labelled 1, 2 and 3. Each node is labelled with its natural and singular index node number. The natural node number corresponds to the i, j, k in equation (2.3). The singular index node number corresponds to the m in equation (2.5).

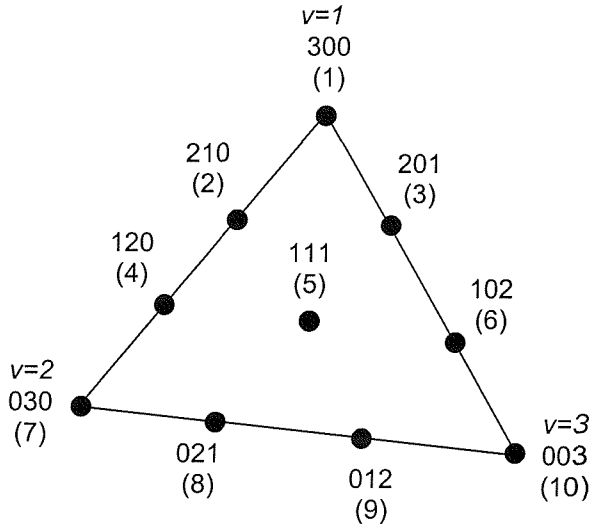

Figure 2-3 Triangular element with cubic interpolation.

The interpolation function for each interpolatory node in two-dimensions is calculated using equation (2.3).

$$\alpha_{ijk} = R_i(n,\xi_1)R_j(n,\xi_2)R_k(n,\xi_3), \qquad i+j+k=n \text{ . (2D)} \tag{2.3}$$

In three dimensions, using tetrahedral elements, an extra natural node index is needed to deal with the additional simplex coordinate.

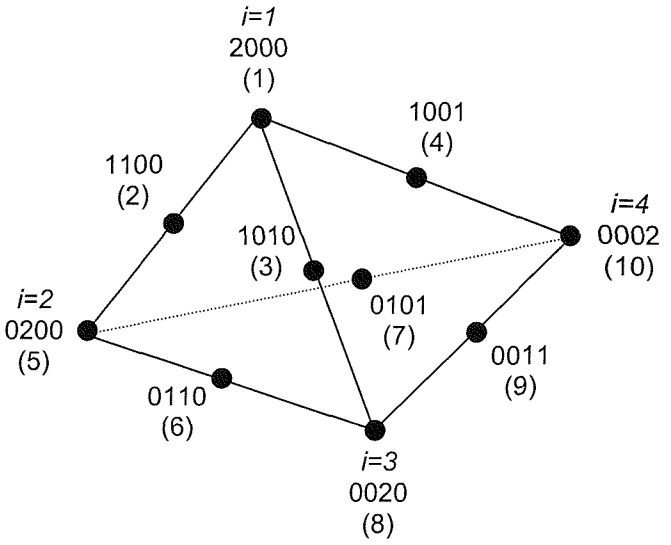

Figure 2-4 Tetrahedral element with quadratic interpolation.

Hence, the formulation of the interpolation functions requires an extra term:

$$\alpha_{ijkl} = R_i(n,\xi_1)R_j(n,\xi_2)R_k(n,\xi_3)R_l(n,\xi_4), \qquad i+j+k+l=n \text{ . (3D)} \tag{2.4}$$

The solution over an element is expressed as a combination of the interpolation function (also commonly called the basis function) and the value of the unknown quantity at the interpolatory nodes:

$$\Psi = \sum_{m=1}^{M} \psi_m \alpha_m \text{ ,} \tag{2.5}$$

where Ψ is the approximate solution over an element, M is the number of interpolatory nodes for an element (calculated using (2.2)), ψ_m is the value of the solution ψ at the node m, and α_m is the basis function associated with the node m.

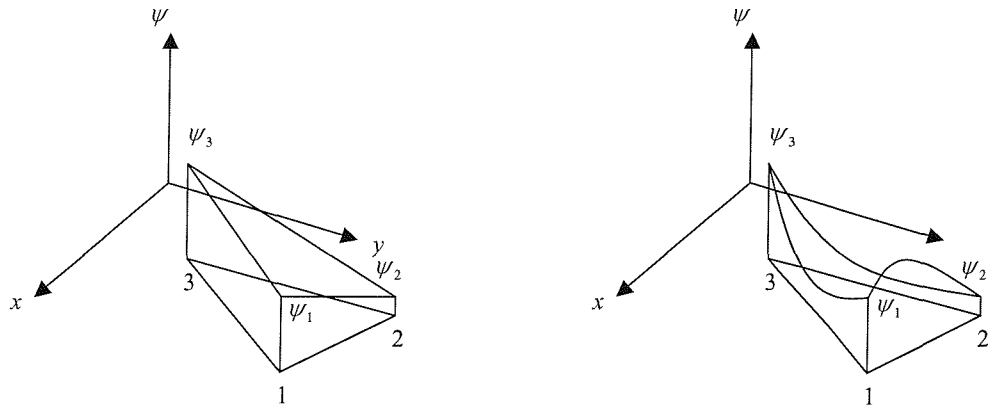

Figure 2-5 Linear and quadratic interpolation functions.

Figure 2-5 illustrates the difference between using a linear polynomial and a quadratic polynomial. There is a computational trade off between the order of the interpolation polynomial that is used and the accuracy of the solution, a quantitative analysis of this relationship is presented in chapter 3.7.

2.3 Governing Mathematical Equations

The fundamental problem to be solved is as follows. Given the physical structure and material properties of a photonic crystal, what are the resulting allowable mode frequencies? If we define the photonic crystal by the function $\varepsilon(\mathbf{r})$ and the allowable mode frequencies are represented by ω, the problem can be stated simply as:

$$\varepsilon(\mathbf{r}) \Rightarrow \omega$$

We need to provide the means to get from $\varepsilon(\mathbf{r})$ to ω. The governing equations that bind these properties can be derived from Maxwell's equations (Halliday, Resnick et al. 1992) to give the formulae for modelling monochromatic electromagnetic waves in a periodic dielectric waveguide, equation (2.6):

$$\begin{cases} \nabla \times \left[\dfrac{1}{\varepsilon(\mathbf{r})} \nabla \times \mathbf{H}(\mathbf{r}) \right] = \left(\dfrac{\omega}{c} \right)^2 \mathbf{H}(\mathbf{r}) \\ \nabla \cdot \mathbf{H}(\mathbf{r}) = 0 \end{cases} \tag{2.6}$$

H represents the magnetic field intensity, $\varepsilon(\mathbf{r})$ represents the dielectric constant (or the electric permittivity) as a function of the spatial position, **r**. ω is the frequency of the electromagnetic

wave and c is the speed of light.

A feature of equation (2.6) is that there is a simple relationship between the scale of the crystal structure and the frequency of the harmonic modes. Contraction or expansion of a structure, $\varepsilon(\mathbf{r})$, by a factor, s, to give the structure $\varepsilon'(\mathbf{r}) = \varepsilon(\mathbf{r}/s)$ leads to inverse scaling of the resultant harmonic mode frequencies, e.g. $\omega' = \omega s$. Thus the equation solution at one scale effectively determines the solutions for all scales. This fact has implications for data visualisation and in the measurement of photonic band gap frequency ranges that are discussed later in chapter 2.12.

2.4 Two-Dimensional Scalar Case

If the waveguide structure is periodic in two dimensions and constant with respect to the third dimension (e.g. Figure 1-1) and only waves propagating in the plane of periodicity are to be considered then the vector equation can be split into two scalar equations (Axmann and Kuchment 1999) (Dobson 1999) representing the transverse magnetic (TM) and transverse electric (TE) modes:

$$\text{TE Mode Polarisation:} \quad -\nabla \cdot \frac{1}{\varepsilon(\mathbf{r})} \nabla \psi = \lambda \psi , \tag{2.7}$$

$$\text{TM Mode Polarisation:} \quad -\nabla^2 \psi = \varepsilon(\mathbf{r}) \lambda \psi . \tag{2.8}$$

The fact that (2.7) and (2.8) are periodic problems (e.g. $\varepsilon(\mathbf{r})$ varies periodically) allows the application of the Floquet-Bloch theory (Kuchment 1993). This states that the eigenfunctions of the wave function for a periodic potential are the product of a plane wave $e^{i\mathbf{k}\cdot\mathbf{r}}$ times a function $u_{\mathbf{k}}(\mathbf{r})$ with the periodicity of the crystal lattice. Thus, the wave function can be represented as

$$\psi = e^{i\mathbf{k}\mathbf{r}} u(\mathbf{r}) , \tag{2.9}$$

where $\mathbf{k}$ is the wave vector and $u(\mathbf{r})$ is the value of the eigenfunction at position $\mathbf{r}$. Substituting equation (2.9) into equation (2.7) gives:

$$-(\nabla + i\mathbf{k}) \cdot \frac{1}{\varepsilon(\mathbf{r})} (\nabla + i\mathbf{k}) u = \lambda u . \tag{2.10}$$

It remains to find a solution to the above differential equation given the periodic boundary conditions. This can be done using a weighted residual (Galerkin's) method [see Appendix A:] to approximate the true solution of the boundary-value problem. This gives the following integral equation:

$$\int \frac{1}{\varepsilon(\mathbf{r})}(\nabla + i\mathbf{k})u \cdot \overline{(\nabla + i\mathbf{k})v}\, dx = \lambda \int u\bar{v}dx. \tag{2.11}$$

Representing $u = \sum \psi_j \alpha_j$ where ψ_j is the unknown field amplitude at the j^{th} node and α_j is the j^{th} basis function and choosing the weighting function v to be equal to the basis function α_l gives the generalised eigenvalue problem:

$$\mathbf{A}(\mathbf{k})\psi = \lambda \mathbf{B}\psi\,, \tag{2.12}$$

where the assembled matrices are formed from the elemental piecewise functions:

$$\begin{aligned} A_{jl} &= \int \frac{1}{\varepsilon(\mathbf{r})}(\nabla + i\mathbf{k})\alpha_j \cdot \overline{(\nabla + i\mathbf{k})\alpha_l} dx \\ B_{jl} &= \int \alpha_j \alpha_l dx \end{aligned} \tag{2.13}$$

Expanding the integral that comprises the **A** matrix gives:

$$\begin{aligned} &(\nabla + i\mathbf{k})\alpha_j \cdot (\nabla + i\mathbf{k})\alpha_l \\ &= (\nabla\alpha_j + i\mathbf{k}\alpha_j) \cdot (\nabla\alpha_l + i\mathbf{k}\alpha_l) \\ &= \nabla\alpha_j \cdot \nabla\alpha_l + \nabla\alpha_j \cdot i\mathbf{k}\alpha_l + i\mathbf{k}\alpha_j \cdot \nabla\alpha_l + i\mathbf{k}\alpha_j \cdot i\mathbf{k}\alpha_l \\ &= \nabla\alpha_j \cdot \nabla\alpha_l && \rightarrow\ S_{jl} \\ &+ i\mathbf{k}(\nabla\alpha_j \cdot \alpha_l + \alpha_j \cdot \nabla\alpha_l) && \rightarrow\ i\mathbf{k}(P_{jl} + P_{lj}) \\ &- k^2\alpha_j\alpha_l && \rightarrow\ k^2 T_{jl} \end{aligned} \tag{2.14}$$

Hence, from the following integral equations base solely on the interpolation functions we can construct the eigensystem matrices:

$$
\begin{aligned}
S_{jl} &= \int_{\Omega} \nabla\alpha_j \cdot \nabla\alpha_l d\Omega \\
T_{jl} &= \int_{\Omega} \alpha_j \alpha_l d\Omega \\
P_{jl} &= \int_{\Omega} \alpha_j \nabla\alpha_l d\Omega
\end{aligned}
\tag{2.15}
$$

For the TE Mode polarisation:

$$
\begin{aligned}
\mathbf{A}(\mathbf{k}) &= \frac{1}{\varepsilon(\mathbf{r})}\left[\mathbf{S} + i\mathbf{k}\cdot\mathbf{P} - k^2\mathbf{T}\right] \\
\mathbf{B} &= \mathbf{T}
\end{aligned}
\tag{2.16}
$$

For the TM polarisation the **A** and **B** matrices are defined as:

$$
\begin{aligned}
A_{jl} &= \int (\nabla + i\mathbf{k})\alpha_j \cdot \overline{(\nabla + i\mathbf{k})\alpha_l}\, dx\,, \\
B_{jl} &= \int \varepsilon(\mathbf{r})\alpha_j \alpha_l dx\,.
\end{aligned}
\tag{2.17}
$$

Hence, the eigensystem matrices can be expressed in terms of the interpolation function integrals as follows:

$$
\begin{aligned}
\mathbf{A}(\mathbf{k}) &= \mathbf{S} + i\mathbf{k}\cdot\mathbf{P} - k^2\mathbf{T} \\
\mathbf{B} &= \varepsilon(\mathbf{r})\mathbf{T}
\end{aligned}
\tag{2.18}
$$

The full derivation for the integral equations in equation (2.15) can be found in Appendix C:. The **T** (metric) matrix is independent of element size and shape and therefore can be stored in tabulated form and used for all elements. The **S** (Dirichlet) matrix and the **P** matrix can be calculated in terms of **D** (Appendix B.4) and **T** matrices and the element geometry.

2.5 Three-Dimensional Vector Case

A logical progression is to extend the two dimensional model to treat the full three-dimensional case. This removes the constraint that the dielectric structure must be constant in the third dimension, thus providing the freedom to explore the properties of fully three-dimensional periodic crystals (Bossavit and Verite 1982; Yablonovitch, Gmitter et al. 1992; Campbell, Sharp et al. 2000). The additional dimension necessitates the computation of a vector rather than scalar

approximation to the electromagnetic field therefore the FEM must be modified accordingly and, as will be explained later in this chapter, a radically new type of finite element is needed.

A naïve approach would be to continue using Lagrange (scalar) interpolation functions, one for each component of the vector field, e.g. three functions for each node, one for each dimension. There is however, an immediately apparent problem with this approach. This is because the Lagrange interpolation functions ensure continuity at material interfaces; each component of the vector field will therefore be continuous. This does not satisfy Maxwell's equations that enforce tangential but not normal continuity of the electric and magnetic field at material interfaces.

There is also a more subtle problem with the application of Lagrange elements in the computation of vector fields; the phenomena of spurious modes (Jin 1993; Silvester and Ferrari 1996; Salazar-Palma, Sarkar et al. 1998). These are numerical approximations to non-physical solutions, e.g. solutions that do not satisfy Maxwell's equations and the imposed boundary conditions. The result is that the computed spectrum of correct allowable electromagnetic modes is contaminated with these incorrect solutions.

These spurious solutions originate from the fact that using the finite element method with Lagrangian interpolation functions does not enforce the divergence condition as defined in Maxwell's equations:

$$\nabla \cdot (\mu \mathbf{H}) = 0, \tag{2.19}$$

$$\nabla \cdot (\varepsilon \mathbf{E}) = 0, \tag{2.20}$$

for the magnetic and the electric fields (in a source free region) respectively. The spurious solutions are found to have substantial non-zero divergences. This flaw appears because only the interpolation functions and not their derivatives are required to be continuous.

Attempts have been made to eliminate the problem of spurious modes when using Lagrange elements. Interpolation functions with continuous derivatives (Csendes and Wong 1987; Wong and Csendes 1988; Sun, Manges et al. 1995) have been applied to enforce the zero divergence condition. The disadvantage is that these functions are more complex and therefore harder to implement. Another approach is to introduce a penalty term to the functional (Rahman, Fernandez et al. 1991). This has the effect of pushing eigenvalues relating to the spurious

solutions up into a higher frequency region out of the range of the propagation modes of interest.

2.6 Curl-Conforming Elements

A more fundamental approach is to use curl-conforming elements where the interpolation functions are of a vector rather than scalar nature. This approach uses vector based interpolation functions such that the tangential component of the field is zero at all element boundaries except one. At this boundary, the tangential component is defined solely by the shape and orientation of that boundary. This approach ensures the desired continuity of tangential component of the field but allows the normal component to be discontinuous. It is from this property that the name, 'curl-conforming' is derived in that the continuous tangential component is the required condition for defining the curl of the vector variable (Nedelec 1986). The non-continuous normal component means that the divergence operation may not be defined for the vector variable hence the elements are not 'div-conforming'. Spurious solutions still occur with the use of curl-conforming elements but they are associated only with zero eigenvalues as opposed to the correct physical solutions that have strictly positive eigenvalues. In this way, spurious modes can be easily distinguished and disregarded. Figure 2-6 illustrates a curl-conforming vector basis function for a two-dimensional triangular element (for ease of visualisation over a three-dimensional element). The key features of interest are the constant tangential field component on the edge between vertices one and two and the zero tangential components on the remaining two edges.

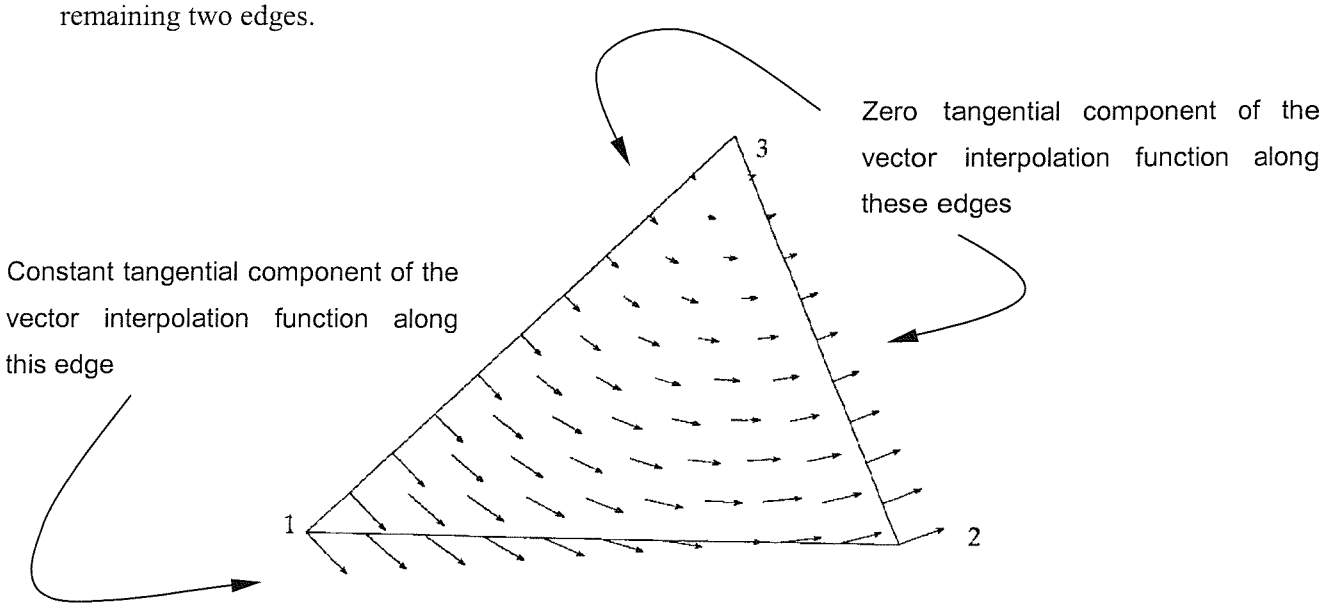

Figure 2-6 A curl-conforming vector interpolation function.

Equation (2.5) now becomes equation (2.21) for the vector FEM. $\mathbf{\Psi}(\mathbf{r})$ represents the approximation of the **E** or **H** field vector (electric or magnetic respectively) at spatial position **r**. ψ_m is the unknown nodal coefficient of the vector interpolation function $\boldsymbol{\tau}_m$. In order to use this approximation for the field vector the vector interpolation functions, $\boldsymbol{\tau}$, must be developed such that they exhibit the tangential and normal continuity requirements between elements as discussed previously (Webb 1993; Webb and Forghani 1993).

$$\mathbf{\Psi}(\mathbf{r}) = \sum_{m=1}^{M} \psi_m \boldsymbol{\tau}_m(\mathbf{r}) \tag{2.21}$$

The development of these vector interpolation functions is most easily demonstrated using first order elements. These are also known as edge elements because there is a one to one mapping between interpolation functions and edges. The procedure can be broken down into the following steps:

1. Define a standard tetrahedral element mapping edges to vertices.
2. Develop three-dimensional simplex coordinates.
3. Use the simplex coordinates and gradients of the simplex coordinates to formulate vector functions that satisfy the continuity requirements.
4. Derive the elemental matrix equations via integration of the vector basis functions.
5. Compute the three-dimensional elemental matrices.
6. Assemble and then solve the resulting system of equations.

In order to use edge elements it is necessary to define a standard mapping between edges and vertices as detailed in Table 2-1.

Edge I	Vertex i_1	Vertex i_2
1	1	2
2	1	3
3	1	4
4	2	3
5	4	2
6	3	4

Table 2-1 Edge to vertex mapping for a tetrahedral element.

This information can be visualised as in Figure 2-7 with the arrows representing the directions of the edges running from vertex i_1 to i_2.

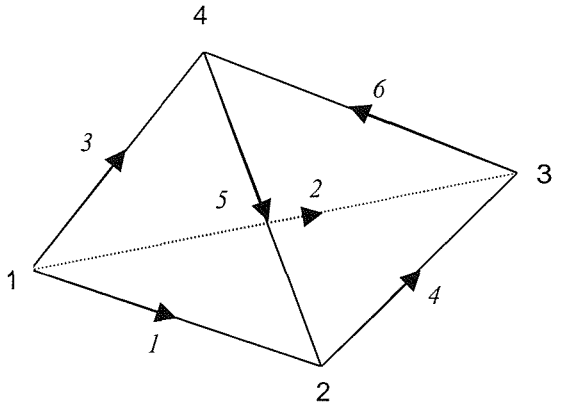

Figure 2-7 Edge and vertex definition for a tetrahedral element.

The three-dimensional simplex coordinates are derived as explained in appendix B.3. The gradients, $\nabla\xi_i$, of the simplex coordinates are vector functions with several properties that make them suitable for the construction of vector basis functions:

$$\nabla\xi_i \cdot \mathbf{e}_{jk} = \begin{cases} 0 & i \neq j \text{ and } i \neq k \\ \pm 1 & i = j \text{ or } i = k \end{cases}. \tag{2.22}$$

1. $\nabla\xi_i$ is a constant vector, the magnitude of which is defined by the coordinates of the tetrahedral vertices.
2. $\nabla\xi_i$ is perpendicular to the face opposite vertex i.
3. The tangential component of $\nabla\xi_i$ along an edge with i as a vertex is dependent only upon the geometry of that edge, e.g. the two vertex coordinates.
4. The tangential component of $\nabla\xi_i$ across a face with vertex i is dependent only upon the geometry of that face, e.g. the three vertex coordinates.

Any scalar function of ξs multiplied by the vector $\nabla\xi$ will possess the same tangential continuity characteristics hence it remains to specify a combination of ξ and $\nabla\xi$ that are suitable for use as a vector interpolation function. The necessity is that the interpolation functions be linearly independent of one another. First order vector interpolation functions $\boldsymbol{\tau}_1$ to $\boldsymbol{\tau}_6$ with the required linear independence have been proposed by (Nedelec 1986) and (Bossavit and Verite 1982) and have therefore been named Nedelec-Bossavit edge elements. These curl-conforming vector interpolation functions can be expressed as:

$$\mathbf{N}_i = l_i(\xi_{i_1}\nabla\xi_{i_2} - \xi_{i_2}\nabla\xi_{i_1}), \tag{2.23}$$

where i, is the edge number and i_1 and i_2 are the vertices at either end of that edge (see Table 2-1). $\mathbf{N}_i$ is the i^{th} vector basis function, l_i is the length of edge i and ξ_{i_x} is the simplex coordinate corresponding to vertex i_x.

2.7 Maxwell Vector Wave Equation

In treating the fully 3D photonic crystal simulation the governing Maxwell equations can no longer be broken down into two scalar equations for each polarisation. Instead the full vector equation must be given the Floquet-Bloch treatment and subsequently discretised into a form suitable for finite elements. The first step is to substitute Bloch's theorem into the governing equation:

$$\nabla\times\left[\frac{1}{\varepsilon(\mathbf{r})}\nabla\times H(\mathbf{r})\right] = \left(\frac{\omega}{c}\right)^2 H(\mathbf{r}) \tag{2.24}$$

Bloch's theorem is used to describe an electromagnetic mode propagating through a periodic dielectric, it states that the allowable modes can be expressed as a plane wave modulated by a function, $\mathbf{u_k}(\mathbf{r})$, which has the same periodicity as the crystal lattice. So the modes can be described the wave vector, $\mathbf{k}$, and the periodic function $\mathbf{u_k}(\mathbf{r})$, $\mathbf{r}$ represents a spatial position:

$$\mathbf{H}_\mathbf{k}(\mathbf{r}) = e^{i(\mathbf{k}\cdot\mathbf{r})}\mathbf{u}_\mathbf{k}(\mathbf{r}) \tag{2.25}$$

Combining equations (2.24) and (2.25) gives the following eigenvalue equation:

$$\nabla\times\left[\frac{1}{\varepsilon(\mathbf{r})}\nabla\times e^{i(\mathbf{k}\cdot\mathbf{r})}\mathbf{u}_\mathbf{k}(\mathbf{r})\right] = \left(\frac{\omega(\mathbf{k})}{c}\right)^2\left(e^{i(\mathbf{k}\cdot\mathbf{r})}\mathbf{u}_\mathbf{k}(\mathbf{r})\right). \tag{2.26}$$

This can be rearranged to give the vector wave equation for a periodic dielectric as:

$$(i\mathbf{k}+\nabla)\times\left[\frac{1}{\varepsilon(\mathbf{r})}(i\mathbf{k}+\nabla)\times\mathbf{u}_\mathbf{k}(\mathbf{r})\right] = \left(\frac{\omega(\mathbf{k})}{c}\right)^2\mathbf{u}_\mathbf{k}(\mathbf{r}). \tag{2.27}$$

2.8 Approximation of the Differential Equation

The differential equation is approximated using a weighted residual method. This yields an approximation to the true solution via minimisation of an integral over the domain. The differential operator on $u(\mathbf{r})$ is defined as follows:

$$\Im = (i\mathbf{k}+\nabla)\times\left[\frac{1}{\varepsilon(\mathbf{r})}(i\mathbf{k}+\nabla)\times \quad\right] \qquad \text{and } \lambda = \left(\frac{\omega}{c}\right)^2 \tag{2.28}$$

An approximation of the solution will therefore produce a residual, e.g.

$$r = \Im u(\mathbf{r}) - \lambda u(\mathbf{r}) \neq 0 \tag{2.29}$$

The best approximation of $u(\mathbf{r})$ is that which reduces the residual, r, to the least value at all points over the domain Ω. The weighted residual method enforces the condition:

$$R_i = \int_\Omega w_i r \, d\Omega = 0 \tag{2.30}$$

In this case the weighting function, w_i, is chosen to be the same as the vector interpolation function, $\mathbf{N}_i$. Hence the residual and subsequently, the integral of the weighted residual, are defined as follows; note the wave vector has been omitted at this stage for clarity:

$$R = \nabla\times\left(\frac{1}{\varepsilon(\mathbf{r})}\nabla\times u(\mathbf{r})\right) - \lambda\, u(\mathbf{r}) \neq 0 \tag{2.31}$$

$$\begin{aligned}&\int_\Omega \mathbf{N}_i\left[\nabla\times\left(\frac{1}{\varepsilon(\mathbf{r})}\nabla\times u(\mathbf{r})\right) - \lambda\, u(\mathbf{r})\right] d\Omega = 0 \\ &= \int_\Omega\left[\mathbf{N}_j\cdot\left(\nabla\times\left(\frac{1}{\varepsilon(\mathbf{r})}\nabla\times u(\mathbf{r})\right)\right) - \mathbf{N}_j\cdot\lambda u(\mathbf{r})\right] d\Omega = 0\end{aligned} \tag{2.32}$$

Using the vector identity:

$$\mathbf{C}\cdot\left(\mathbf{D}\times\left(\mathbf{A}\times\mathbf{B}\right)\right)\equiv\left(\mathbf{A}\times\mathbf{B}\right)\cdot\left(\mathbf{C}\times\mathbf{D}\right), \tag{2.33}$$

One can rearrange (2.32) to give:

$$\begin{aligned}&\int_{\Omega}\left[-\left(\frac{1}{\varepsilon(\mathbf{r})}\nabla\times u(\mathbf{r})\right)\cdot\left(\nabla\times\mathbf{N}_j\right)-\mathbf{N}_j\cdot\lambda u(\mathbf{r})\right]d\Omega=0\\&=\sum_{i=1}^{I}\int_{\Omega}u_i\left[-\left(\frac{1}{\varepsilon(\mathbf{r})}\nabla\times\mathbf{N}_i\right)\cdot\left(\nabla\times\mathbf{N}_j\right)\right]-\mathbf{N}_j\lambda\ \mathbf{N}_i u_i\,d\Omega=0.\end{aligned} \tag{2.34}$$

Substituting the wave vector terms back in at this stage leaves the integral equation that must be solved using finite elements:

$$\int_{\Omega}u_i\left[-\left(\frac{1}{\varepsilon(\mathbf{r})}[\nabla+i\mathbf{k}]\times\mathbf{N}_i\right)\cdot\left([\nabla+i\mathbf{k}]\times\mathbf{N}_j\right)\right]d\Omega-\int_{\Omega}\mathbf{N}_j\lambda\ \mathbf{N}_i u_i d\Omega=0. \tag{2.35}$$

Equation (2.35) is rearranged into the form of a generalised eigenvalue problem. The material permittivity term, $1/\varepsilon(\mathbf{r})$, and frequency term, λ, are constant factors and can therefore commute outside their respective integrals:

$$\frac{1}{\varepsilon(\mathbf{r})}\int_{\Omega}u_i\left[-\left([\nabla+i\mathbf{k}]\times\mathbf{N}_i\right)\cdot\left([\nabla+i\mathbf{k}]\times\mathbf{N}_j\right)\right]d\Omega=\lambda\int_{\Omega}u_i\left[\mathbf{N}_j\cdot\mathbf{N}_i\right]d\Omega. \tag{2.36}$$

The right hand side of equation (2.36) is clearly a simple product of the metric or **T** matrix, the 3D derivation of which is detailed in Appendix F.2. The left hand side must be simplified into component matrices. This is performed via the following steps:

$$
\begin{aligned}
& \left[-(\nabla + i\mathbf{k}) \times \mathbf{N}_i\right] \cdot \left[(\nabla + i\mathbf{k}) \times \mathbf{N}_j\right] \\
= \; & \left[\nabla \times \mathbf{N}_i + i\mathbf{k} \times \mathbf{N}_i\right] \cdot \left[\nabla \times \mathbf{N}_j - i\mathbf{k} \times \mathbf{N}_j\right] \\
= \; & \begin{array}{l} (\nabla \times \mathbf{N}_i) \cdot (\nabla \times \mathbf{N}_j) + (i\mathbf{k} \times \mathbf{N}_i) \cdot (\nabla \times \mathbf{N}_j) \\ -(i\mathbf{k} \times \mathbf{N}_j) \cdot (\nabla \times \mathbf{N}_i) + (\mathbf{k} \times \mathbf{N}_i) \cdot (\mathbf{k} \times \mathbf{N}_j) \end{array} \\
= \; & \begin{array}{ll} (\nabla \times \mathbf{N}_i) \cdot (\nabla \times \mathbf{N}_j) & \rightarrow \mathbf{S} \\ + i\mathbf{k} \cdot \left[(\mathbf{N}_i \times \nabla \times \mathbf{N}_j) - (\mathbf{N}_j \times \nabla \times \mathbf{N}_i)\right] & \rightarrow i\mathbf{k} \cdot \mathbf{P} \\ + k^2 \mathbf{N}_i \cdot \mathbf{N}_j & \rightarrow k^2 \mathbf{T} \\ -(\mathbf{k} \cdot \mathbf{N}_i)(\mathbf{k} \cdot \mathbf{N}_j) & \rightarrow \mathbf{k}^T \mathbf{J}\, \mathbf{k}. \end{array}
\end{aligned}
\tag{2.37}
$$

We can now formulate the generalised eigenvalue equation in terms of the wave vector, **k**, and the component matrices, **S**, **P**, **T** and **J**.

$$
\begin{aligned}
& \mathbf{A}(\mathbf{k})x = \lambda \mathbf{B}x \\
& \mathbf{A}(\mathbf{k}) = \mathbf{S} + i\mathbf{k} \cdot \mathbf{P} + k^2 \mathbf{T} - \mathbf{k}^T \mathbf{J}\mathbf{k} \\
& \mathbf{B} = \mathbf{T}
\end{aligned}
\tag{2.38}
$$

Hence, in generating the eigenvalue equation we need to perform the integration presented in equation (2.39) to generate the necessary elemental matrices. The equations can all be integrated numerically; for the complete derivations of these matrices, see Appendix F:

$$
\begin{aligned}
T_{ij} &= \int_\Omega \mathbf{N}_i \cdot \mathbf{N}_j \, d\Omega \\
S_{ij} &= \int_\Omega (\nabla \times \mathbf{N}_i) \cdot (\nabla \times \mathbf{N}_j) \, d\Omega \\
P_{ij} &= \int_\Omega (\mathbf{N}_i \times \nabla \times \mathbf{N}_j) - (\mathbf{N}_j \times \nabla \times \mathbf{N}_i) d\Omega \\
J_{ij} &= \int_\Omega (\mathbf{k} \cdot \mathbf{N}_i)(\mathbf{k} \cdot \mathbf{N}_j) d\Omega
\end{aligned}
\tag{2.39}
$$

2.9 Assembly of the System of Equations

The elemental matrices have to be assembled into a set of global matrices, taking the solution over single elements and combining them to give the solution over the entire domain. This can be described mathematically as

$$\mathbf{K} = \sum_{e=1}^{M} \mathbf{K}^e \tag{2.40}$$

Where $\mathbf{K}$ is the global matrix, e refers to the global element number, M is the total number of elements in the domain and $\mathbf{K}^e$ is the elemental matrix. This matrix summation requires a mapping between global and local node numbers so the elements of $\mathbf{K}^e$ can be inserted into the correct position in the global matrix $\mathbf{K}$.

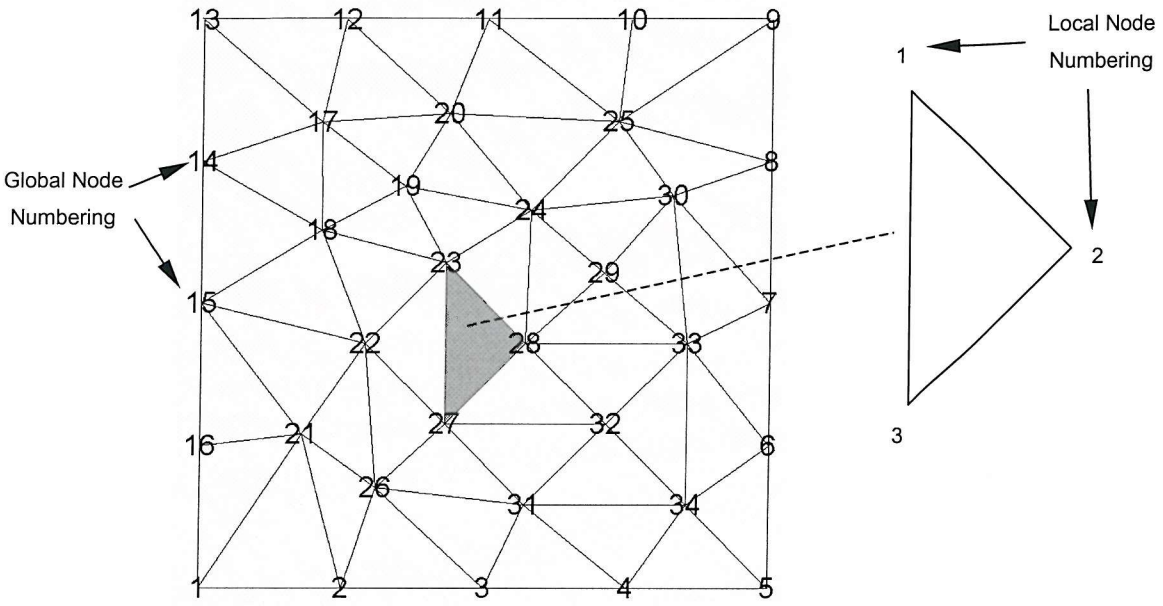

Figure 2-8 Global and local node numbering.

Figure 2-8 illustrates the link between an individual element and its position in a mesh. For each element, we store the local to global node number mappings as illustrated in Table 2-2.

Local Node Number	Global Node Number
1	23
2	28
3	27

Table 2-2 Local to global node map.

Therefore when the elemental matrix $\mathbf{K}^e$ is assembled into $\mathbf{K}$, element $K^e_{(1,1)}$ is summed into element $K_{(23,23)}$ and so on as depicted in Figure 2-9.

$$\begin{bmatrix} K^e_{(1,1)} & K^e_{(1,2)} & K^e_{(1,3)} \\ K^e_{(2,1)} & K^e_{(2,2)} & K^e_{(2,3)} \\ K^e_{(3,1)} & K^e_{(3,2)} & K^e_{(3,3)} \end{bmatrix} \quad \Rightarrow \quad \begin{bmatrix} K_{(23,23)} & K_{(23,28)} & K_{(23,27)} \\ K_{(28,23)} & K_{(28,28)} & K_{(28,27)} \\ K_{(27,23)} & K_{(27,28)} & K_{(27,27)} \end{bmatrix}$$

Figure 2-9 Local to global matrix elements.

The structure of the global matrices is therefore highly dependent on the global numbering scheme. It is beneficial to number nodes such that their difference in an element is minimised. This reduces the bandwidth of the resulting diagonal matrices thereby increasing the efficiency with which the resulting eigenvalue problem can be solved (Fagan 1992).

2.10 Reciprocal Lattice Space and the Brillouin Zone

The periodicity of the crystal lattice allows us to model a crystal of infinite extent by considering only the unit cell, an area bounded by the lattice vectors, as illustrated in Figure 2-10.

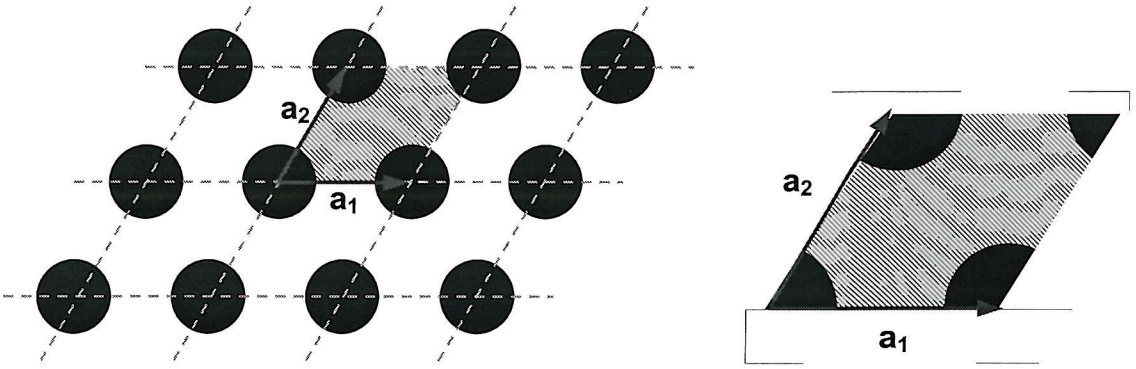

(a) (b)

Figure 2-10 A two-dimensional crystal lattice (a) and the corresponding unit cell (b). The lattice vectors, $\mathbf{a}_1$ and $\mathbf{a}_2$ are highlighted with arrows.

A crystal can be described by the function $\varepsilon(\mathbf{r})$ which represents the permittivity at spatial position $\mathbf{r}$. The crystal's periodic structure means it is invariant under any translation equal to an integral multiple of the lattice vectors. This periodicity can be stated mathematically as:

$$\varepsilon(\mathbf{r}) = \varepsilon(\mathbf{r} + m\mathbf{a}_1 + n\mathbf{a}_2), \tag{2.41}$$

where $\mathbf{a}_1$ and $\mathbf{a}_2$ are the lattice vectors and m and n are integer values.

It is the periodic nature of the crystal lattice that allows the application of Bloch's theorem

(Equation (2.25)). This states that the allowable electromagnetic modes can be represented by a plane wave modulated by a function, **u**, which has the same periodicity as the lattice. This theorem introduces the wave vector, **k**, as a parameter for the magnetic field intensity. The set of these wave vectors exist in reciprocal lattice space, a concept that is fundamental to solid state physics (Kittel 1986).

Reciprocal lattice vectors define reciprocal lattice space in the same way that real-space lattice vectors define the crystal lattice. The reciprocal lattice vectors (e.g. $\mathbf{b}_1$ and $\mathbf{b}_2$) are computed as a function of the real-space lattice vectors (e.g. $\mathbf{a}_1$ and $\mathbf{a}_2$) according to equation (2.42). The direction of the reciprocal lattice vectors is dictated by the Kronecker-delta operator that dictates $\mathbf{a}_1$ and $\mathbf{b}_2$ are orthogonal as are $\mathbf{a}_2$ and $\mathbf{b}_1$.

$$\mathbf{a}_i \mathbf{b}_j = 2\pi\delta_{ij} . \tag{2.42}$$

The magnitude of the reciprocal lattice vectors can be computed simply as,

$$|\mathbf{b}_i| = \frac{2\pi}{|\mathbf{a}_i| \cos\theta}, \tag{2.43}$$

where θ is the angle between the lattice vectors. The crystal lattice and its reciprocal are illustrated in Figure 2-11.

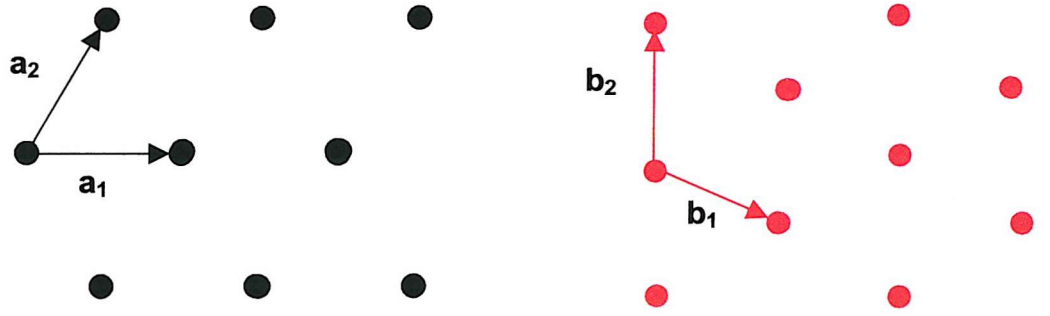

(a) (b)

Figure 2-11 Lattice vectors in real space (a) and reciprocal lattice space (b). The direction and magnitude of the reciprocal lattice vectors are governed by equations (2.42) and (2.43) respectively.

The periodicity of the crystal lattice allows us to consider only the unit cell when modelling a crystal of infinite extent. In the same way, we need only consider the set of **k**-vectors that are contained within the 'unit-cell' in reciprocal lattice space. This set is said to lie within the 1st Brillouin zone in reciprocal lattice space, a region in which all wave vectors are unique and

cannot be reached via translation by an integer product of the reciprocal lattice vectors. Hence, when computing the allowable modes as a function of the wave vector we need only consider values of **k** that lie within the 1st Brillouin zone.

The Brillouin zone can be constructed by extending lines between a reciprocal lattice point and its nearest neighbours. The perpendicular bisectors of these lines are then taken with the area enclosed by these bisectors being the 1st Brillouin zone. The presence of symmetries within the Brillouin zone allows the domain of **k** to be reduced further to avoid redundant **k** vectors that produce degenerate modes. Thus we form an irreducible Brillouin zone that cannot be subdivided by the lines of symmetry. The Brillouin zone construction and irreducible Brillouin zone are shown in Figure 2-12 (a). The dimensions of the Brillouin zone are given in Figure 2-12 (b) as a function of the real-space lattice pitch length, a.

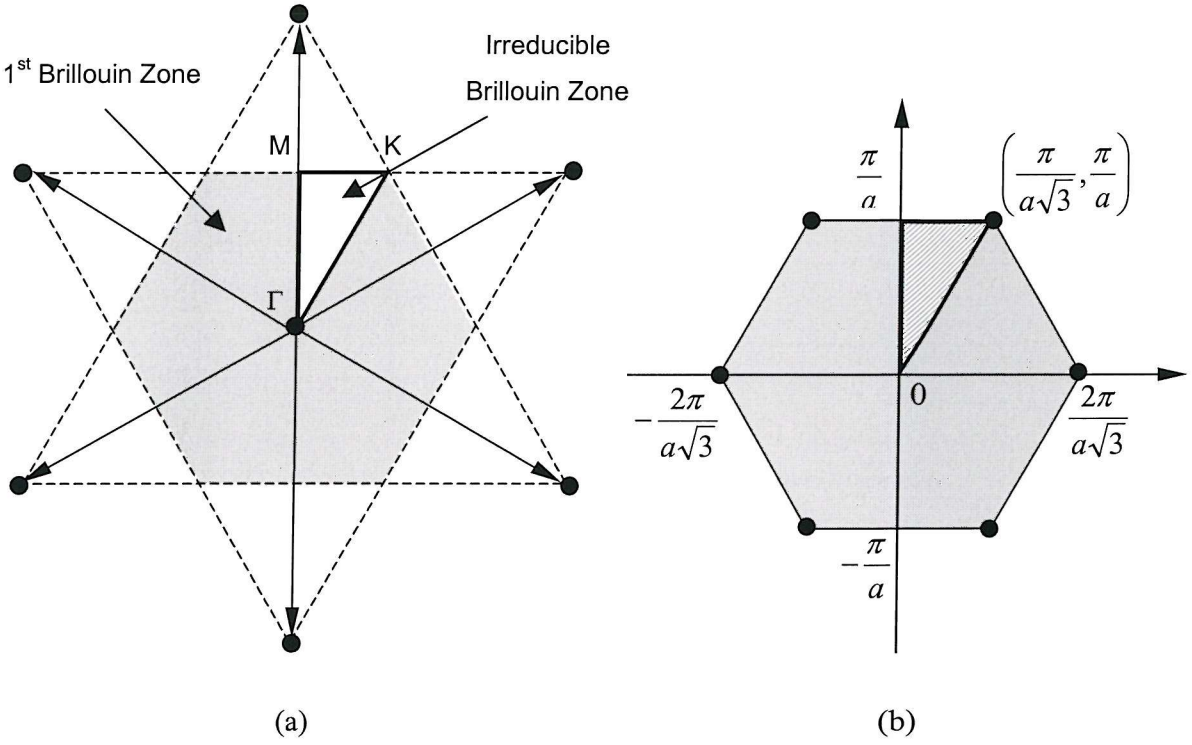

(a) (b)

Figure 2-12 Brillouin zone construction for a triangular lattice (a) Dimensions of the Brillouin zone in terms of the real-space lattice pitch length (b). The 1st Brillouin zone is highlighted in grey with the irreducible Brillouin zone cross-hatched.

So in order to solve the original generalised eigenvalue problem as a function of **k**, the domain of **k** is the irreducible Brillouin zone. Wave vectors within this area will produce unique (non-degenerate) solutions, the set of which formulate the spectrum of the photonic crystal. In practice, one can sample a discrete number of points along a path describing the perimeter of

this irreducible Brillouin zone or a sample distribution of points can be taken from the area.

For each position in reciprocal lattice space (e.g. each wave vector, **k**) we can compute n bands of ascending frequency, as these are the lowest n eigenvalues. This allows the modes to be classified by their wave vector, **k**, and the band number, n, i.e. $\mathbf{H}(\mathbf{k}, n)$.

Let $\lambda_n(\mathbf{b})$ be the n^{th} eigenvalue at a given wave vector, **k**. A plot of these eigenvalues as one moves around the Brillouin zone produces a band diagram (see 2.12 Data Visualisation), effectively the spectrum of the original problem.

When dealing with a true unit cell, defined to be a cell of the smallest area possible necessary to describe that crystal structure, we can choose a set of **k**-vectors that describe a path around the irreducible Brillouin zone as described previously. However, for cases in which a true unit cell is not used, for example when investigating super-cells incorporating defects and cells without nice symmetries, a convenient Brillouin zone path is not always easily available. In these cases we can choose the set of **k**-vectors in a quasi-random fashion from the area contained within the first Brillouin zone. A Sobol sequence (Press, Teukolsky et al. 1999) is utilised to ensure that the chosen vectors are evenly distributed within the prescribed area, as shown in Figure 2-13 (a). The vectors are subsequently sorted such that adjacent vectors as found in the file are also adjacent in reciprocal lattice space as highlighted in Figure 2-13 (b), this ensures that the similarity of adjacent solutions can still be exploited in the eigenvalue solver. In this way, one can reconstruct the spectra of a PC without having to construct a path in reciprocal lattice space.

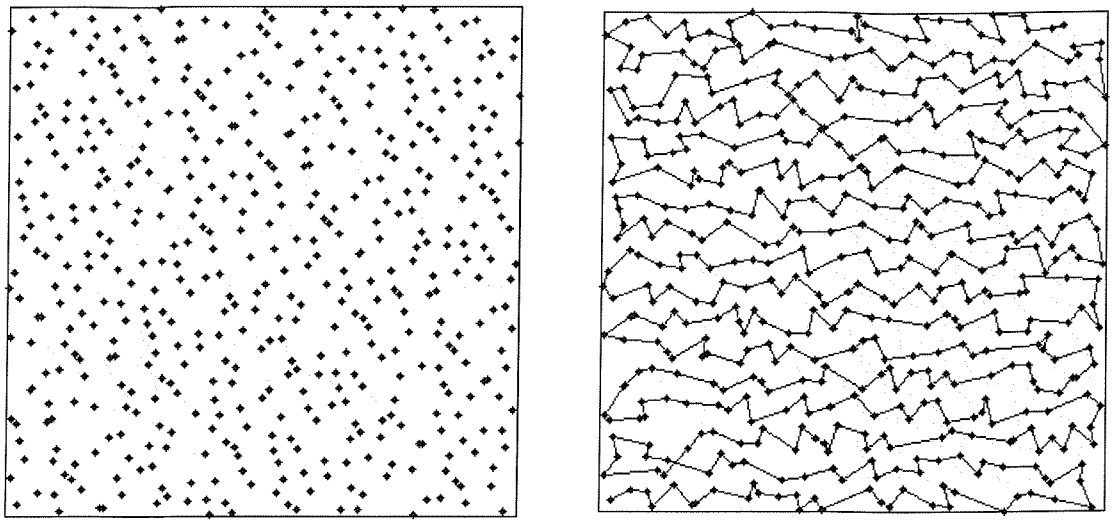

(a) (b)

Figure 2-13 A Sobol sequence; a quasi-random distribution of points (a) and the linking of adjacent points highlighting their close proximity (b).

2.11 Solution of the System of Equations

Assembly of the elemental matrices gives rise to a generalised eigenvalue problem. This is solved using a subspace iteration technique to determine a given number of least dominant eigenvalues, along with their corresponding eigenvectors. The method is based on a combination of the power method (Jennings 1977), where several vectors are iterated upon simultaneously, and the properties of the Rayleigh quotient (Bathe and Wilson 1976; Sehmi 1989). Conversion to the standard eigenvalue format is not required, so full advantage can be taken of the sparsity and symmetries of the matrices. Using this method, a number of simple but effective optimisations can be employed.

- Calculation of only the physically relevant eigenvalues: typically, the pertinent information is contained in the lowest 10 eigenvalues and the vast majority need not be found.

- Exploitation of the similarity of adjacent solutions: When calculating band diagrams, a series of similar eigensystems needs to be solved. By feeding in the solution of one eigensystem as the initial guess for the subspace search of the next system, the number of iterations required for convergence is significantly reduced.

- Searching a larger subspace than strictly necessary: The subspace iteration converges rapidly to the most dominant eigenvectors in the subspace but struggles to find the least

dominant ones. This difficulty in converging to the last components can be avoided by searching a slightly larger subspace and neglecting to find the final, difficult, eigenvectors.

2.12 Data Visualisation

Having assembled the **A** and **B** matrices and then solved the resulting eigensystem, equation (2.9), as a function of the wave vector, **k**, we are left with a set of eigenvalues and corresponding eigenvectors that need to be visualised.

$$\mathbf{A}(\mathbf{k})x = \lambda \mathbf{B}x \tag{2.9}$$

The subspace iterative eigenvalue solver allows a specific number, n, of the least dominant eigenvalues to be computed for each **k** vector in reciprocal lattice space. Hence we have $n \times \mathbf{k}$ eigenvalues and their eigenvectors, which can be categorised as follows:

$$\begin{matrix} \lambda_n(\mathbf{k}) \\ x_n(\mathbf{k}) \end{matrix} \tag{2.10}$$

The values of interest are the frequencies of the allowable electromagnetic modes. Due to the scaling properties of Maxwell's equations as discussed previously in chapter 2.3, these frequencies are presented in dimensionless units, $\omega a/2\pi c$, where ω is the frequency, a, is the length of the unit cell and c is the speed of light. This normalises the spectra for a given photonic crystal irrespective of its scale. The conversion from eigenvalue to dimensionless frequency is straightforward:

$$\left(\frac{\omega a}{2\pi c}\right)_n (\mathbf{k}) = [\lambda_n(\mathbf{k})]^{\frac{1}{2}} \cdot \frac{a}{2\pi}. \tag{2.11}$$

The 'band structure' is contained in this data set. If the discrete set of wave vectors has been chosen such that they form a coherent path around the irreducible Brillouin zone the band structure can be plotted as a band diagram, also known as a dispersion relation (Figure 2-14). The normalised frequencies of the modes are plotted against the wave vector. If a photonic band gap exists for the photonic crystal being modelled this will be seen as a frequency range that is not intersected by any of the bands.

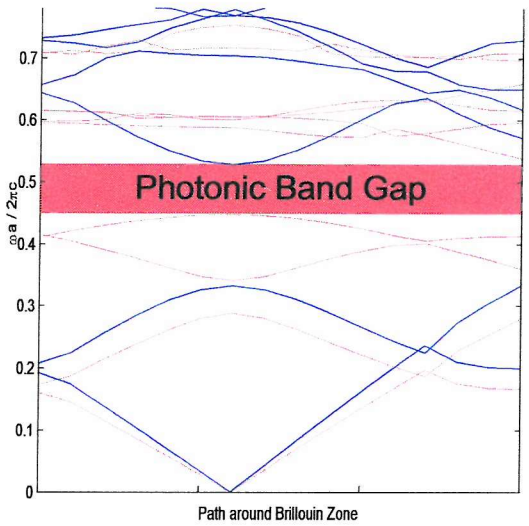

Figure 2-14 Example of a band diagram for a photonic crystal. The frequency range that none of the bands intersect is highlighted, this represents a photonic band gap.

The mode frequencies can also be visualised as a density of states diagram, an example of which is presented in Figure 2-15. This is a histogram of the frequency density of eigenvalues against the normalised frequency, e.g. $\omega a/2\pi c$ is plotted along the x-axis with the frequency density along the y-axis. This is a useful data representation as it clearly shows any band-gaps. These are simply frequency ranges where the density drops to zero.

Density of states diagrams are particularly useful when modelling crystal structures for which a true unit cell is not used, for example when investigating super-cells incorporating defects or cells without symmetries. In these cases a convenient Brillouin zone path is not always easily constructed and instead a 'Monte-Carlo' approach (Newman and Barkema 1999) to wave vector selection is taken, for example, the quasi-random selection of vectors based on a Sobol sequence. The discontinuity in **k** prevents the band diagram from being a useful representation of the data hence a density of states diagram is the preferred method of presentation.

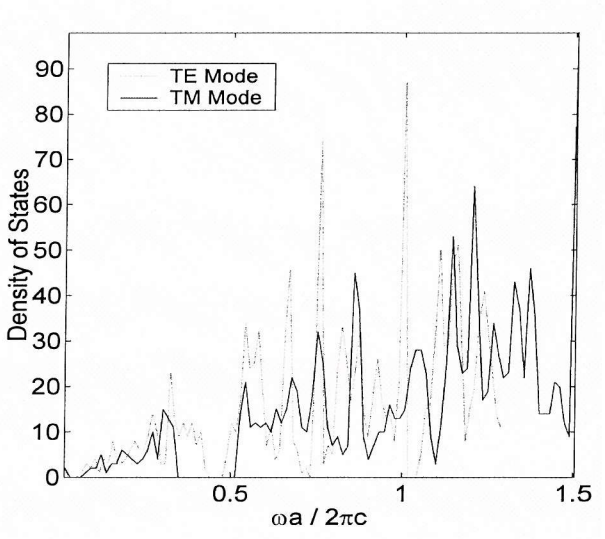

Figure 2-15 Example of a density of states diagram for a photonic crystal. The frequency range for which the density of states drops to zero represents a photonic band gap.

For many photonic crystal structures band gaps appear only for a specific range of filling fractions; thus by varying the rod radius (r) whilst keeping the pitch (a) constant one can determine where the band gaps exist in the form of a 'gap map', see Figure 2-16. The rod to pitch ratio (r/a) is represented on the x-axis and the normalised frequency, $\omega a/2\pi c$, is represented on the y-axis. The presence of TE and TM band gaps are then plotted on to these axes. The benefit of visualising the band structure in this way is that it clearly highlights where any complete band gaps appear and where their size is greatest.

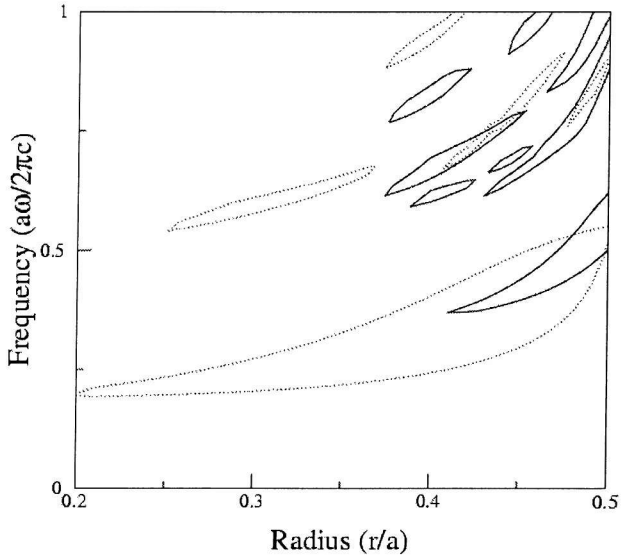

Figure 2-16 Example gap-map for a triangular lattice plotting the band-gap frequency ranges for both the TE(dashed) and TM (solid) modes against the rod radius.

For each eigenvalue, there is a corresponding eigenvector. Each eigenvector represents an allowable mode of propagation through the photonic crystal. The values that comprise the eigenvector are proportional to the field intensity at the corresponding node positions in the mesh, e.g. for the eigenvector x in equation (2.9) the value, x_i, represents the field intensity at the i^{th} node in the mesh. Hence, for two-dimensional meshes, the modes of propagation can be visualised as a surface plot of the eigenvectors based on the mesh representation of the crystal, e.g. Figure 2-17.

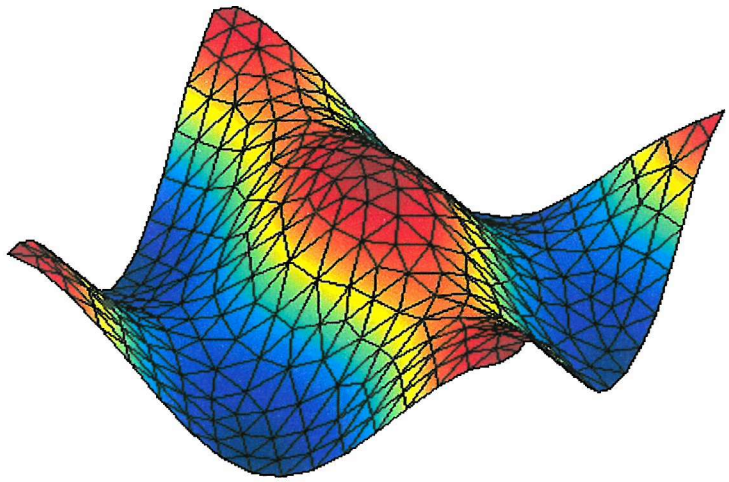

Figure 2-17 Example of a field intensity plot. The magnitude of the field is plotted at mesh node points.

2.13 Comments on the FEM

The FEM has several advantages over traditional plane-wave expansion techniques and FD methods.

- The photonic crystal unit cell is represented by a two-dimensional triangular or three-dimensional tetrahedral mesh. This simple and intuitive representation of the domain allows arbitrary and complex crystal structures to be modelled more directly than the Fourier transform representation used in the plane wave method.

- Each triangle (element) stores its dielectric constant. Hence, the inherent discontinuities in the dielectric constant between materials can be expressed accurately. This is not the case in the plane wave method where Gibbs phenomena associated with the truncated

Fourier representation of $\varepsilon(\mathbf{r})$ can affect the accuracy of the computation (Villeneuve and Piche 1994).

- The domain discretisation need not be regular as opposed to the meshes most usually used in FD methods. This allows irregular meshes to be used that may well model the detailed physical PC structure more naturally.

- The FEM gives a piecewise continuous solution rather than the point-wise counterpart generated from FD techniques. This means that the way in which the solution varies over an element is an integral part of the FEM as opposed the discrete point based solution provided by FD methods.

- Self-adaptive mesh refinement (Thompson, Soni et al. 1999; Molinari, Cox et al. 2001) enables the mesh quality to be improved in areas of high relative error. This can significantly increase the solution accuracy for minimal additional computational cost. This is far harder to perform using FD methods, where commonly the whole domain discretisation has to be refined to improve the solution quality.

- The FEM can be adjusted for the three-dimensional vector case. This has the advantage of enforcing the correct continuity requirements between elements so that spurious modes are avoided; this is covered in more detail later in this report (Section 2.5).

- The **A** and **B** matrices in the resultant eigenvalue problem are sparse, allowing memory and processor requirements to scale with $O(n)$ rather than $O(2n^d)$ (d is the number of dimensions) for plane wave expansion techniques. This sparseness arises from the topology of the mesh, with each node connected to, on average, six other nodes in two dimensions. This leads to only six values per matrix row. This is not the case in the plane wave method where dense matrices store the coefficients of the Fourier expansion terms. Each matrix value holds a coefficient thus the resulting matrices are dense. This is the major advantage of the FEM, making modelling of complex 2-dimensional and particularly 3-dimensional PBG structures feasible (Pissanetsky 1984). Figure 2-18 clearly depicts the sparsity of the assembled global matrices. It represents an 800 x 800 **A** matrix (Equation (2.17)) with dots representing the non-zero elements.

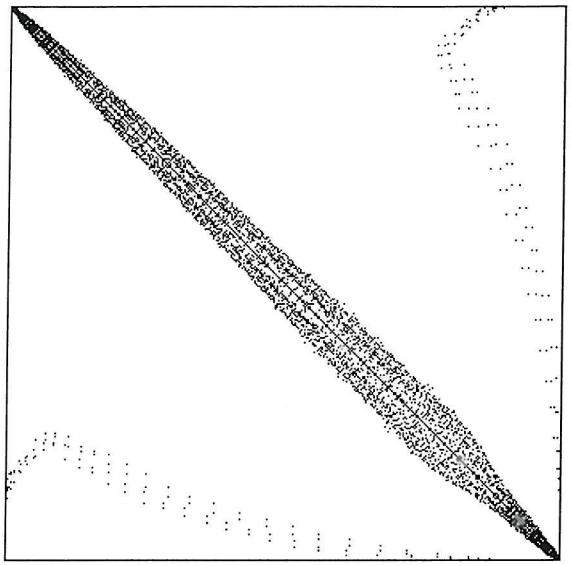

Figure 2-18 Sparse Global Matrix: 800 x 800 = 640, 000 elements. 12460 non-zero elements gives a sparsity of approximately 2%.

The accuracy of solution produced by the FEM is closely related to the number of interpolatory nodes in the model. Increasing the number of interpolatory nodes improves the quality of solution, but at the expense of increased computational cost. The number of interpolatory nodes can be controlled in two ways. Firstly, and most trivially, the domain can be subdivided into a greater number of smaller elements; this is known as *h*-refinement. Computing the solution over a smaller element will give a better approximation to the true solution since the 'resolution' of the solution is improved.

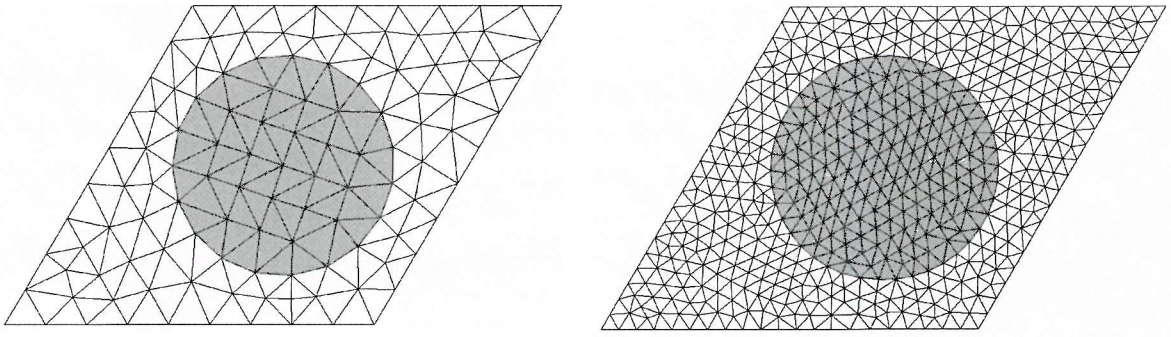

(a) (b)

Figure 2-19 h-*refinement for a triangular lattice unit cell. Mesh (a) is composed of 200 elements, mesh (b) is composed of 1000 elements.*

Secondly, the order of interpolation can be increased, increasing n where an n^{th} degree polynomial is being used to approximate the solution over an element. This is also known as *p*-refinement. A greater flexibility in the interpolation function comes at the cost of an increase in

the number of interpolatory nodes and hence an increase in the number of interpolation functions. In 2-dimensions, the number of interpolation functions for a given interpolation order increases as the triangular numbers, e.g. 3, 6, 10, 15 for orders 1, 2, 3, 4 (see Section 2.2). For good quality meshes the ratio of number of interpolation nodes to the total number of elements in the mesh for an interpolation order p, is approximately $p^2/2$. The relative benefits and costs of h and p refinement, in the context of a two dimensional treatment of photonic crystal modelling, are investigated later in this report (see Section 4.2). In the next chapter we use the code we have developed to compute the band structure for a variety of common photonic crystal structures and we compare our results with those obtained from other sources, including plane wave expansion techniques, finite difference methods and experimental data.

3 Results

In order to validate the FE code it is necessary to perform analyses of dielectric structures that can be compared with other results presented in the literature. These results can be either theoretical or experimental. The theoretical results can be further divided into true (analytical) and approximate (numerical) solutions. This section presents FE solutions for comparison with those structures that can be represented and solved analytically, and for several other common structures that have been examined numerically using other techniques, for example, plane wave expansion and finite difference methods. FE analyses are also presented for comparison with experimental data.

3.1 Comparison with Analytical Results

The propagation mode frequencies for free-space can be calculated analytically according to equation (3.1). The frequency, λ, is computed as a simple function of the wave vector, $\mathbf{k}$, and the reciprocal lattice vector, $\mathbf{G}$. The derivation of this equation can be found in Appendix D:.

$$\lambda = \left[i(\mathbf{G}+\mathbf{k})\right]^2 = (\mathbf{G}+\mathbf{k})^2, \tag{3.1}$$

This result can be used to verify that the FE code is producing a good approximation to the correct solution in this case.

The unit cell representation for free-space is arbitrary so long as periodic boundary conditions are enforced and the dielectric constant for all elements is set to one ($\varepsilon_{air}=1$). For simplicity, a square unstructured triangular mesh representation is used as shown in Figure 3-1.

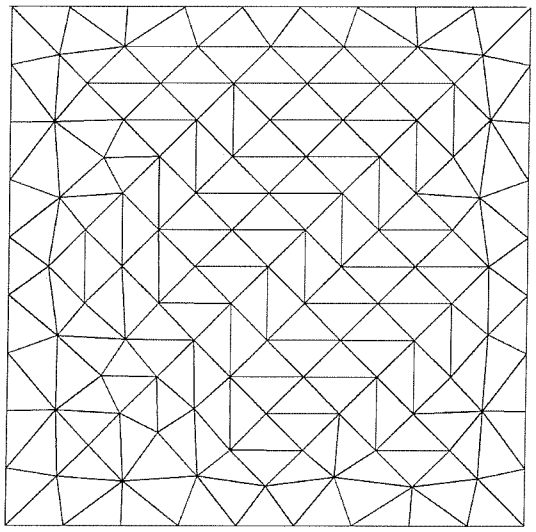

Figure 3-1 Unstructured triangular mesh representation of a square free-space unit-cell.

The FE and analytical band diagrams are presented in Figure 3-2. The band frequencies range between 0 and 2 on a normalised frequency scale and the wave-vector, **k**, is sampled from a path circulating the irreducible Brillouin zone (see chapter 2.12). Overall, the band diagrams show excellent agreement; slight inconsistencies are present but these are to be expected due to the approximate nature of the FE solution.

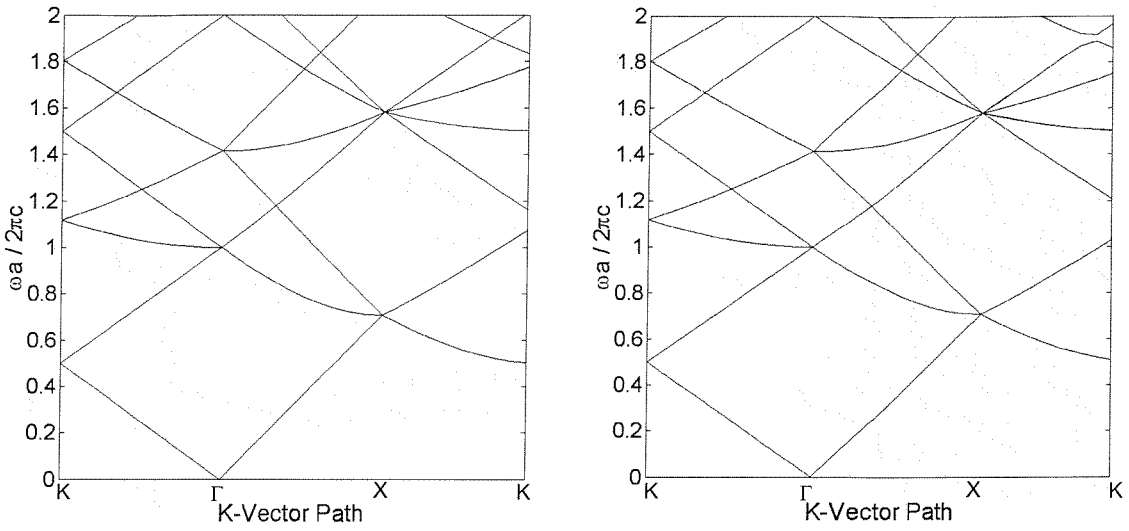

Figure 3-2 Analytical, (a), and Finite element, (b), free-space band diagrams.

3.2 Comparison with Numerical Results

Many photonic crystal structures have been examined theoretically using other numerical methods (see chapter 1.1) (Axmann, Kuchment et al. 1999). Further validation of the FE code can be made by comparing analyses of equivalent structures to those found in the literature.

Photonic crystals that are invariant in one dimension and periodic in the remaining two are commonly based on an arrangement of cylindrical rods in a substrate as shown in Figure 3-3.

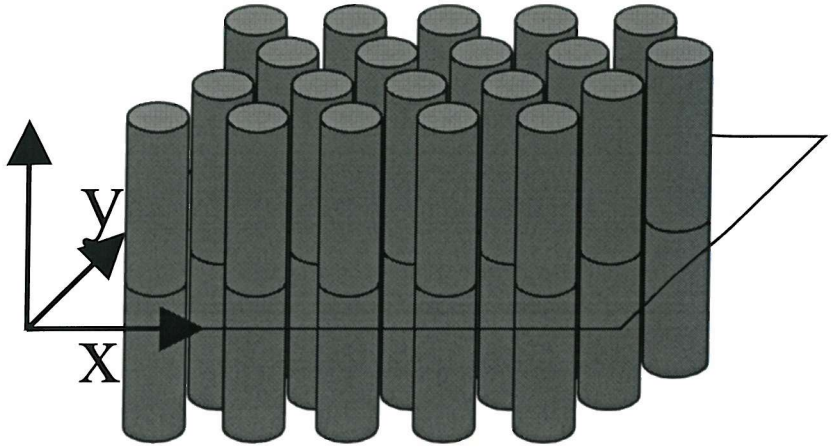

Figure 3-3 A typical two-dimensional photonic crystal structure consisting of cylindrical rods arranged periodically in a substrate material.

Two such arrangements that have been well studied are the square and triangular lattices, the geometries of which are shown in Figure 3-4 and Figure 3-6 respectively. Circular rods are arranged in a background material such that their centres are positioned at the lattice points. The unit-cell can be derived from the lattice as the area bound by the lattice vectors. This is the maximum area after which the structure repeats periodically. The unit cell structure is approximated with an unstructured triangular mesh representation. Figure 3-4 and Figure 3-6 show these unit-cells and examples of how the unit-cells are tiled to recreate the crystal structure, note that the mesh boundary vertices must be periodic in order for the cells to tile correctly.

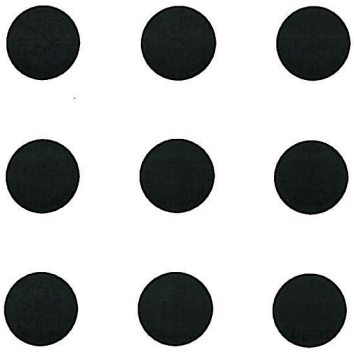

(a)

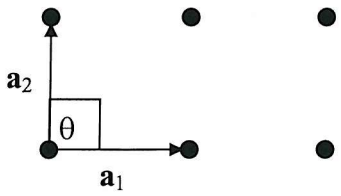

$|\mathbf{a}_1| = |\mathbf{a}_2|. \quad \theta = 90°$

(b)

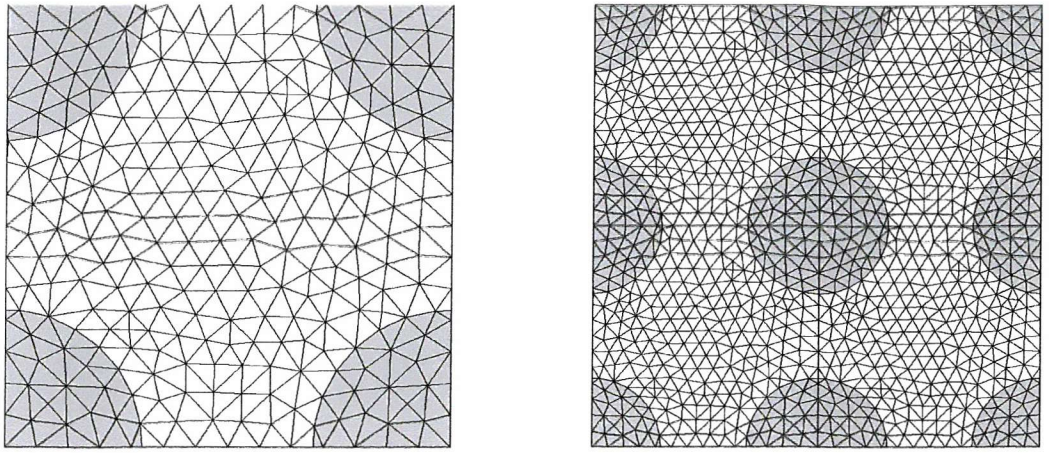

(c) (d)

Figure 3-4 Square lattice rod arrangement (a) and the square lattice geometry (b). Single (c) and tiled (d) unit-cells for a square crystal lattice of rods in a substrate material.

The band structure for a square lattice of alumina rods in air with a filling rod to pitch (*r/a*) of 0.2 was computed using the FE code and can be seen in Figure 3-5. Comparison with the equivalent analysis as presented in (Joannopoulos, Meade et al. 1995) shows excellent agreement. The key feature of the diagram is the large band gap in the TM mode between the 1st and 2nd bands. A complete band gap does not appear for this structure. This result also agrees with the plane wave calculation and experimental transmission data as presented in (Xiangdong, Zhao-Qing et al. 2001).

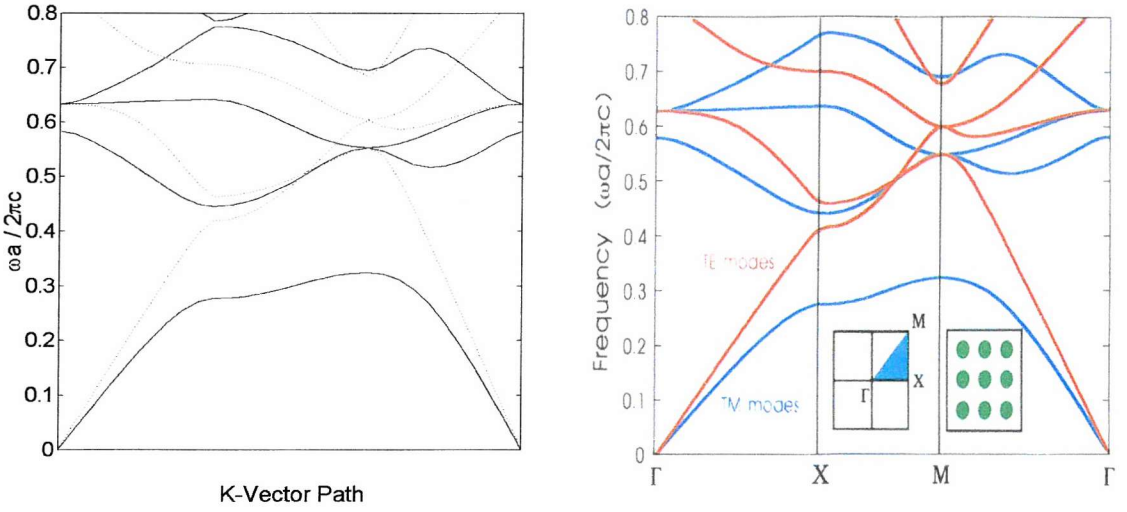

(a) (b)

Figure 3-5 Photonic band structures produced by (a) the finite element code code with the solid and dashed lines representing the TM and TE modes respectively and (b) reproduced courtesy of Joannopoulus et al. for a square lattice arrangement of alumina rods (ε=8.9) in air with a relative rod radius, r/a, of 0.2.

The triangular lattice was modelled for air rods in a gallium arsenide (GaAs) substrate material. Gallium arsenide is a widely used material in optoelectronics and for this simulation, the permittivity is considered constant at 11.4. The rod radius to pitch length ratio was 0.48. The resulting band diagram (see Figure 3-7) exhibits a large band gap in the TE polarisation between the 1st and 2nd bands stretching between 0.33 and 0.51. There is also a band gap in the TM polarisation between the 2nd and 3rd bands from 0.42 to 0.51. The frequency ranges of these gaps overlap hence the crystal produces a complete photonic band gap in both polarisations. The size of the band gap can be given but this is not a meaningful value due to the scaling properties of the underlying Maxwell equations, therefore the band gap is best described in terms of the ratio of the size of the gap to the mid-gap point, $\Delta\omega/\omega_0$. This quantity is invariant under scaling of the unit cell and for this photonic crystal structure it is 0.09/0.465 = 0.19.

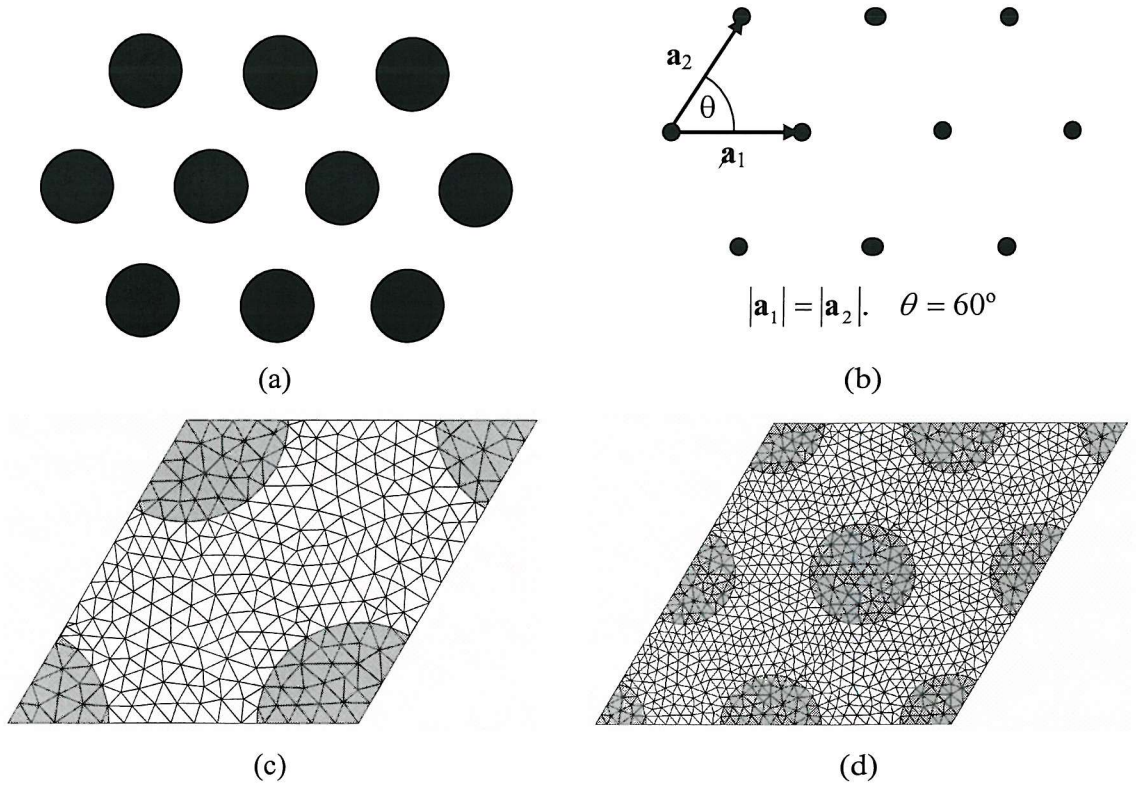

Figure 3-6 Triangular lattice rod arrangement (a) and the triangular lattice geometry (b). Single (c) and tiled (d) unit-cells for a triangular crystal lattice of rods in a substrate material.

A similar structure was analysed for comparison with the result presented in (Villeneuve and Piche 1994). Air rods with a filling fraction of 83% set in a substrate with refractive index 3.5. For a direct comparison, a different path around the reduced Brillouin zone was used. Comparison of the two band diagrams again shows excellent agreement (see Figure 3-8).

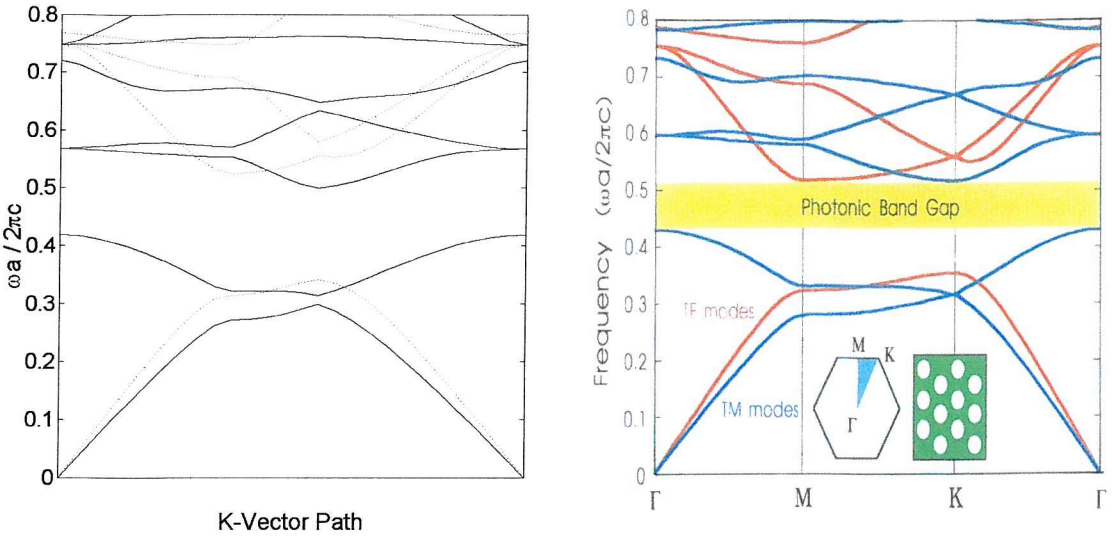

(a) (b)

Figure 3-7 Photonic band structures produced by (a) the finite element code with the solid and dashed lines representing the TM and TE modes respectively and (b) reproduced courtesy of Joannopoulus et al. for a triangular lattice arrangement of air rods with a relative radius, r/a, of 0.48 in a substrate material, ε=13.

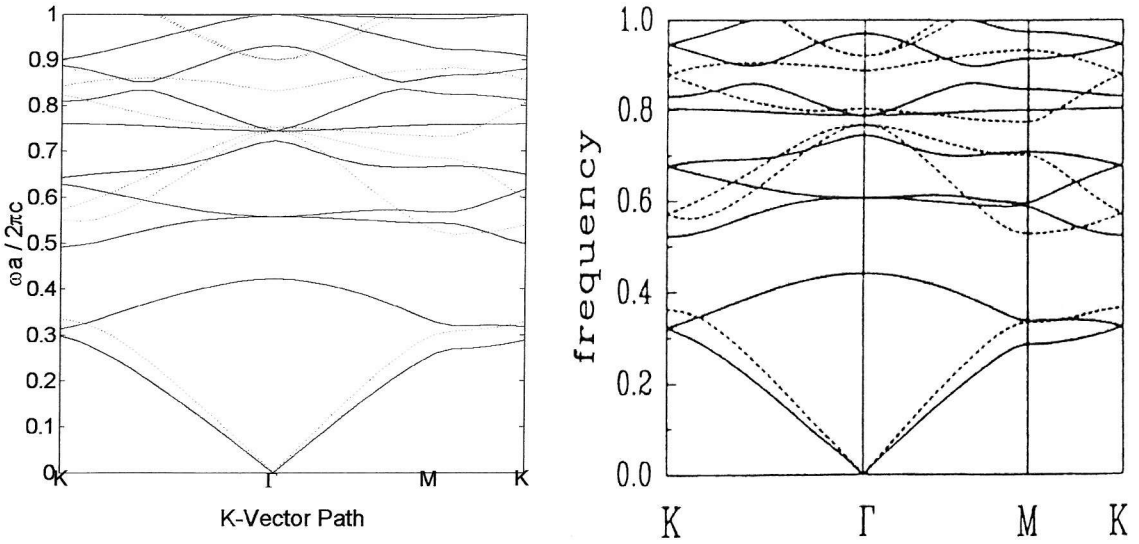

(a) (b)

Figure 3-8 Finite element analysis (a) and plane wave analysis courtesy of Villeneuve et al. (b) of a triangular lattice of air rods (filling fraction = 80%) set in a substrate with a refractive index of 3.5. The solid and dashed lines represent the TM and TE modes respectively.

A further comparison can be made with the plane wave analysis presented in (Charlton, Parker et al. 1999). The crystal structure was a triangular lattice of air rods in silicon nitride, but with a

lower filling fraction of only 30%. This reduction in the rod radius effectively closes the photonic band gap. The results of the FE analysis, presented in Figure 3-9, show excellent agreement with the plane wave analysis of the same system.

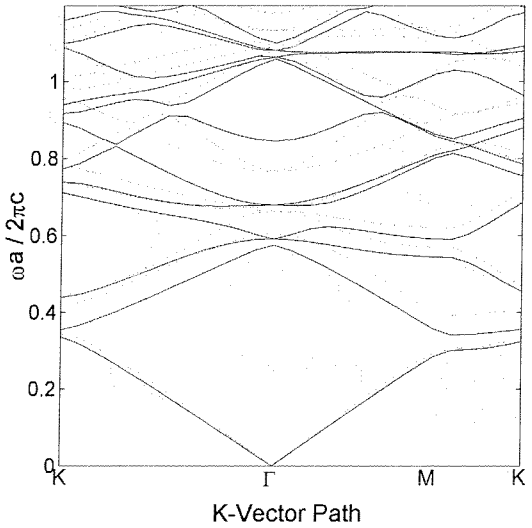

Figure 3-9 Band diagram for a triangular lattice of air rods in silicon nitride, dielectric constant = 4.0804, filling fraction = 30%.

Another photonic crystal structure commonly presented in the literature is the square array or 'woodpile'. This structure is composed of a square grid of dielectric veins as shown in Figure 3-10. The band diagram was computed for a square array of alumina ($\varepsilon = 8.9$) veins in air. The filling fraction (ratio of vein to substrate area) was 36%. The result is shown in Figure 3-11. No band gap is present for the TM polarisation but a large gap opens up in the TE polarisation between the 1st and 2nd bands with gap to mid-gap ratio, $\Delta\omega/\omega_0 = (0.41\text{-}0.33) / 0.37 = 0.22$.

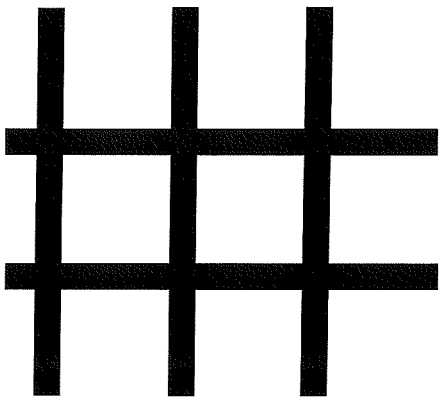

(a)

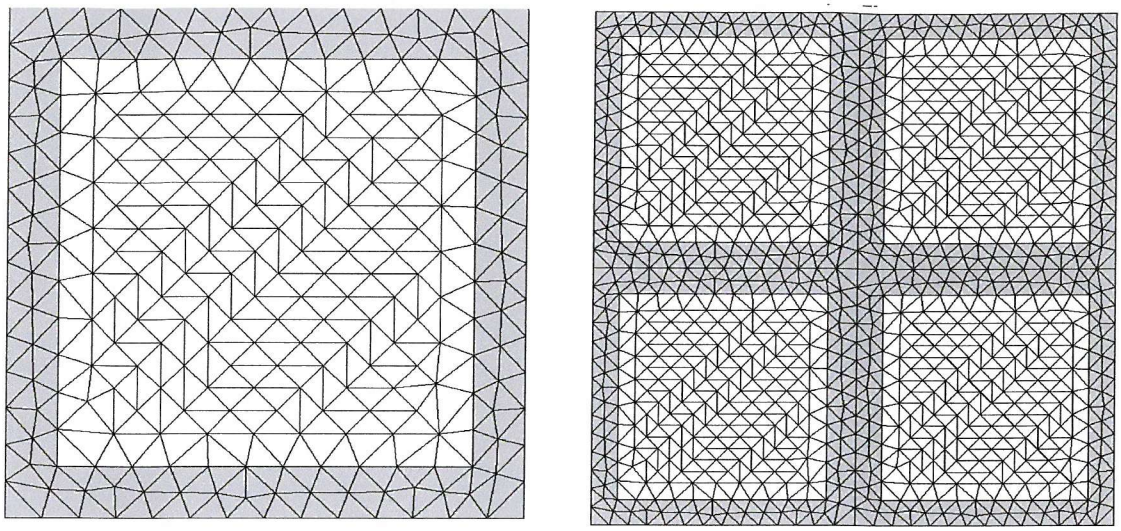

(b) (c)

Figure 3-10 (a) Square array or 'woodpile' photonic crystal structure; A square grid of dielectric veins is set in a substrate material. (b) The unit cell mesh representation and (c) an example of 4 unit cells tiled periodically.

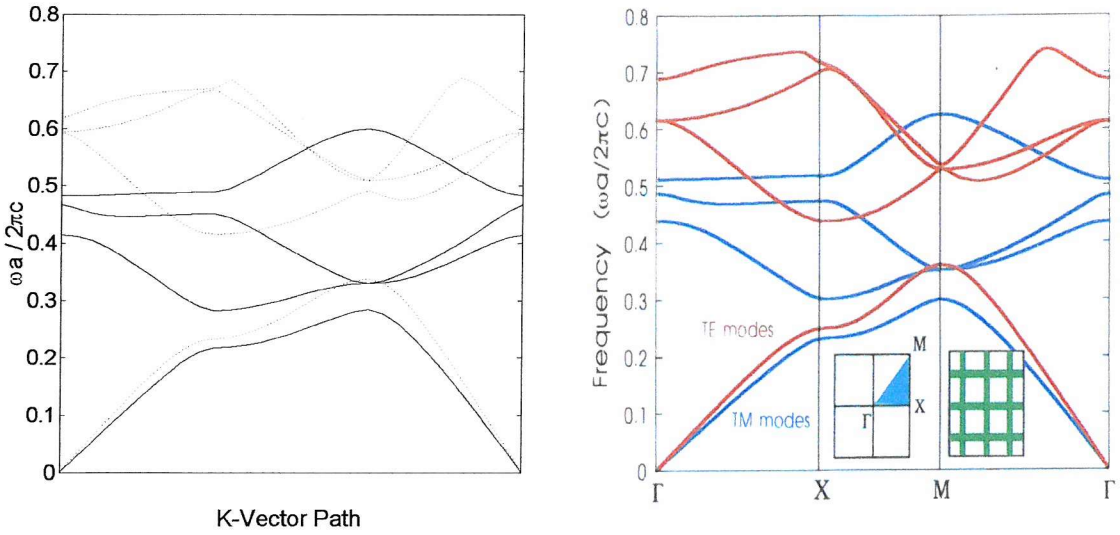

(a) (b)

Figure 3-11 Photonic band structures produced by (a) the finite element code with the solid and dashed lines representing the TM and TE modes respectively and (b) reproduced courtesy of Joannopoulus et al. for a square grid lattice of alumina (=8.9) in air, filling fraction equals 36%.

The results of our investigation into commonly modelled photonic crystal structures concur with the general rules governing the existence of band gaps as presented in (Joannopoulos, Meade et al. 1995). The key points are as follows:

- Crystal structures with disconnected areas of high dielectric constant favour band gaps

in the TM mode polarisation, as can be seen in Figure 3-5 where the crystal structure consists of disconnected rods of alumina, ε=8.9.

- Crystal structures with connected areas of high dielectric constant favour band gaps in the TE mode polarisation, as can be seen in Figure 3-11 where the crystal structure consists of a square array of connected areas of alumina.

In order to create a crystal with a complete band gap, where there is a frequency range for which both polarisations are excluded we need to combine both these characteristics. They would seem to be mutually exclusive but a compromise between the two in which a structure has areas of high dielectric constant connected by narrow veins can exhibit the desired complete photonic band gap. The obvious example of this is the triangular lattice of air rods in a high dielectric substrate, e.g. Gallium Arsenide, ε=11.4. Figure 3-12 illustrates these points for the triangular lattice.

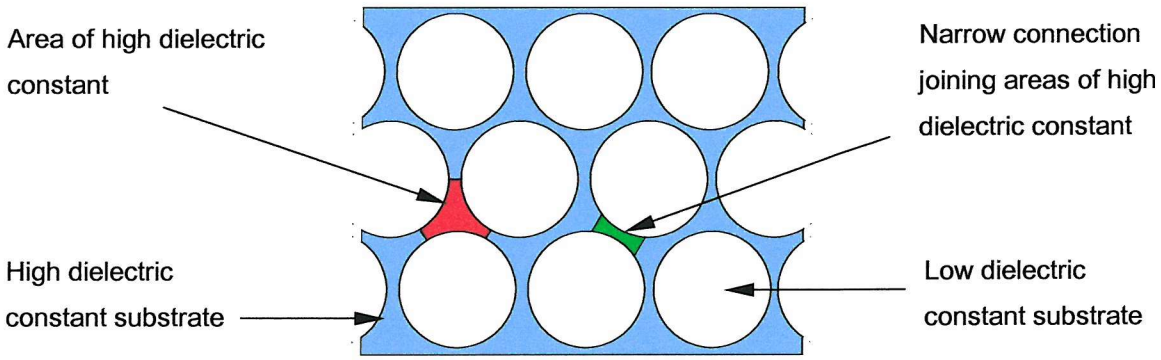

Figure 3-12 Example of a triangular lattice of air rods in a high dielectric constant substrate. Note the highlighted areas of high dielectric constant (shaded red) connected by narrow veins of substrate material (highlighted green).

3.3 Comparison with Experimental Results

Photonic crystal structures have been examined experimentally using fabricated devices and lasers (Charlton and Parker 1998; Charlton, Zoorob et al. 2000). It is important to compare experimental data with that produced using the FE code, as ultimately, if the code is not delivering an accurate representation of what is actually happening when these crystals are being used then it is of very limited real value to researchers in the field.

Transmission through a triangular lattice of air rods in gallium arsenide with a filling fraction of 80% (similar to that illustrated in Figure 3-13) has been measured, the result of which can be seen in Figure 3-14 (a), note the frequency running along the x-axis has been normalised to

allow comparison with the FEM output.

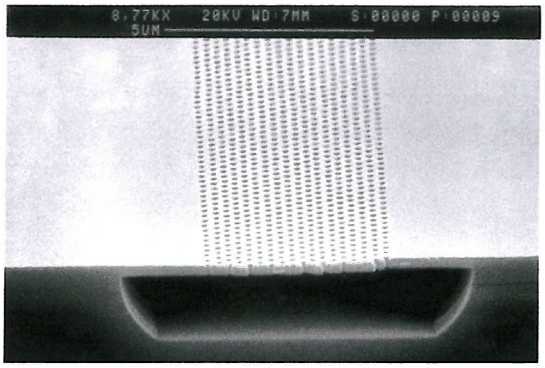

Figure 3-13 Bridge waveguide structure (pitch=300nm) courtesy of Martin Charlton, Southampton Microelectronics Research Group.

A FEM analysis of the same PC (same material and structural parameters) yields a density of states diagram also shown in Figure 3-14 (b). Comparing the transmission and density of states diagrams one can see the same key features, namely a sharp attenuation in the transmission intensity and a corresponding decrease in the density of states around a normalised frequency of 0.42. This is further proof that the FE code is providing a good approximation to the real physical system.

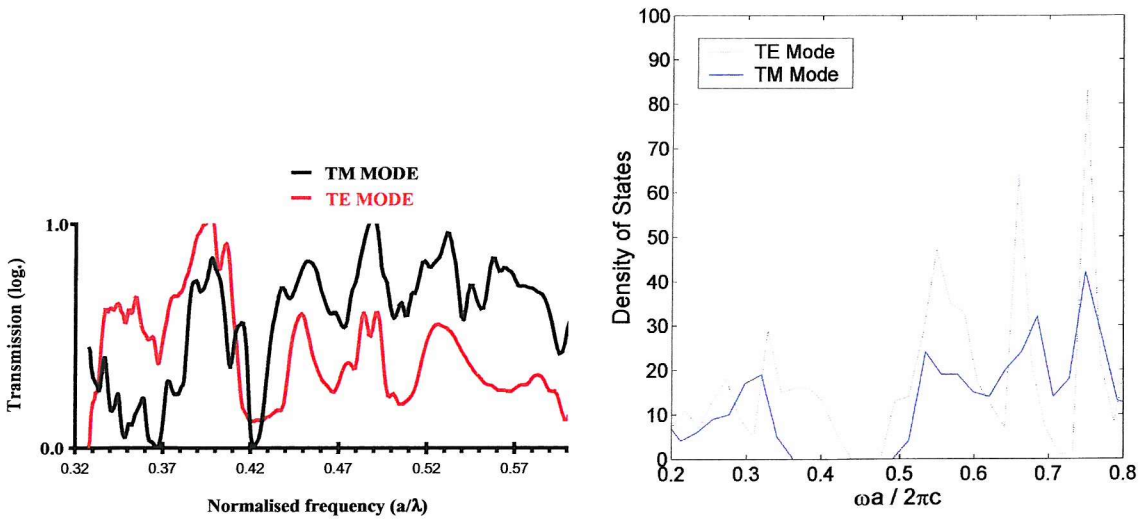

Figure 3-14 (a) Transmission diagram for a triangular lattice PC consisting of air rods in a GaAs substrate with a filling fraction of 80%. (b) FEM analysis of the same structure. A triangular lattice unit cell mesh of circular rods was used. The rod material was air (ε=1) and the substrate material was GaAs (ε=11.4).

3.4 Band Gap Maps

Several square and triangular lattice meshes were generated with rod radii to pitch length ratios

ranging from 0.06 to 0.50 in 0.02 increments. The spectra for each of these meshes were computed for air rods in a gallium arsenide (GaAs) substrate. The lowest 20 eigenvalues were computed using second order interpolation functions at 30 k-vectors sampled from a path describing the irreducible Brillouin zone. These are presented in Figure 3-15. They show excellent agreement with the equivalent data presented in (Joannopoulos, Meade et al. 1995).

For the square lattice arrangement of GaAs rods in air (Figure 3-15 (a)) there are several TM mode gaps but no TE mode gaps. The largest gap, also the lowest in frequency starts at an *r/a* of 0.1 reaches its maximum frequency width at 0.2 then disappears at 0.4. The other main gaps follow a similar pattern but they are reduced in size and shifted to the top-right of the diagram. All the gaps have disappeared when the *r/a* reaches 0.5, corresponding to the point at which the rods become connected. The square lattice of air columns in a GaAs substrate (Figure 3-15 (b)) yields both TE and TM modes gaps but for a significantly larger rod radius. Again, there is no complete band gap present.

The triangular lattice of GaAs rods in air exhibits similar but slightly larger gaps in the TM mode as were seen for the equivalent square lattice. However, this structure also has two gaps in the TE mode although these do not overlap with the TM mode gaps to give rise to a complete photonic band gap. The triangular lattice of air rods in GaAs a significant band-gap for the TE mode emerges at $r/a = 0.2$ up to 0.5. An overlapping band-gap for the TM mode gives rise to a complete band-gap from $r/a = 0.42$ to 0.5, so both polarisations are excluded in this frequency range for this photonic crystal structure. Several other smaller gaps can be seen in the normalised frequency range above 0.6 $\omega a/2\pi c$.

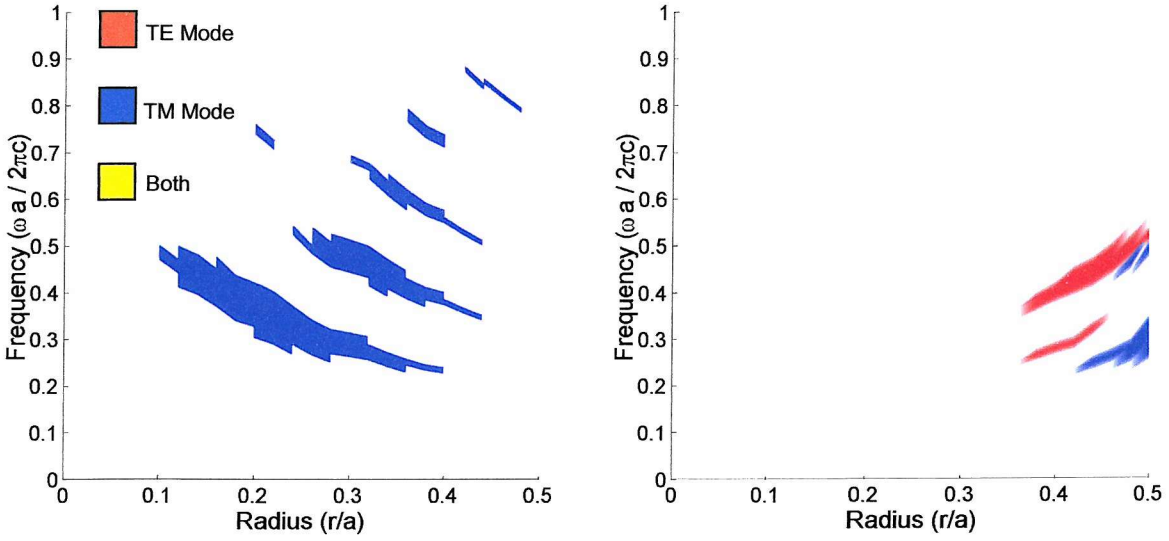

(a) (b)

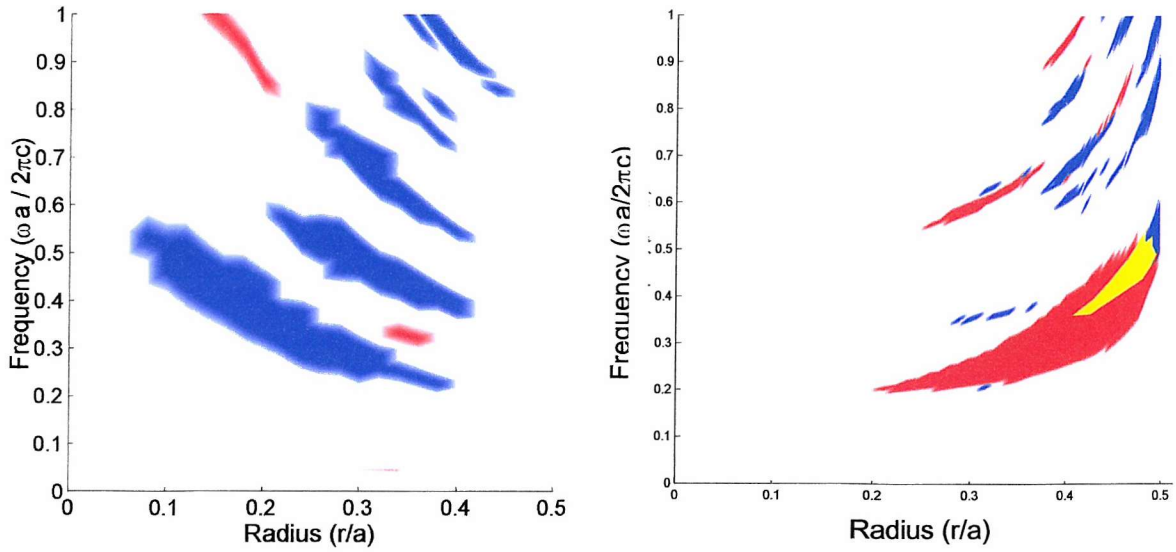

(c) (d)

Figure 3-15 Band gap maps for photonic crystal structures: (a) square lattice of GaAs rods in air (b) square lattice of air rods in a GaAs substrate (c) triangular lattice of GaAs rods in air (d) triangular lattice of air rods in a GaAs substrate. TE polarisation band gaps are highlighted in red, TM polarisation band gaps are highlighted in blue and complete band gaps are highlighted in yellow.

3.5 Three Dimensional FE Analysis

The development of the three-dimensional vector finite element code proved to be highly problematic. The formulation of the elemental matrices is made more complex and there are four rather than three elemental matrices to consider. This arises from having to model the full vector wave equation rather than simplifying it into two scalar components. Also, the edge based interpolation functions are more difficult to formulate than their scalar counterparts, particularly for higher interpolation orders.

Enforcing continuity of scalar values at the nodal points forms the basis of the two-dimensional scalar finite element method. The analogous requirement in the three-dimensional vector finite element method is to enforce tangential continuity across an elements edge. In order to implement this correctly it is necessary to consider the orientation of adjoining edges and also adjoining faces when assembling the global matrices. These additional constraints coupled with the inherent difficulty of visualising a three-dimensional object in a two-dimensional format made testing and debugging the code an extremely difficult and time-consuming procedure. Section 3.6 presents a detailed discussion of the progress that has been made towards a working version of a three-dimensional vector finite element code.

The primary purpose of this research is to provide accurate and efficient finite element modelling software. This was a novel approach to the task of modelling photonic crystals, which at the time the research commenced, had not been well investigated. However, the widespread interest in photonic band gap devices has led to a number of companies releasing commercial vector finite element codes with a focus on photonic device modelling since the inception of this work. Rather than view this in a negative light it confirms that our initial motivation to begin the research was well founded and particularly valid.

The availability of such 'off-the-shelf' packages led to the move in focus from the development of the three-dimensional vector finite element code to photonic crystal design optimisation. This allowed the exploration of a new area of research whilst at the same time exploiting the highly optimised two-dimensional code we had already developed. It is hoped that the progress made so far can be used as the basis for further academic research.

3.6 Free-space Propagation at the Gamma Point

The solution to the vector wave equation (1.7) can be solved analytically for the case of propagation through free-space (see Appendix D:). This analytical solution is further simplified if one considers modes of propagation at the gamma point only, where the wave-vector, **k**, equals zero. The mode frequencies are proportional the square root of λ as shown in equation (3.2).

$$\lambda = \left(\frac{\omega}{c}\right)^2 = (\mathbf{G})^2 . \tag{3.2}$$

G represents the set of vectors emanating from the gamma point outwards to the reciprocal lattice points. Figure 3-16 is a graphical representation of this set of vectors travelling from the gamma point, highlighted by the blue dot, to the other reciprocal lattice points, highlighted in red. This set is stated mathematically in equation (3.3); m and n are integers and $\mathbf{b}_1$ and $\mathbf{b}_2$ are the reciprocal lattice vectors. This is for the two-dimensional case; the three-dimensional case would require an additional integral multiple of the third reciprocal lattice vector.

$$\mathbf{G} = m\mathbf{b}_1 + n\mathbf{b}_2 . \tag{3.3}$$

The value of λ is equal to the square of the magnitude of the corresponding vector **G**. Inspection of Figure 3-16 reveals that the vectors, **G**, can be grouped into those of equal magnitude.

Clearly these are going to produce equal values of λ.

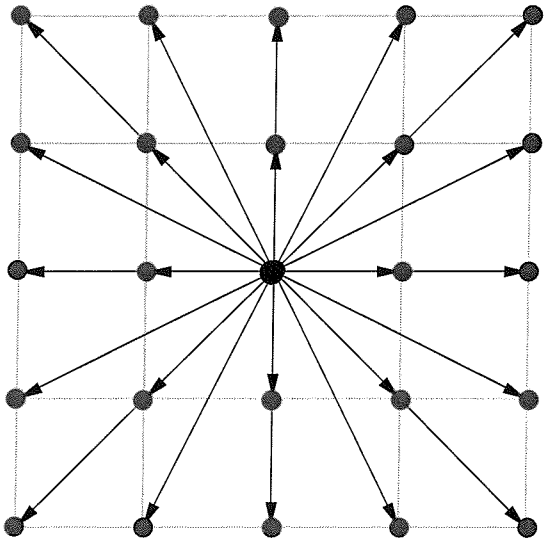

*Figure 3-16 The first 20 **G**-vectors in reciprocal lattice space corresponding to a square unit-cell representation of free-space.*

Table 2-1 gives the values of $\mathbf{G}^2$ and the number of times that they occur, n. Plotting these values in order of ascending magnitude would give a series of discrete steps of length n. The values of λ correspond to the eigenvalues computed by the finite element code. Therefore, plotting the eigenvalues computed for a mesh representation of free-space at the gamma-point in ascending order should give us approximately the same pattern of discrete steps.

$(\mathbf{G})^2$	n
0	1
1	4
2	4
4	4
5	8
8	4
9	4

Table 3-1 The values of λ (reciprocal lattice vector magnitude squared) and the number of times, n, that value occurs.

This data is shown in Figure 3-17. The lowest 30 eigenvalues were computed for a 200 element square unit–cell mesh with the permittivity of all the elements, ε = 1 corresponding to that of free-space. The agreement between the analytical data presented in Table 3-1 and the plot is

excellent with distinct discrete steps in λ with the number of times that they occur being as expected.

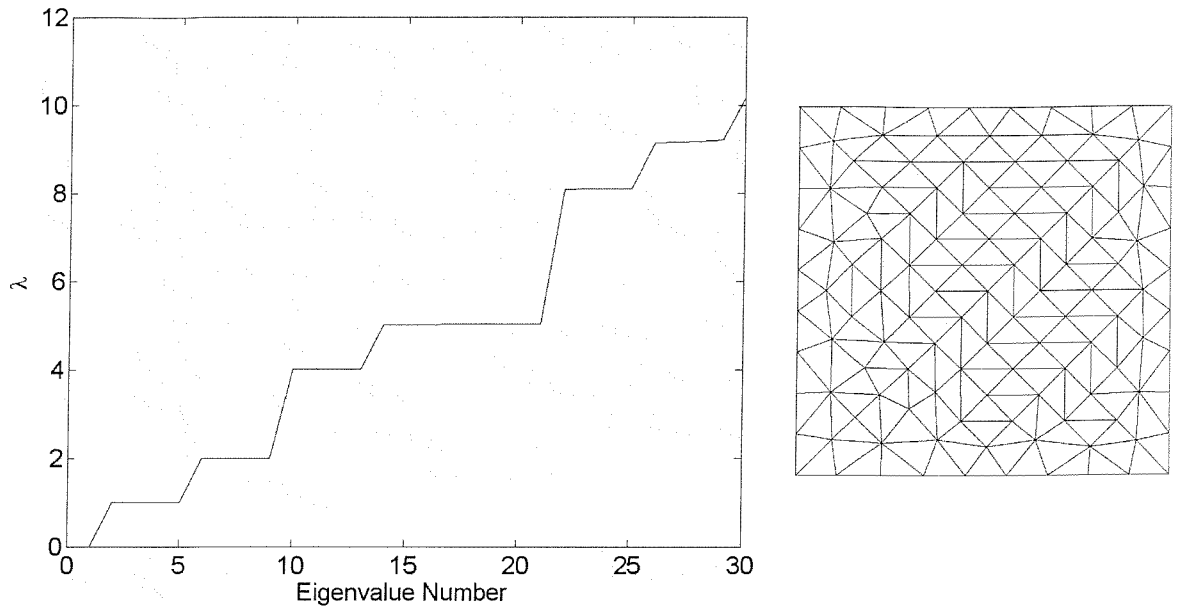

*Figure 3-17 A plot of the lowest 30 eigenvalues (a) computed for free-space at the gamma point (**k** = [0 0]) and the corresponding mesh representation of freespace (b).*

An analogous approach can be employed for initial testing of the three-dimensional code. The set of **G** reciprocal lattice vectors can be constructed according to equation (3.4)

$$\mathbf{G} = m\mathbf{b}_1 + n\mathbf{b}_2 + p\mathbf{b}_3 \tag{3.4}$$

These can be visualised by constructing the 3D reciprocal lattice space, as shown in Figure 3-18, figure (a) highlights the first 6 reciprocal lattice vectors of the shortest magnitude; figure (b) highlights the next group of 12 reciprocal lattice vectors of the same magnitude. The next group of eight reciprocal lattice vectors of equal magnitude extend to the eight corners of the reciprocal lattice space shown. Therefore, the lowest 125 eigenvalues are grouped as shown in Table 3-2.

$(\mathbf{G})^2$	n
0	1
1	6
2	12
3	8
4	6
5	24
6	24
8	12
9	24
12	8

Table 3-2 The values of λ (reciprocal lattice vector magnitude squared) and the number of times, n, that value occurs.

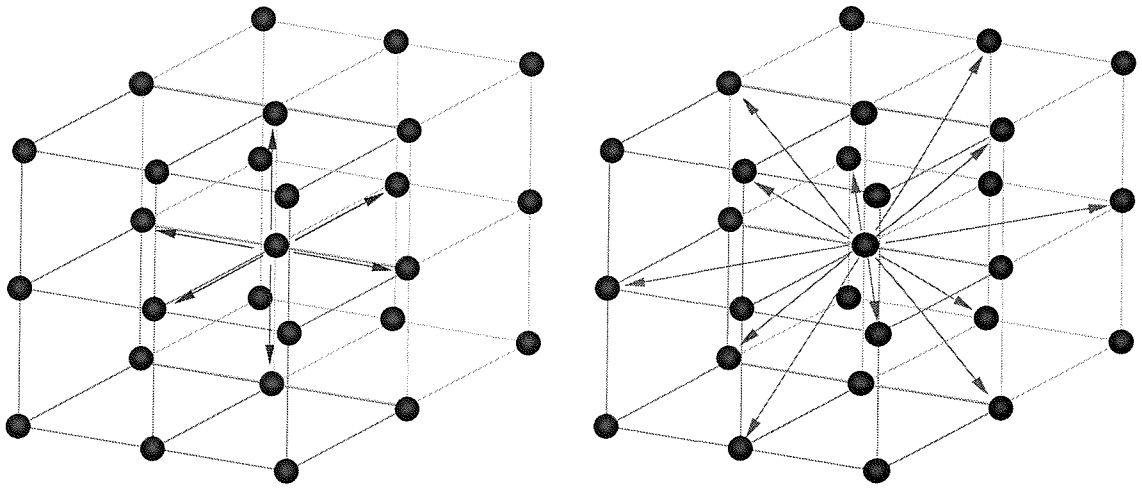

Figure 3-18 Reciprocal lattice space for a cubic unit cell. (a) represents the first 6 reciprocal lattice vectors of equal magnitude (b) represents the next 12 reciprocal lattice vectors of equal magnitude.

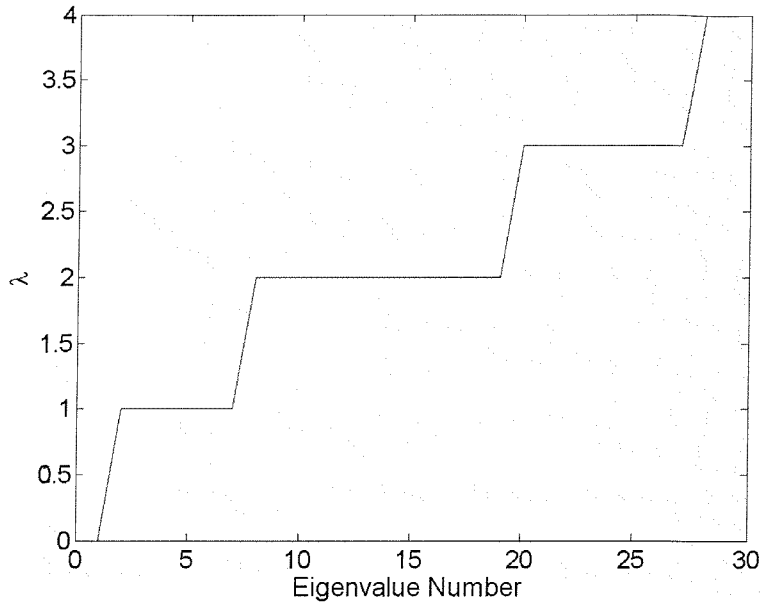

Figure 3-19 Plot of the analytical solution at the gamma-point for free-space in three-dimensions.

Three-dimensional mesh representations of free-space were generated using a number of public domain meshing algorithms. These consisted of cubic unit-cells composed of tetrahedral elements. These meshes were used as input to a beta version of the vector finite element code. The eigenvalues for three such meshes of increasing granularity are plotted in Figure 3-20, Figure 3-21 and Figure 3-22. Although the results do deviate from the exact analytic solution (see Figure 3-19) it is clear that as the granularity of the mesh increases the numerical solution is converging towards the correct solution.

We were unable to produce such accurate results for wave vectors other than the gamma point. This was due to errors still present in the formulation of the elemental matrices.

$$\begin{aligned} &\mathbf{A}(\mathbf{k})x = \lambda \mathbf{B}(x) \\ &\mathbf{A}(\mathbf{k}) = \mathbf{S} + i\mathbf{k}\cdot\mathbf{P} + k^2\mathbf{T} + \mathbf{k}^T\mathbf{J}\,\mathbf{k} \\ &\mathbf{B} = \mathbf{T} \end{aligned} \tag{3.5}$$

The fact that the correct results can be obtained at the gamma point indicates that the Dirichlet, **S**, and metric, **T**, matrices are being computed correctly therefore suggesting that the remaining bugs lie within the formulation of the **P** and **J** matrices.

To summarise, we have developed a vector finite element code capable of understanding various 3D input formats produced by popular public domain meshing algorithms, the necessary

periodic boundary conditions have been implemented and the correctness of the **S** and **T** matrices has been verified. Work remains to be done to correctly compute the **P** and **J** matrices.

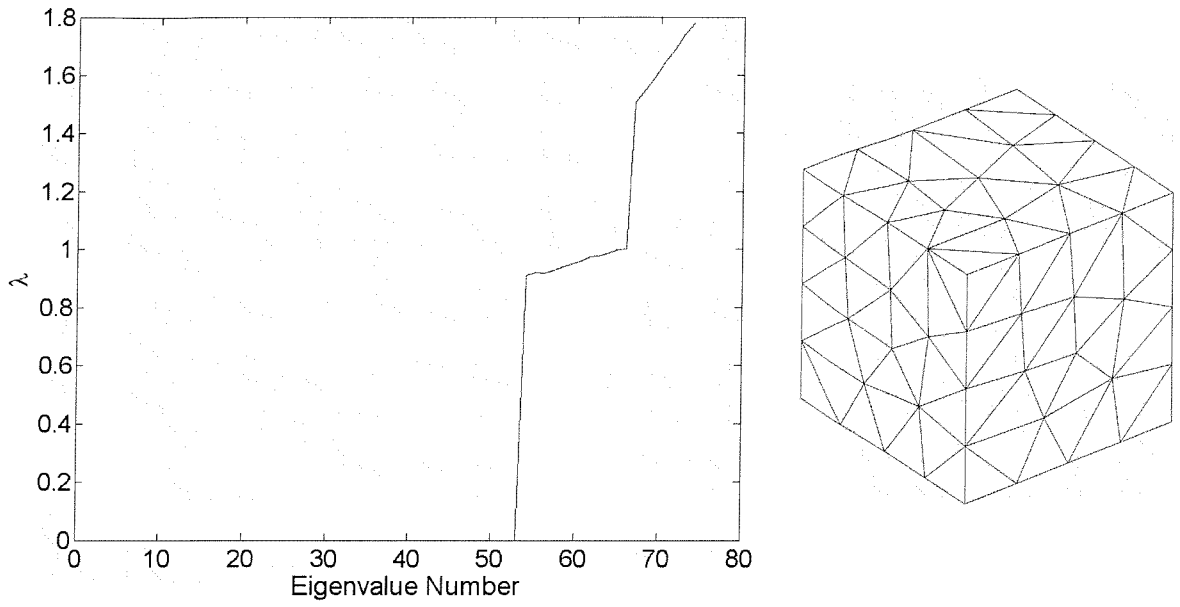

(a) (b)

Figure 3-20 A plot of the lowest 74 eigenvalues, (a), for a three-dimensional mesh representation of free-space consisting of 106 vertices and 310 tetrahedral elements, (b).

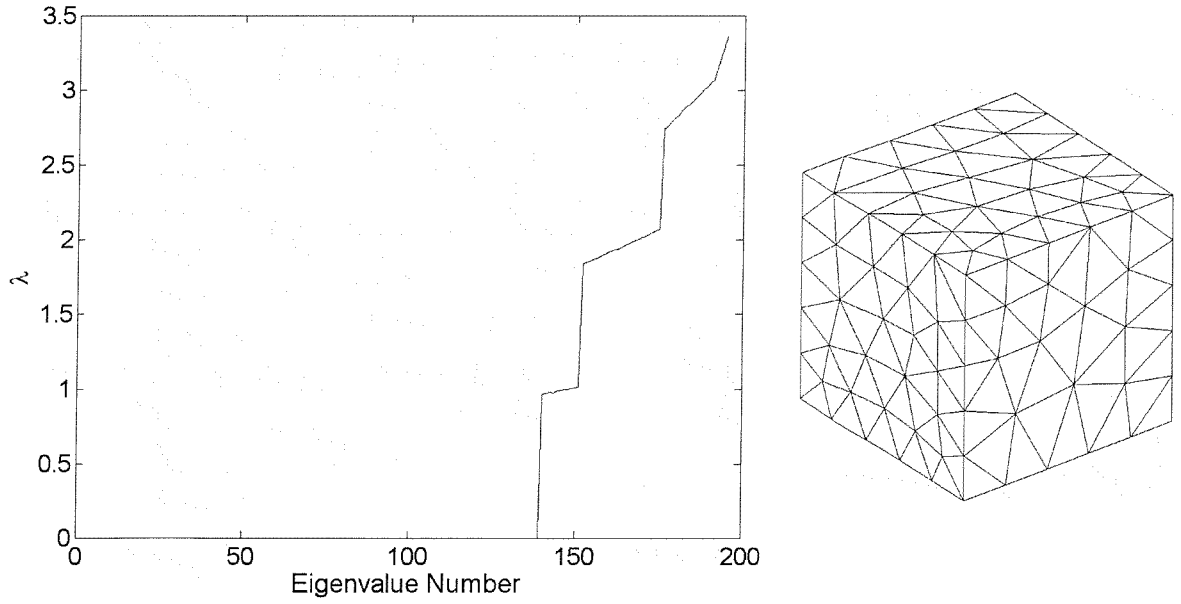

(a) (b)

Figure 3-21 A plot of the lowest 195 eigenvalues, (a), for a three-dimensional mesh representation of free-space consisting of 225 vertices and 822 tetrahedral elements, (b).

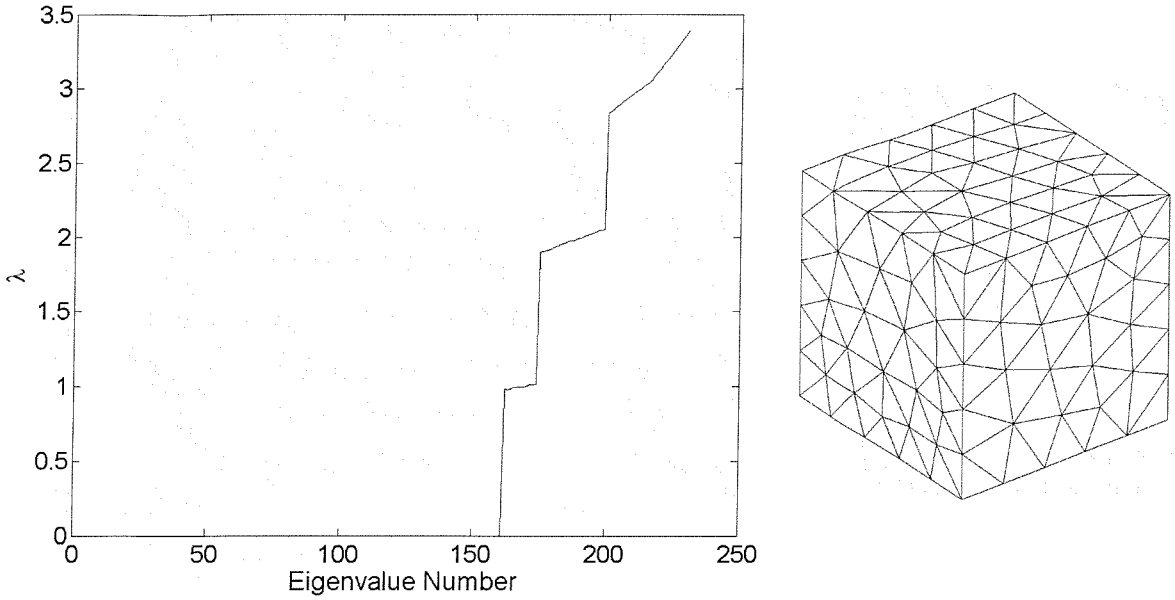

(a) (b)

Figure 3-22 A plot of the lowest 230 eigenvalues, (a), for a three-dimensional mesh representation of free-space consisting of 260 vertices and 958 tetrahedral elements, (b).

The problem of spurious modes is clearly apparent from the 3D eigenvalue plots. The analytic solution produces one zero eigenvalue corresponding to the reciprocal lattice vector, $\mathbf{G} = (0, 0, 0)$. Our numerical result produces far more zero eigenvalues, with the exact value being equal to the number of internal vertices (those vertices not lying on the unit-cell boundary) in the mesh. This is clearly a problem in terms of efficiency as to compute the lowest n eigenvalues of interest we actually have to compute $n + w$ eigenvalues, where w represents the number of internal vertices. For example, Figure 3-22 shows that for a 958-element mesh there are 162 internal vertices, therefore to compute 60 eigenvalues that correspond to real solutions we have to compute the lowest 222 eigenvalues with 162 of those corresponding to non-physical solutions. An alternative eigenvalue solver has been written to solve this problem, based on the Implicitly Restarted Lanczos method, (Golub and Van Loan 1996), (Calvetti, Reichel et al. 1994), it can be used to filter out the zero eigenvalues as they converge by removing them from the sub-space.

3.7 Fabrication Constraints

It is vital to consider real world constraints when investigating numerical models. In the case of modelling photonic band gap devices one must consider the errors involved in the fabrication

process. We may have an accurate model but variations in the fabrication process may result in actual devices based on our theoretical results having significantly different optical characteristics.

Typically, we are interested in photonic devices that exhibit a band gap in the visible light region of the electromagnetic spectrum. For diffraction to occur the feature size of a photonic crystal must be comparable to that of the wavelength to which it is intended to operate, hence we need to have a feature size in the order of 10^{-6}m. Triangular lattice arrangements of air rods in a substrate material have been chemically etched with a pitch length (distance between rod centres) of 310nm (Charlton and Parker 1998), (Campbell, Sharp et al. 2000). The absolute error for this distance is ±15nm. The absolute error for a rod radius of 100nm is ±5nm. This corresponds to a relative error of 5% for both the rod position and the rod radius.

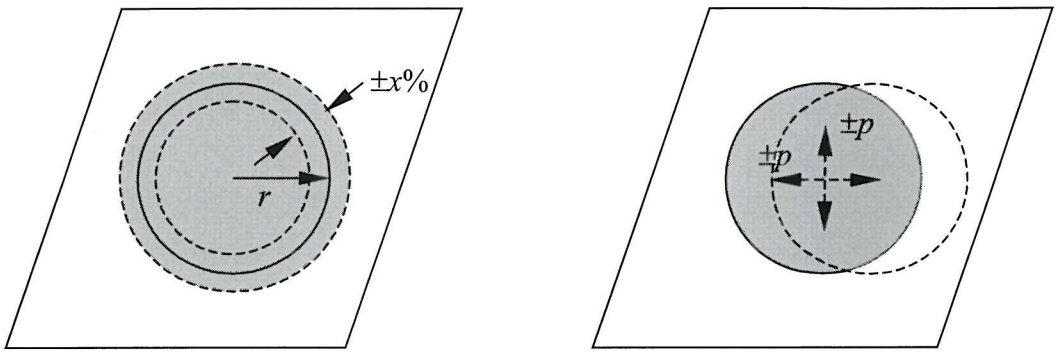

Figure 3-23 The error associated with(a) the rod radius and (b) the rod position.

It is important to understand the implication of these tolerances on the resulting band structure of the photonic band gap device. In order to investigate this we designed an experiment allowing us to observe the effect of random fluctuations in both rod position and radius. A nine rod rhombic unit-cell was used as the basis of the experiment as can be seen in Figure 3-24. 250 meshes were generated in which the rod radii could vary by up to ±5%, representing the current fabrication tolerance. This was repeated in decreasing integral increments down to 1% to illustrate how the situation would change if fabrication tolerances were to improve. In every case, the relative error in the rod position was fixed at 4.8%. Each of the 1250 meshes were analysed using the finite element code. The material parameters used corresponded to air-rods in GaAs.

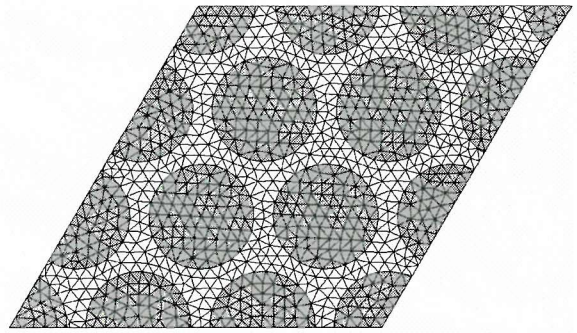

Figure 3-24 A rhombic unit-cell containing nine rods. The radius of these rods vary randomly within a prescribed percentage error constraint.

The resulting eigenvalues were post-processed to produce Figure 3-25. This presents the mean upper and lower normalised frequency values for a given % error in the rod radius. The error bars represent ± one standard deviation away from the mean.

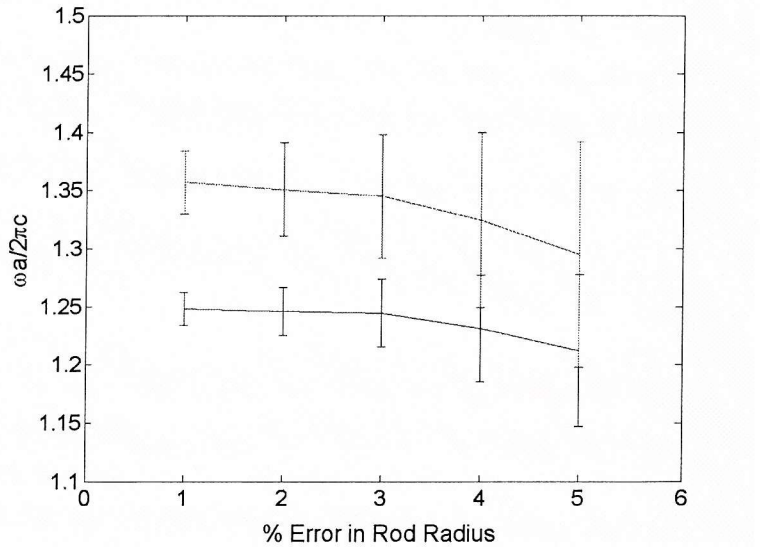

Figure 3-25 A plot of the upper and lower bounds of the band gap against the relative error in the rod radius. The error bars represent one standard deviation either side of the mean.

The large number of randomly generated meshes resulted in the lower and upper bounds of the frequency ranges having a normal distribution. This allowed us to compute the probability of our nine rod triangular lattice crystal would exhibit a band gap within a given fabrication tolerance. Figure 3-26 shows the distribution functions of the upper and lower frequency values for a 1% relative error in the rod radius (a) and a 5% relative error (b). The probability of a photonic crystal not exhibiting a band gap is equal to the area in which the upper and lower frequency distribution functions overlap. For a 1% rod radius tolerance the overlap is small, hence the probability of fabricating a photonic crystal with a robust band gap is good. Increasing the rod radius tolerance to 5%, that which we expect from current fabrication techniques, has a

dramatic effect. The overlap of the lower and upper frequency limits is far greater resulting in a probability of a device exhibiting a band gap of only 0.42. The probabilities of fabricating a device that exhibits a photonic band gap are given in Table 3-3.

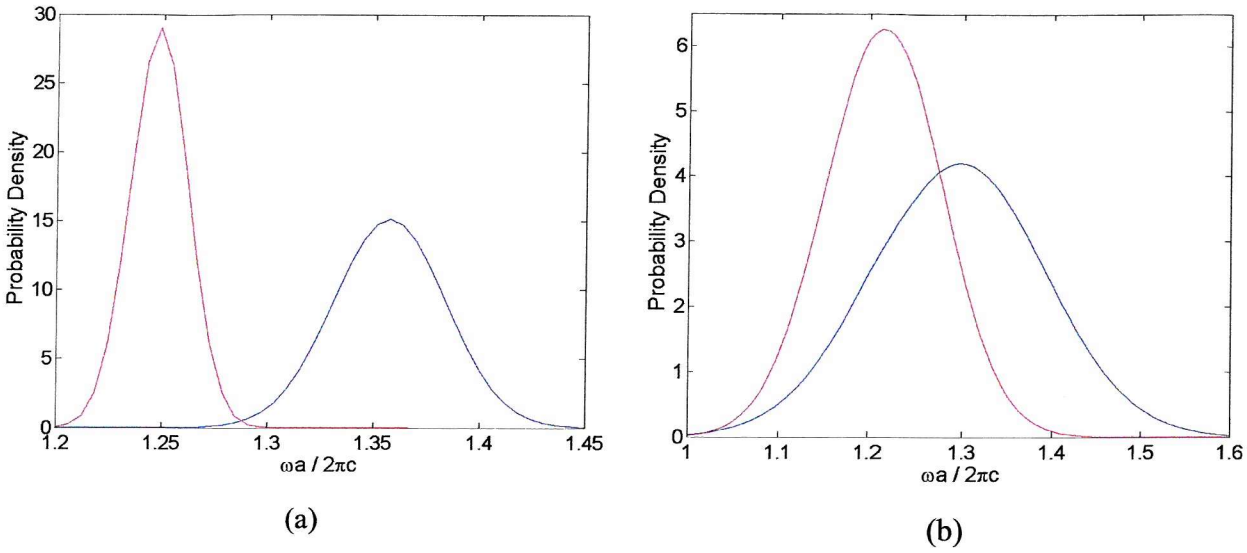

(a) (b)

Figure 3-26 The normal distributions of the positions of the lower (red) and upper (blue) bounds of the photonic band gap frequency range for a relative error in the rod radius of (a) 1 % and (b) 5 %.

Relative Error (%)	Probability of a Band Gap
1	0.99
2	0.92
3	0.81
4	0.59
5	0.42

Table 3-3 The probability of a triangular lattice photonic crystal exhibiting a photonic band gap for a given relative error in the rod radius.

The equivalent experiment was performed varying the error in the rod position while keeping the error in the rod radius constant. 250 meshes were generated for relative errors of 1, 2, 3 and 4%. This data was combined with that generated previously in Table 3-3 where the rod position error was 4.8% corresponding to the current relative error in the lithography process at the University of Southampton. The results from these analyses are presented in Figure 3-27. The probability of the photonic crystal (see Figure 3-24) exhibiting a photonic band gap is plotted against the relative error in the rod position. The various lines correspond to variations in the rod radius error.

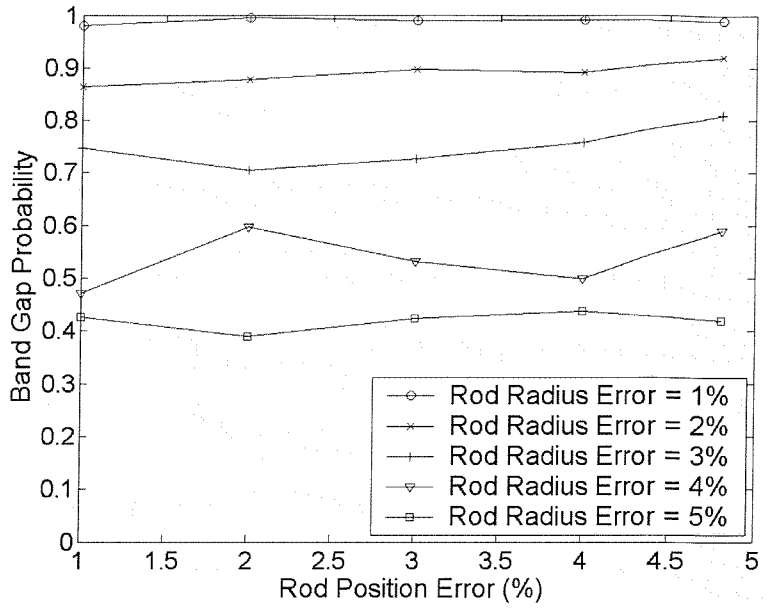

Figure 3-27 Probability of the photonic crystal exhibiting a band gap for various relative errors in the rod position. Each line corresponds to a different relative error in the rod radius as explained in the legend.

From Figure 3-27 it can be seen that the error in position of the rods makes little difference to the probability of there being a band gap. The probability values vary by relatively small amounts as the error in the rod position increases, there is also no obvious trend in the values as the positional error increases, the values simply oscillate around the mean. This is in stark contrast to the effect of error in the rod radius. Thus we can conclude the most important factor in the fabrication of photonic crystals is the filling fraction. It is vital that this value is controlled within as low a relative error as possible if the numerically modelled and fabricated counterpart are to exhibit the same photonic band gap.

Analysis of the triangular lattice structure with the finite element code showed the optimum filling fraction to be 83%. This corresponds to a radius to pitch length (r/a) of 0.48. Multiplying by a pitch length of 310nm gives us an actual rod radius of 148nm. Considering a worst-case scenario, this rod radius could be 5% larger at 155.4nm. This gives a rod diameter that is greater than the pitch length; hence the substrate material would become disconnected and is likely to collapse rendering the device useless.

To summarise, we are left with a situation in which the accuracy of the numerical model exceeds that of the fabrication technique. Investigation into the effects of errors in the fabrication process, particularly with regard to rod-radius and therefore the filling fraction, has shown that a large variation from the desired behaviour is probable with current fabrication techniques. It is vital therefore, that current techniques are refined or new techniques developed.

4 Performance

4.1 Accuracy and Convergence

Since the FEM computes an approximation to the true solution for a given spectral problem, it is important to estimate the accuracy of a given solution and the rate at which the approximate solution converges to the true solution (Villeneuve and Piche 1994).

The spectrum for free space can be computed using the FEM and compared with the analytical solution as explained in chapter 3.1. This calculation can be repeated for varying mesh granularities to ascertain the rate of convergence.

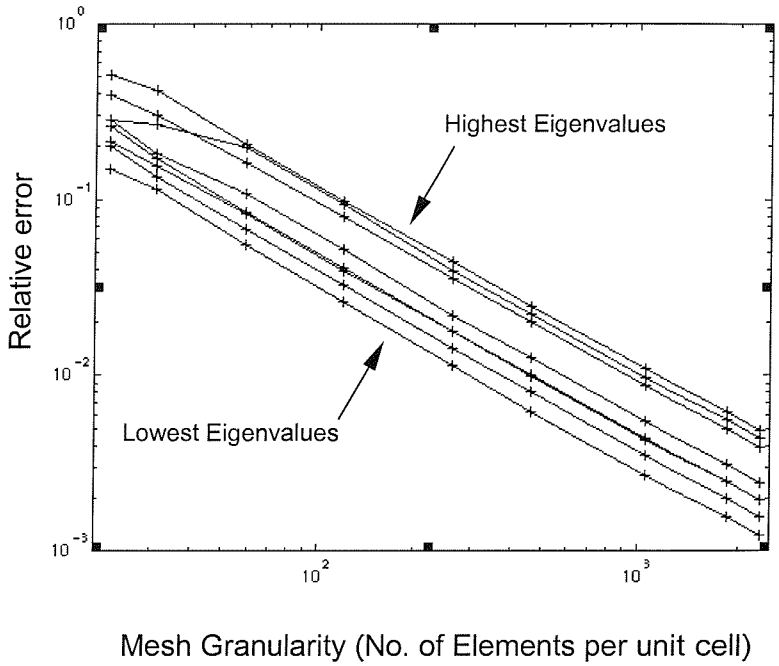

Figure 4-1 Convergence of the FEM for free-space. The maximum relative errors for the lowest 9 eigenvalues are plotted against mesh granularity.

Figure 4-1 demonstrates that FEM eigenvalues converge to the correct answer as the mesh granularity is decreased. A series of 2-dimensional FEM analyses of propagation of electromagnetic waves in free space were performed, using increasingly fine meshes; in each case, the lowest nine eigenvalues were compared to corresponding analytical solutions of the system. The maximum relative error in each of the eigenvalues is plotted against the number of nodes in the mesh. The maximum relative error is computed using the following formula:

$$\text{relative error} = \left| \frac{\text{approx eigenvalue} - \text{true eigenvalue}}{\text{true eigenvalue}} \right|. \qquad (4.1)$$

The maximum relative error refers to the eigenvalue for a given mesh (for each mesh, $n \times k$ eigenvalues are computed where n is the number of eigenvalues computed at each k-vector and k is the number of k-vectors sampled) that has the greatest relative error. The diagram also shows that the lower eigenvalues tend to be significantly more accurate than higher ones.

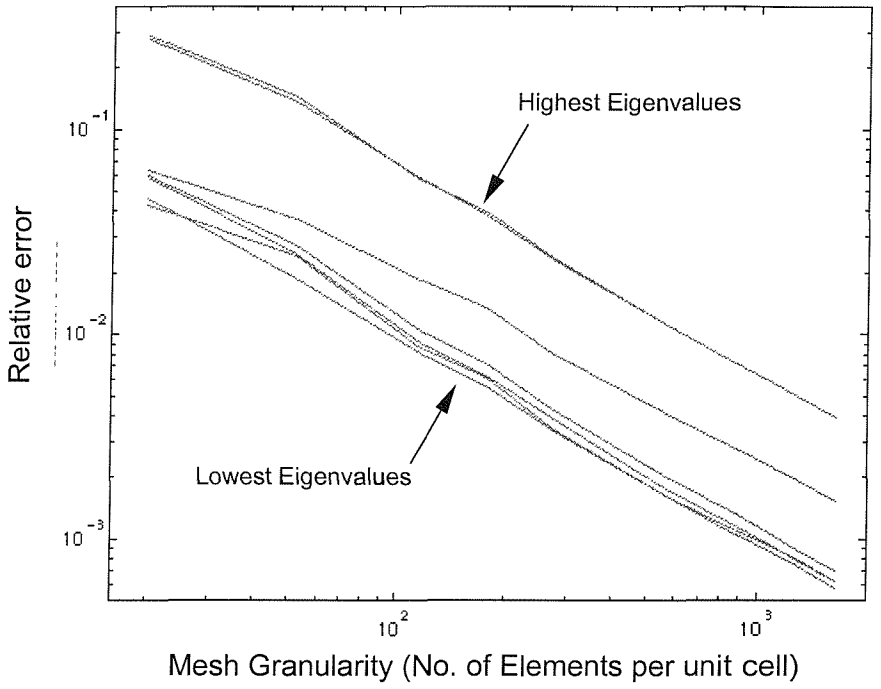

Figure 4-2 Convergence of the FEM for a triangular Lattice. The maximum relative errors for the lowest nine eigenvalues are plotted against mesh granularity.

The same procedure was performed with a triangular lattice. As the analytical solution is not available for this system, the exact eigenvalues were estimated by extrapolation of the modelled data and plotted in Figure 4-2.

Both figures have a gradient of approximately minus one; as both axes are logarithmic, doubling the mesh density for a unit cell halves the relative error.

4.2 Optimising 2D Algorithm Performance

The first step is to check that the cost in terms of memory and computation for various

interpolation orders does scale linearly as the theory of the FEM suggests. Secondly, the relationship between the quality of the solution, the mesh size and the interpolation order needs to be investigated. To do this, a number of triangular lattice meshes were created with the number of elements ranging from 25 to 4000 elements. The filling fraction was kept constant at 50%. These meshes were run through the FEM code for first to fourth order interpolation. The lowest 10 eigenvalues were computed for 50 k steps taken from the Brillouin zone. The computation time and the resulting eigenvalues were recorded. The relative error was computed via comparison to a pseudo-exact solution (4000 element mesh with fourth order interpolation). Plotting computation time against mesh size (Figure 4-3) showed a linear relationship for all four interpolation orders confirming the O(n) scaling of computation cost.

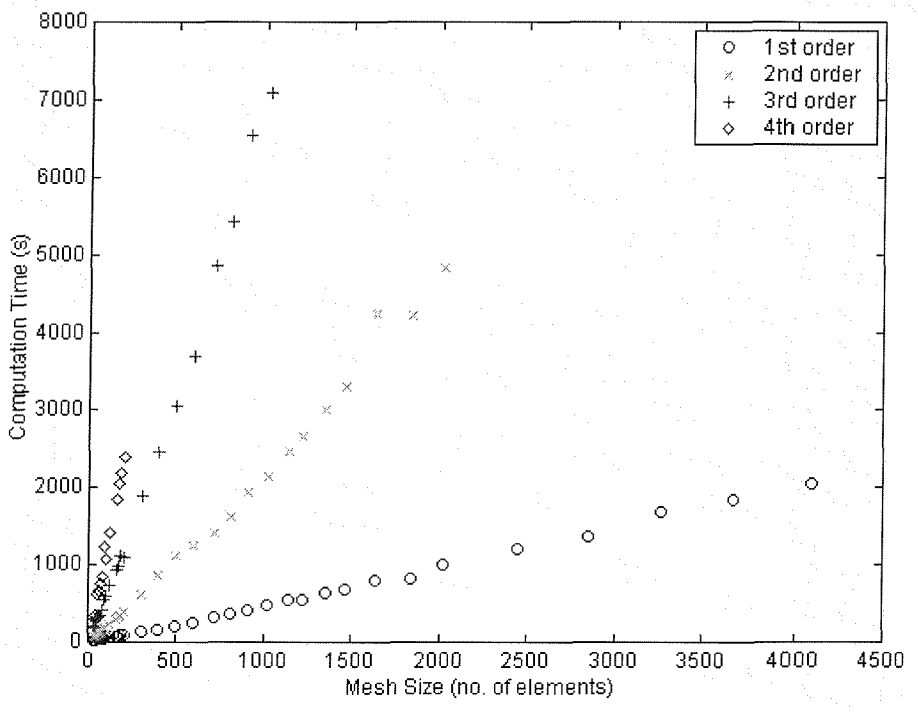

Figure 4-3 Comparison of computation time with mesh size (no. of elements) for interpolation orders one to four.

Analysis of the relationship between mesh size (number of elements) and the number of non zero values in the resulting eigensystem matrices (Figure 4-4) also revealed an exactly linear relation for all interpolation orders. This confirms that the memory cost of the algorithm also scales with O(n) as the memory requirement of the algorithm is that of the sparse matrices stored.

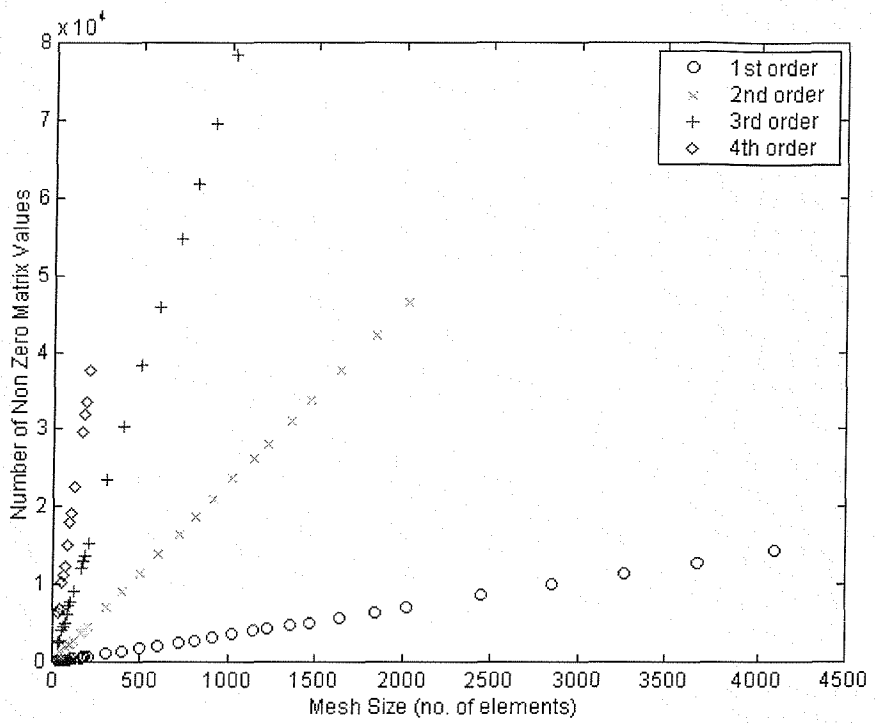

Figure 4-4 Comparison of no. of non zero matrix values with mesh size (no. of elements) for interpolation orders one to four.

Having confirmed that memory and computation scale with O(n), the performance of the algorithm must be investigated, i.e. how can we achieve the best possible solution with the minimal effort in terms of memory and computation.

Plotting relative error against the number of non-zero matrix values exposes the interpolation order that will yield the most accurate solution for a given memory cost. This is true as the number of non-zero matrix elements is directly proportional to the memory cost of the algorithm. The interpolation order that is closest to the bottom left corner of the figure (representing the ideal of minimum memory for lowest error) is the one that gives the optimal solution quality for the minimum memory cost. Figure 4-5 shows that there is little to choose between interpolation orders two and three with fourth order appearing marginally worse. It is clear that first order does not perform as well.

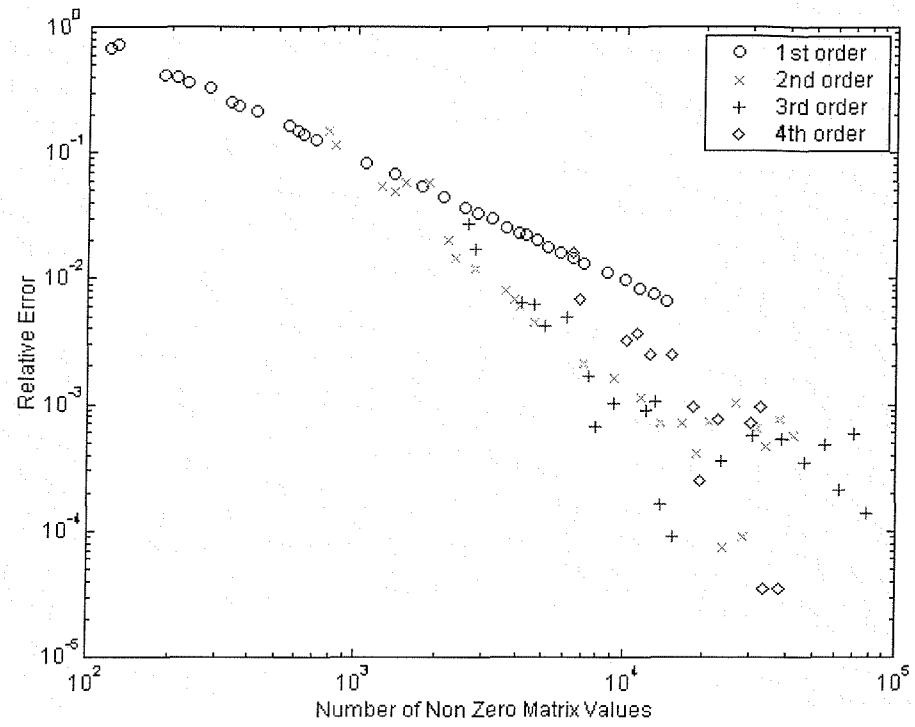

Figure 4-5 Comparison of relative error with the no. of non zero matrix values for interpolation orders one to four.

A plot of relative error against computation time (Figure 4-6) reveals similar results, optimal but indistinguishable performance for second and third orders, marginally worse for fourth order and significantly worse for first order.

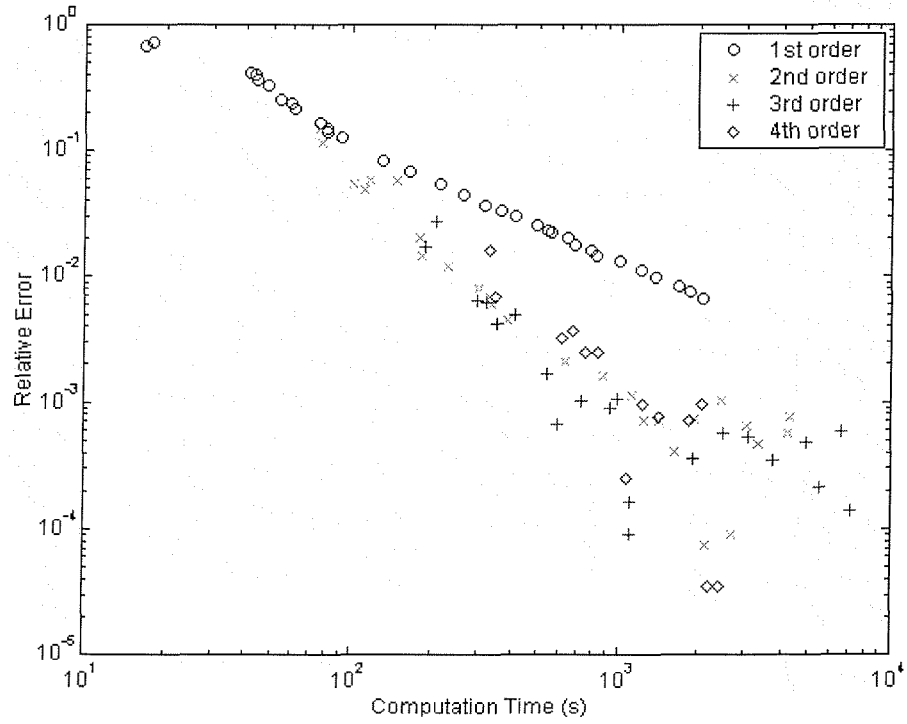

Figure 4-6 Comparison of relative error with computation time for interpolation orders one to four.

Bearing this in mind it seems that using second or third order interpolation gives optimal overall performance. However, it is important to bear in mind that for a given number of non-zero matrix values the mesh size will be larger for the lower interpolation orders as there are less interpolatory nodes. This leads to the fact that the actual dielectric structural representation will be more accurate for lower interpolation orders for a given memory cost. This issue could make second order interpolation a better choice for very complex crystal structures.

4.3 Object-Oriented Software Approach

This section outlines the software engineering side of the project.

The finite element analysis software has been developed using C++ (Stroustroup 1997), Python (Lutz 1996) and Matlab (The MathWorks 1999). Python and Matlab were used primarily as rapid prototyping tools. The fact that they are scripting languages makes them particularly suitable for this purpose. The code was then converted to C++ for the performance gain of a compiled, rather than interpreted language.

Python and C++ combine well as they are both strongly object-oriented languages hence converting between the two is relatively simple. Matlab excels in matrix based computation and data visualisation. This has been useful for verification of portions of the code, e.g. the eigenvalue solver, and for visualisation of the band diagrams, electric and magnetic fields.

The object oriented programming paradigm encapsulates data and methods together into objects. These objects can communicate via message passing. A message can invoke a method presented in an objects interface. This arrangement allows objects to hide their functionality and merely present services to other objects via well-defined interfaces.

This arrangement allows complex software systems to be built up in a modular fashion from a number of objects, each object offering a range of related services. This approach increases productivity and gives scope for greater reusability of code. The FEMLIB software class structure is as follows:

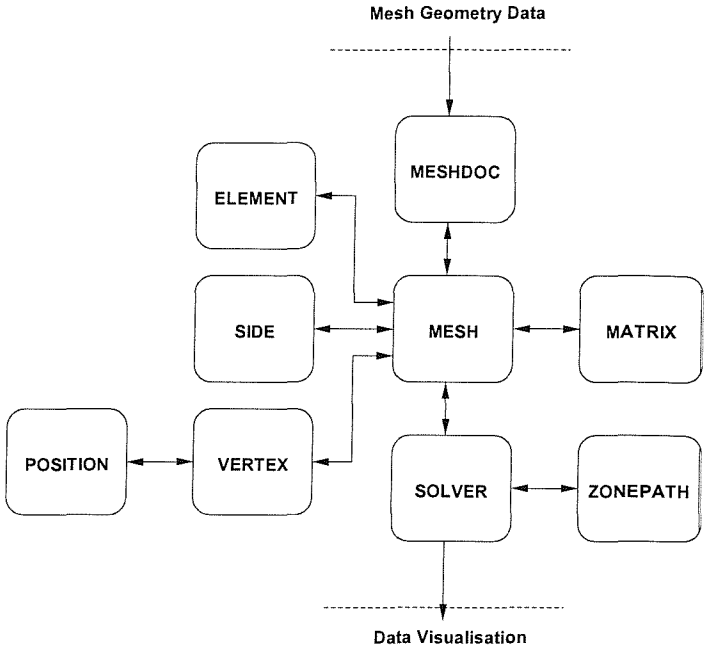

Figure 4-7 FEM class structure.

4.4 Classes and Interfaces

The main classes and their structure are depicted in Figure 4-7. These classes along with their constituent methods and data members are described in Appendix G:. The mesh geometry data is produced by Easymesh and output into a number of separate files. These files are processed by FEMLIB to produce an object-oriented representation of the mesh. In the 2D case, this involves producing an `element`, `side` and `vertex` object corresponding to each one in the mesh. This idea can be extended to higher dimensions with the introduction of higher order simplexes. The objects must contain the relevant information describing the structure of the mesh. For example, a `vertex` object must contain its position in space, a `side` object must know the vertices at each of its ends and an `element` must know from which sides it is constructed.

This connectivity between objects is achieved by implementing vectors of pointers to objects e.g. a `side` has a vector of pointers to `vertex` objects and an `element` has a vector of pointers to `side` objects.

A `mesh` object uses the same principle. It has a vector of pointers to every `element`, `side` and `vertex` in that `mesh`. This is illustrated in Figure 4-8.

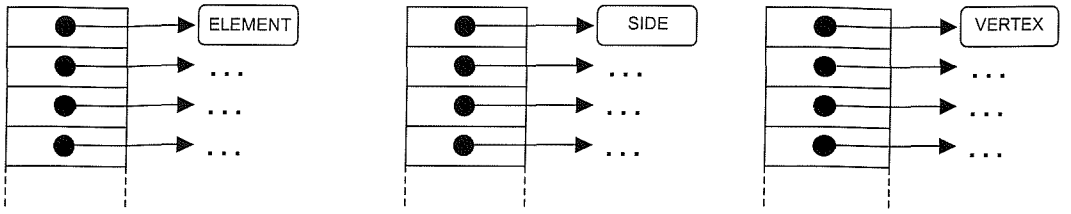

Figure 4-8 Pointer based mesh storage structure.

This approach to the mesh structure facilitates the enforcement of the periodic boundary conditions. Figure 4-9 illustrates that corresponding vertices on either side of the bounding parallelogram are essentially the same vertex under periodic boundary conditions, e.g. x and y are the same vertex. This is represented by having the two vector elements that represent x and y point to the same vertex object. In the special case of the corners of the bounding parallelogram, four vector elements, a, b, c and d all point to the same vertex object. The same technique is used for sides that lie on the boundary.

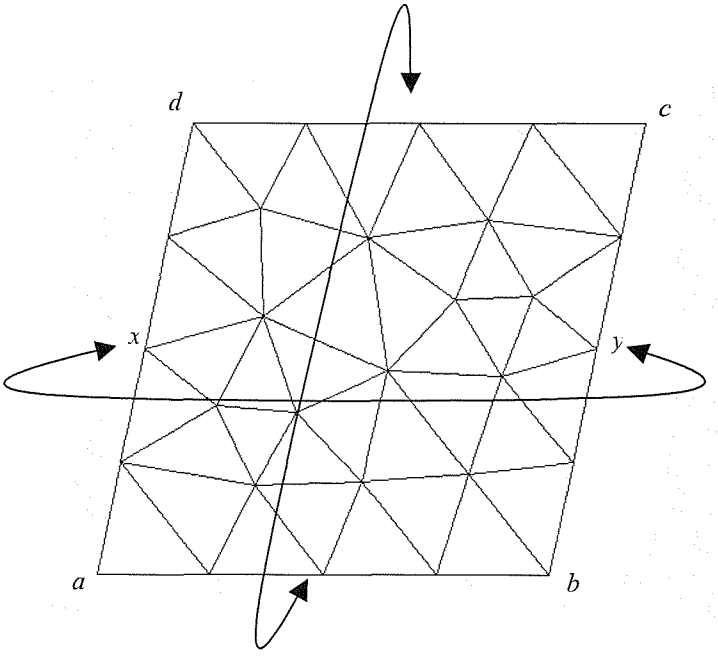

Figure 4-9 Periodic boundary conditions.

The `element` class contains methods to calculate the elementary matrices. These are stored as `matrix` objects. These `matrix` objects are then assembled into global matrices by the `mesh` class. These global `matrix` objects are then passed to the eigenvalue solver.

A `matrix` object stores the data elements and provides several methods. These include element extraction, matrix-scalar operations, matrix-vector operations, matrix-matrix operations, similarity transforms, Cholesky decomposition and reduction to tri-diagonal form.

The `zonepath` class defines the path of the quasimomentum vector, k, around the Brillouin zone. Its methods allow specification of the number of legs the path has, the step size for each leg and the Cartesian coordinate of each corner of the path.

4.5 Computing Resources

This section details the computational resources that were utilised to run the software that we developed.

The increase in performance achieved by desktop PCs over the last few years has been accompanied by a growth in the use of such computers in numerically intensive scientific applications. Various 'Beowulf' projects (Beowulf 2002) have used the convergence of mid-range proprietary workstations and desktop PC's to produce commodity super-computers. The basic idea is to connect together a number of headless PCs via a network whether it be simple Fast Ethernet or a more specialised interconnect and using the flexibility of the operating system create an environment wherein the individual workstations, appear to the user, to behave as one multi-CPU computer. Since all of the components in such a machine are off-the-shelf and mass-produced the cost benefits of such an approach are considerable.

Whilst the finite element code is efficient, it is still computationally intensive. This is especially true when modelling complex crystal geometries requiring many thousands of elements and high order interpolation functions. This coupled with the sheer number of photonic crystals that have been analysed necessitated the use of high performance computing facilities provided by the University of Southampton.

Initial computation was performed on the Linux Beowulf cluster, DGL. Iridis, a substantially larger Linux Beowulf cluster, superseded this in December 2001. The optimisation software was tied to the Windows operating system due to the third party meshing algorithm; hence computation was performed on a test-bed Windows cluster. The technical specifications of these computing facilities are as follows.

4.6 Iridis: The Beowulf Cluster

Iridis is a Linux Beowulf cluster maintained by the University of Southampton computing

services department (Iridis 2002). It has the following specification:

- 550 processors; consisting of 292 1000Mhz Intel Pentium III's; 80 1800Mhz Intel Pentium IV's and 32 1500Mhz Intel Pentium IV's
- 192Gb of memory
- 8.5Tb of local disk storage
- 2.8Tb on RAID5 disk array

It is capable of 484 billion floating-point calculations per second. Jobs are submitted via a master node running the EASY job scheduler (EASY 2002). This is a bespoke scheduler developed by the University of Southampton. It is specifically tuned to the target-users to provide fair resource allocation.

4.7 Iridis: The Windows Condor Cluster

A small number of the PC's bought for the Iridis project have been used to create a test-bed Windows cluster. It has the following specification:

- 16 Single Processor Intel Pentium IV's
- 8.2 GB of memory
- 600 GB of local disk storage

The cluster is grid-enabled using Condor (Condor 2002), This is a software system that creates a High-Throughput Computing (HTC) environment by harnessing the power of a cluster of workstations on a network. Although Condor can manage a dedicated cluster of workstations, a key appeal of Condor is its ability to utilise non-dedicated, pre-existing resources in a distributed ownership setting such as machines sitting on people's desks in offices and labs.

Condor provides a framework to harness idle compute cycles within a network of computers. The structure is that of a pool of resources (networked workstations) managed by a Central Manager workstation. The user submits jobs to the pool from his/her workstation. The Central Manager matches resource requests with resources available within the computing pool.

4.8 DGL: The Beowulf Cluster

DGL is a small Linux Beowulf cluster maintained by the High Performance Computing Group, Department of Electronics and Computer Science, University of Southampton. It has the

following specification:

- 8 Single Processor AMD Athlon 600 MHz
- 2 GB of memory
- 180 GB of local disk space

Jobs are submitted via a master node running the MAUI job scheduler (MAUI 2002). This is a well known and respected scheduling algorithm maintained and developed at Brigham Young University, Utah. Maui is an open source project and may therefore be freely downloaded, modified, and distributed. It is also supported by the Department of Energy, the Pacific Northwest National Laboratory, the Centre for High Performance Computing at the University of Utah, the National Centre for Supercomputing Applications and many others.

The availability of these high-performance computing resources has been vital to this research, particularly the design optimisation process where large numbers of crystal structures had to be analysed. Without the high throughput that these commodity clusters provide, much of the work would have been unfeasible due to the increase in the amount of time required. Also, the move towards grid-enabled computing, as demonstrated by the Windows cluster running Condor, allows the user to move away from the paradigm where one has to specify where and when the code should run. The grid-enabled paradigm allows the user to and work at a higher level of abstraction avoiding the low-level detail. Hence the user can concentrate on the code and subsequently the computed results, it is the computer system that decides where and when the code should run.

5 12-fold Symmetric Photonic Quasicrystals

It is desirable in some cases to maximise the band gap while minimising the contrast in dielectric constant (Villeneuve and Piche 1994). One way of achieving this is to experiment with novel crystal geometries. One such promising structure is the 12-fold symmetric quasicrystal (Zoorob, Charlton et al. 2000). This crystal structure shows great potential as a novel photonic band gap material exhibiting a band gap for relatively low filling fractions and dielectric contrasts. The band gaps are highly homogeneous with respect to the angle of incidence of the incoming light due to the crystals high degree of rotational symmetry. These crystals have been analysed using the finite element method developed specifically for modelling PBG structures. We present and discuss quasicrystal structures and their optical properties.

5.1 Quasicrystal Configurations

The quasicrystal structure proposed in (Zoorob, Charlton et al. 2000) is based on a dodecagon composed of an inner hexagon consisting of six equilateral triangles surrounded by a ring of squares and equilateral triangles. The two fundamental quasicrystal structures are the 'square-square' and 'triangle-triangle'. The descriptions highlight the way in which the dodecagons are joined to form the lattice. Examples of each are shown in Figure 5-1, with the unit cells outlined in bold. Anisotropies can also be introduced to the lattice by rotation of the dodecagons to produce 'square-triangle' arrangements, however, these structures require larger unit cells to reproduce the anisotropy when periodically tiled.

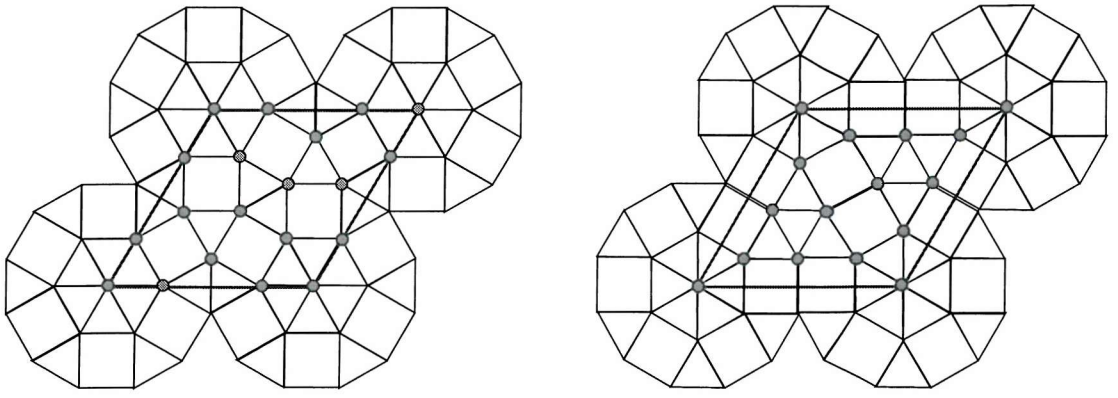

(a) (b)

Figure 5-1 12-fold symmetric quasicrystal configurations: (a) 'Triangle-Triangle' and (b) 'Square-Square'.

Figure 5-2 shows unstructured triangular mesh representations of the 'triangle-triangle' and 'square-square' configurations. The circular rods are centred on the vertices of the quasicrystal structure.

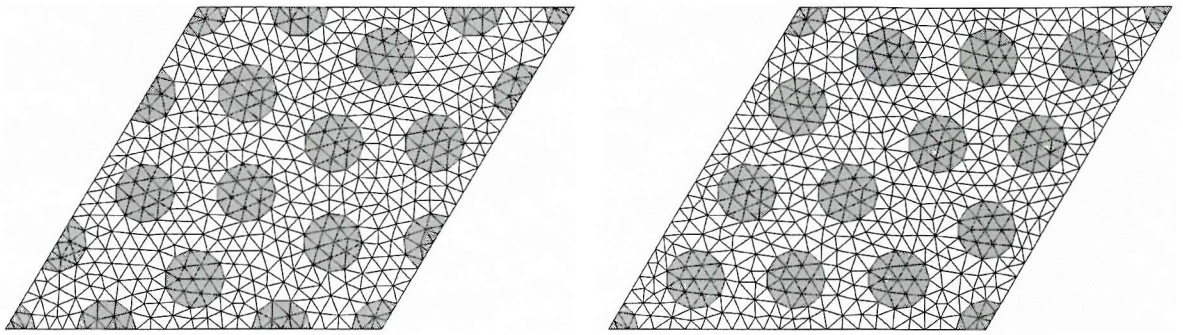

Figure 5-2 Unstructured triangular mesh representations of the rhombic unit-cells: (a) 'triangle-triangle' and (b) 'square-square' configurations.

Several meshes were produced, in both configurations, with rod to pitch length ratios (*r/a*) varying from 0.1 through to 0.5 in 0.01 increments. These meshes were used with the FE code with various material parameters including air-rods in gallium arsenide, silicon nitride and glass and vice versa, e.g. gallium arsenide rods in air. The set of **k**-vectors were sampled from a path describing the irreducible Brillouin zone, $K \rightarrow \Gamma \rightarrow X \rightarrow K$, as illustrated in Figure 5-3.

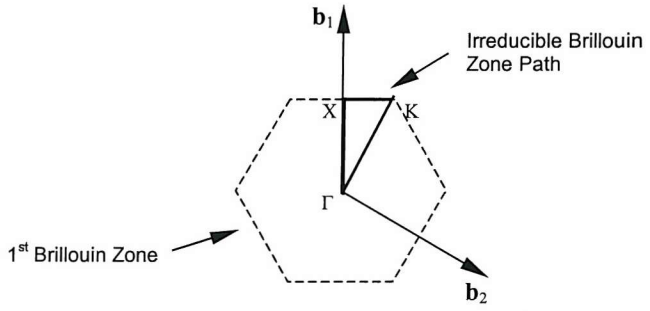

Figure 5-3 The irreducible Brillouin zone path, $K \rightarrow \Gamma \rightarrow X \rightarrow K$, used in the analysis of the quasicrystal photonic band-gap devices.

5.2 Results

Dispersion relations are presented in Figure 5-4 for both the 'triangle-triangle' and 'square-square' crystal configurations with a rod radius to pitch length ratio (*r/a)* of 0.5 for air rods in silicon nitride (SiN, $\varepsilon = 4.1$) and gallium arsenide (GaAs, $\varepsilon = 11.4$). A complete band gap is evident between 0.48 and $0.57\omega a/2\pi c$ for GaAs, whereas SiN only exhibits a small gap in the TM mode centred at $0.33\omega a/2\pi c$. In all cases, 'triangle-triangle' and 'square-square' configurations produced almost identical spectra. The mirror symmetry shown between

dispersion relations as one moves along K-Γ and Γ-X in reciprocal lattice space proves that a crystal rotation of 30° produces the same band structure. This supports the claim that quasicrystals are highly homogeneous with respect to the angle of incidence of incoming light.

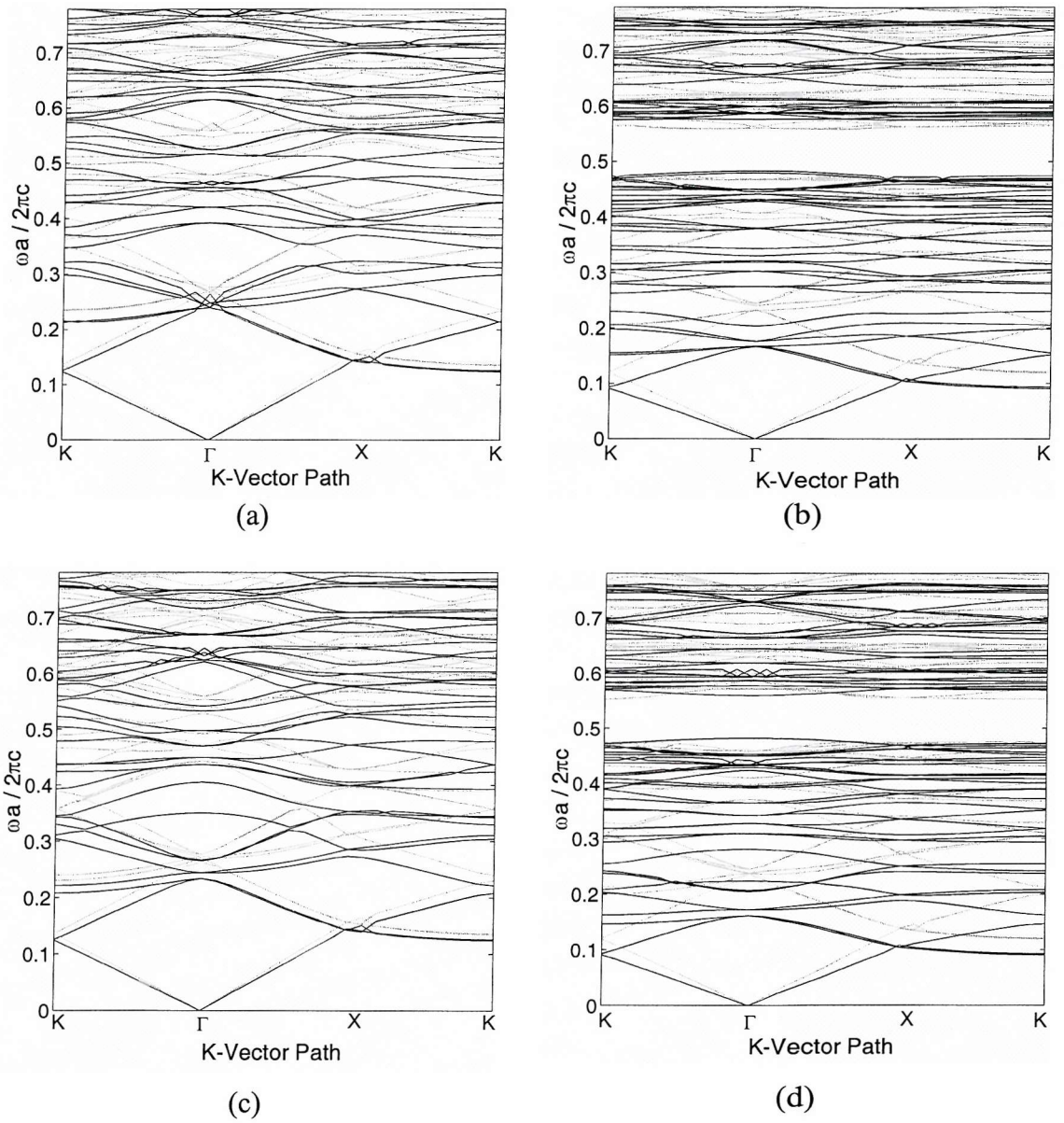

Figure 5-4 Dispersion relations for: (a) 'triangle-triangle' configuration of air rods in SiN substrate; (b) 'triangle-triangle' configuration of air rods in a GaAs substrate; (c) 'square-square' configuration of air rods in SiN; (d) 'square-square' configuration of air rods in a GaAs substrate. r/a = *0.5 for all crystals. The solid and broken curves correspond to the transverse electric (TE) and transverse magnetic (TM) polarisations respectively.*

A similar analysis was made for both quasicrystal configurations, but with a significantly smaller *r/a* of 0.3. The resulting density of states diagrams (Figure 5-5) allow direct comparison

with the results presented in (Zoorob, Charlton et al. 2000). The diagrams are similar in their key features, namely the presence of two band gaps in the TM mode centred at 0.22 and 0.275 $\omega a/2\pi c$. The gap width to mid gap ratios of these gaps in Figure 5-5 *(a)* are 9% and 4% for the lower and higher gaps respectively. In Figure 5-5 *(b)*, the gap width to mid gap ratios are significantly different at 4.5% and 8%. In addition, there is a pronounced peak in density of states in the TE mode in Figure 5-5 *(a)* across the lower frequency band gap that is not present in Figure 5-5 *(b)* and a significant reduction in the density of states for the TE mode within the higher frequency gap in Figure 5-5 *(b)* that is not present in Figure 5-5 *(a)*.

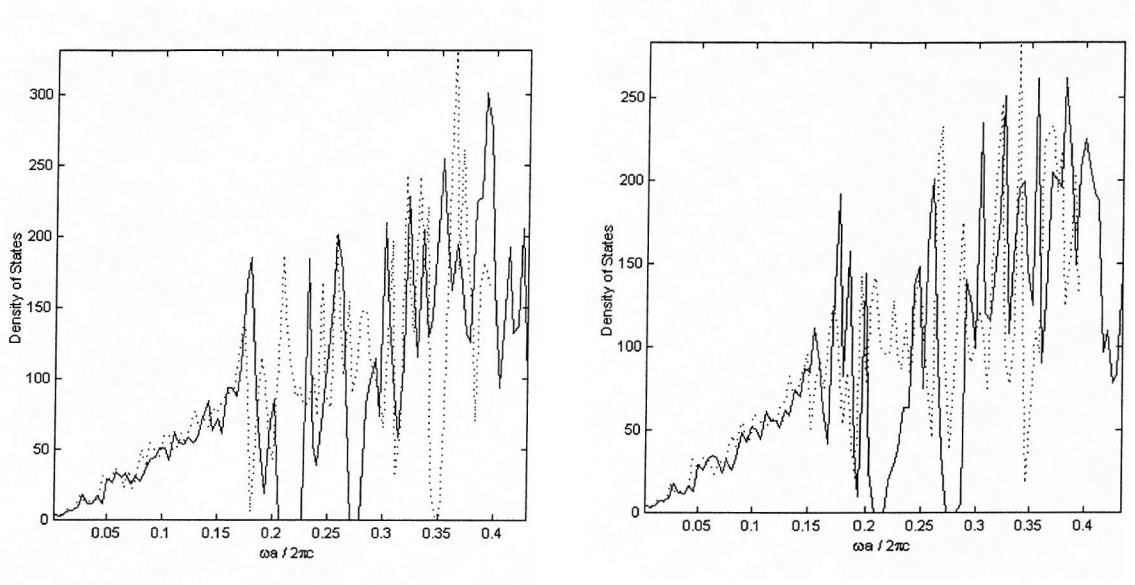

(a) *(b)*

Figure 5-5 Density of states diagrams for triangle-triangle (a) *and square-square* (b) *quasicrystal configurations. Air rods in a gallium arsenide substrate, dielectric constant = 11.4, r/a=0.3. The solid and broken curves correspond to the transverse electric (TE) and transverse magnetic (TM) polarisations respectively.*

It has been proposed that complete band gaps exist for 12-fold symmetric quasicrystal PCs consisting of air rods in substrate materials with a dielectric constant as low as 2.1 (corresponding to glass) (Zoorob, Charlton et al. 2000). FEM analyses of the equivalent PC structures presented in that paper were computed, the density of states diagrams are shown in Figure 5-6. Diagram *(a)* corresponds to a quasicrystal with an rod radius to pitch length ratio of 0.3 (corresponding to a filling fraction of 30%) and a background dielectric constant of 4.1, equal to that of silicon nitride, a common material in opto-electronic components (Netti, Charlton et al. 2000). Diagram *(b)* corresponds to a quasicrystal with an *r/a* of 0.3 and a background dielectric constant of 2.1, equal to that of glass, again a commonly used opto-

electronic material. The FE analysis does not produce a complete band gap in either of these cases. A small band gap centred at 0.355 was present in the silicon nitride case for the TE polarisation. However, this is in agreement with a recent publication examining the spectral properties of these structures using the multiple scattering method (Xiangdong, Zhao-Qing et al. 2001). The absence of a complete band gap for air holes in silicon nitride suggests that air holes in glass will not possess such a gap either, as the dielectric contrast between rod and background material is further reduced. Figure 5-6 *(b)* confirms this prediction with no band gaps in either TE or TM modes although there is a significant reduction in density of states in both modes at 0.42 $\omega a/2\pi c$.

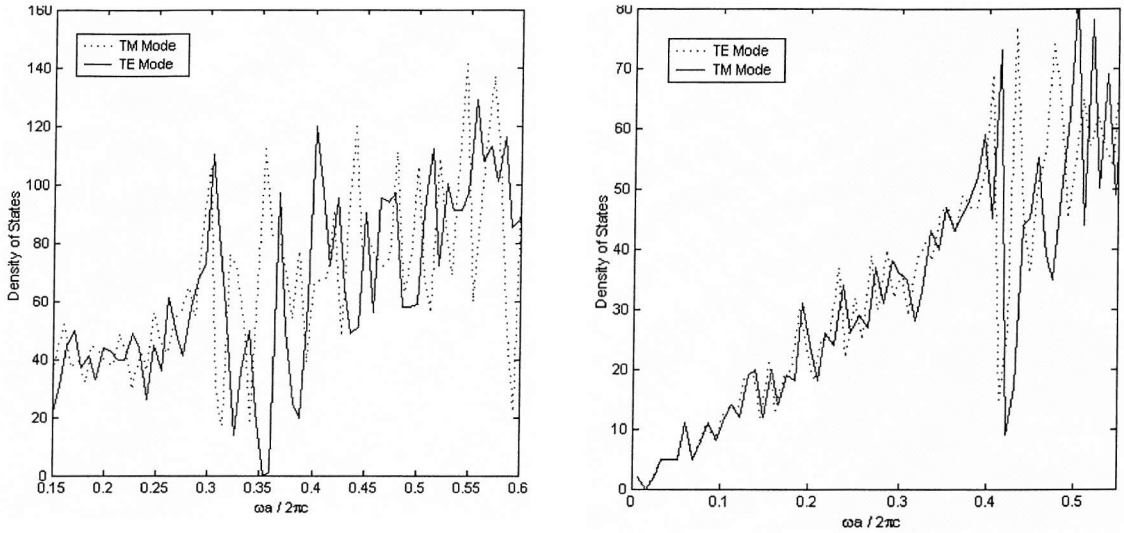

Figure 5-6 Density of states diagrams for a triangle-triangle quasicrystal configuration with r/a = 0.3: (a) *substrate dielectric constant = 4.1 (silicon nitride)* (b) *substrate dielectric constant = 2.1 (glass).*

The agreement of Figure 5-6 *(a)* with the equivalent analysis presented in (Xiangdong, Zhao-Qing et al. 2001) prompted further comparison with their results. Figure 5-7 *(a)* is a density of states diagram for a quasicrystal with a filling fraction of 75% and a background dielectric constant of 8.9. This diagram shows excellent agreement with a robust TM mode band gap centred at 0.38 $\omega a/2\pi c$ and a complete band gap at 0.49 $\omega a/2\pi c$. The gap width to mid-gap ratio of the complete band gap is 61%. Figure 5-7 *(b)* is a density of states diagram for a quasicrystal with a filling fraction of 54% and a background dielectric constant of 11.4. This corresponds to Figure 6 in (Xiangdong, Zhao-Qing et al. 2001) and also shows excellent agreement, particularly in the complete band gap centred at a normalised frequency of 0.5.

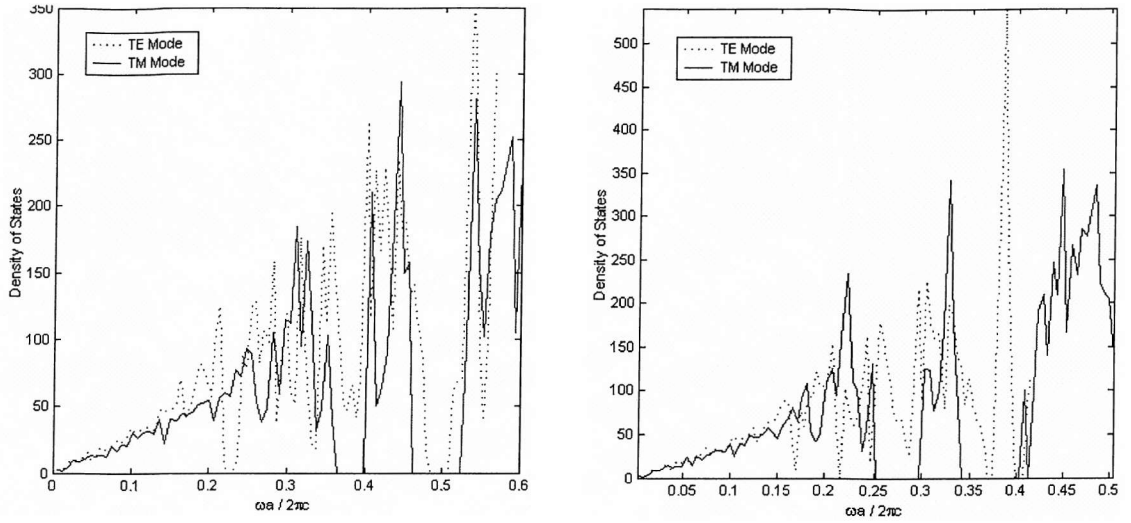

Figure 5-7 Density of states diagrams for (a) *air-rods in a substrate material of dielectric constant = 8.9, r/a = 0.47* (b) *air-rods in a substrate material of dielectric constant = 11.4, r/a =0.40.*

Band gap maps of the normalised frequency range of TE and TM mode band gaps plotted against the filling fraction are displayed in Figure 5-8. Hence, one can easily observe the filling fraction that produces the optimum PBG. The results are shown in Figure 5-8. While band-gaps do appear in both the TE and TM modes for a substrate material with a permittivity as low as 4.1 there is no overlap, hence no complete PBG. Increasing the dielectric contrast does result in a complete band gap as can be seen for air rods in GaAs with an *r/a* between 0.39 and 0.5. The maximum frequency range of the gap is 0.47 to 0.55 $\omega a/2\pi c$. Swapping the dielectric materials so that we have GaAs rods set in air increases the range of rod radii that produce a complete gap to between 0.21 and 0.46 *r/a* with the maximum frequency range also increasing at 0.32 to 0.58 $\omega a/2\pi c$.

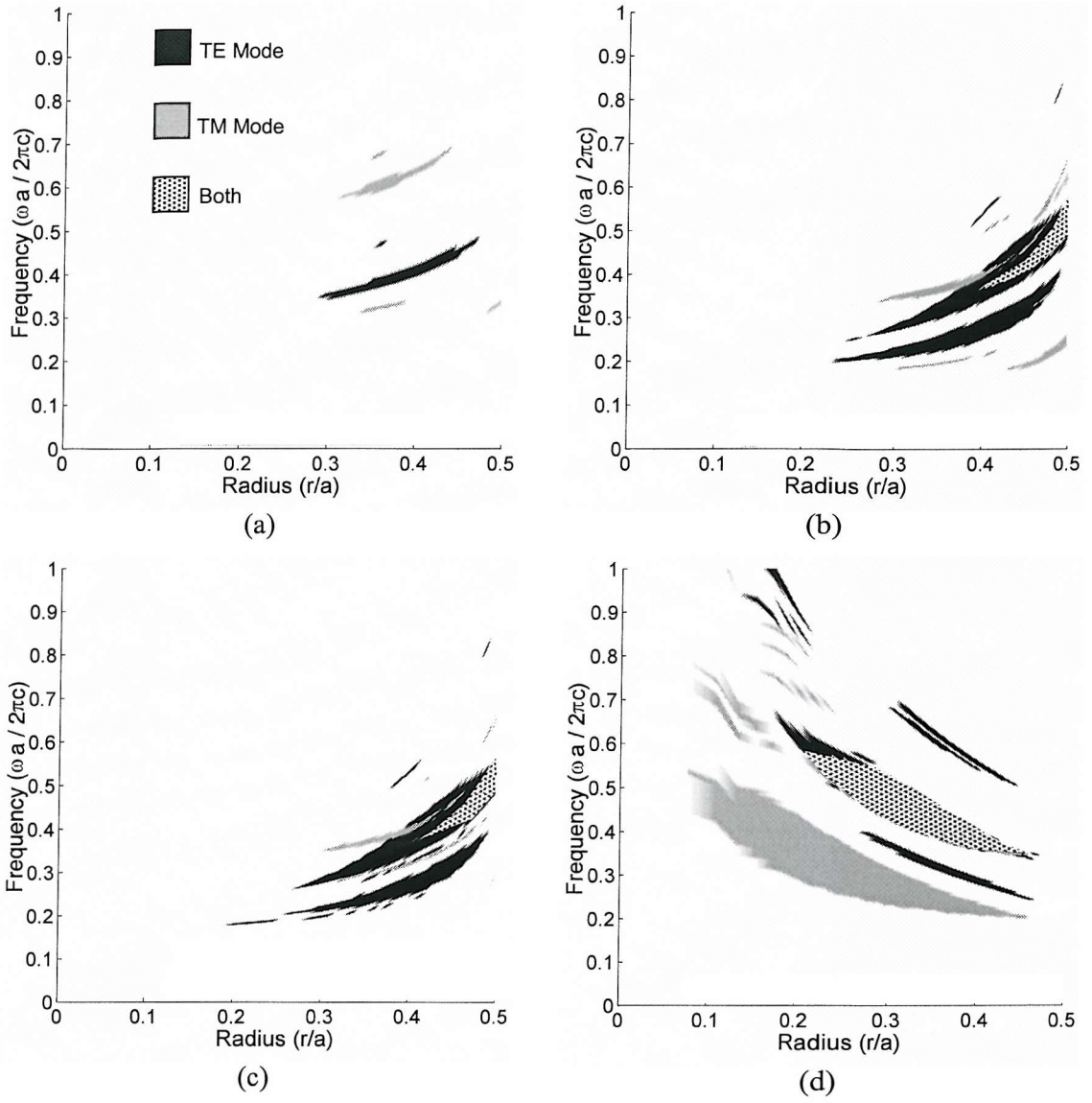

Figure 5-8 Gap-maps for various quasicrystals: (a) 'triangle-triangle' configuration of air rods in SiN. (b) 'triangle-triangle' configuration of air rods in GaAs, (c) 'square-square' configuration of air rods in GaAs. (d) 'triangle-triangle' configuration of GaAs rods in air. The filling fraction is expressed as the ratio of rod radius to the pitch (r/a).

Validation of our results can be made through comparison with other tried and tested numerical methods and experimental data. Figure 5-9 compares the results of our FEM code (a) with the equivalent analysis using a finite difference time domain code (b) and actual experimental data (c). The PBG device in each case was a 'triangle-triangle' configuration 12-fold symmetric quasicrystal of consisting of air rods etched into a silicon nitride substrate. The filling fraction, *r*/a, was set at 0.23. All three diagrams show strong attenuation in the normalised frequency at 0.35 $\omega a/2\pi c$.

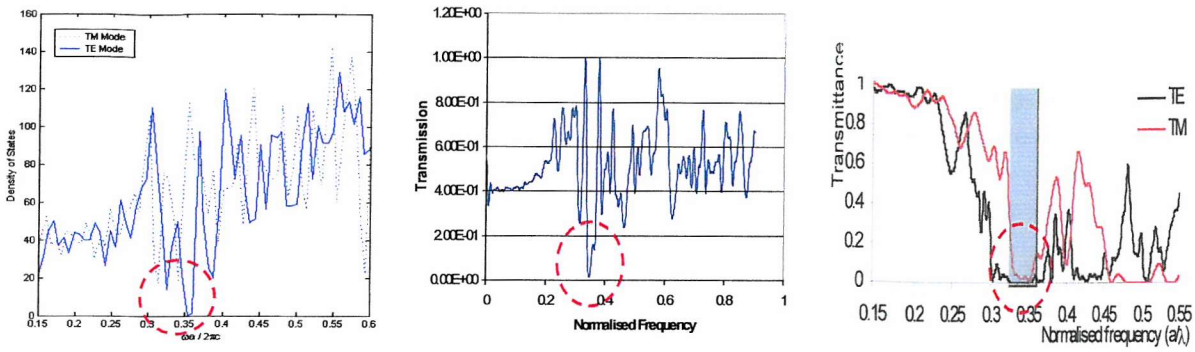

(a) (b) (c)

Figure 5-9 Comparison of results for a 'triangle-triangle' configuration quasicrystal of air rods in silicon nitride, filling fraction = 30%. (a) Finite Element Method, (b) Finite Difference Time Domain courtesy of Majd Zoorob, (c) Experimental Data courtesy of Martin Charlton, Caterina Netti, Greg Parker and Jeremy Baumberg, ECS and Physics Dept. University of Southampton.

5.3 Introduction of Crystal Defects

The effect of introducing a defect into an otherwise highly ordered PC structure has prompted much interest. The defect could be a variation in the dielectric constant of a rod, alteration of a rods diameter or complete removal of a rod or rods (see Figure 5-10). The effect of these defects can then be ascertained from the FEM output. The aim is to use defects to control the frequency and range of photonic band-gaps.

The introduction of defects into a crystal structure can cause a single mode or closely spaced modes to propagate that have a frequency within the range of the band gap. In this case the defect induced mode cannot propagate through the crystal as it has a frequency within the forbidden range hence the light is localised and cannot escape, the mode is effectively 'pinned' by the defect (Joannopoulos, Meade et al. 1995).

The effect of introducing a localised defect to the quasi-crystal unit cell is presented in Figure 5-10. The defect is constituted by the removal of the central rod. The resulting density of states diagram however, does not show any significant differences when compared with the standard quasi-crystal.

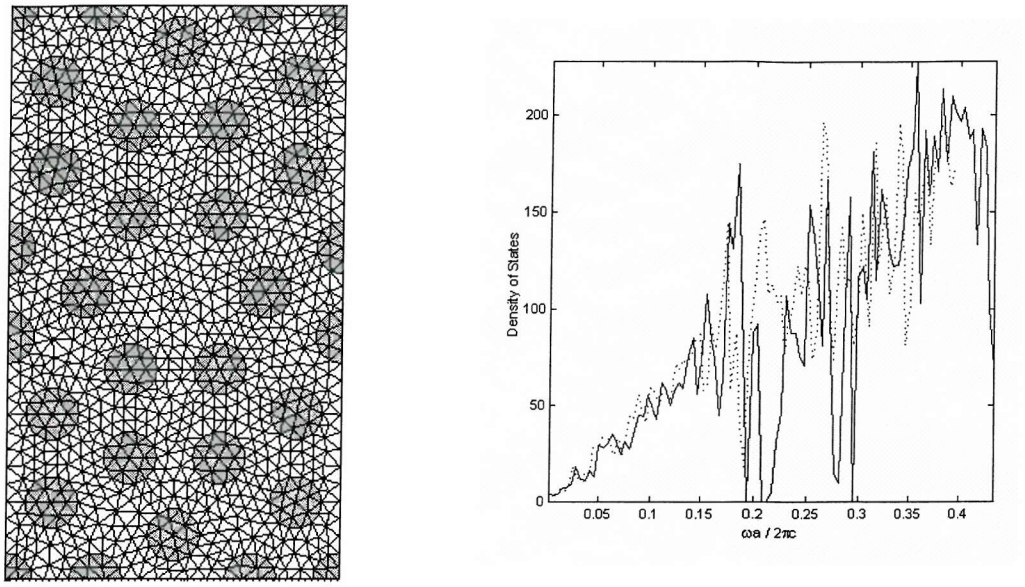

Figure 5-10 Quasicrystal with a central rod defect; mesh and density of states diagram; r/a = 0.3, substrate dielectric constant = 11.4.

5.4 Conclusions

The 12-fold symmetric quasicrystal does produce complete band gaps but not for especially low dielectric contrasts, e.g. air rods in SiN or glass. Complete band gaps appear as the dielectric contrast increases, and as the rod radius to pitch length increases. Swapping rod/substrate materials such that the PC consists of high dielectric rods in a low dielectric substrate also increases the frequency range of the band gaps. In comparison with a standard triangular lattice, there is little advantage in the band gaps produced in using a quasicrystal rod arrangement. There is however the increased order of rotational symmetry (6 to 12), which makes the structure less sensitive to the angle of incidence of the incoming light resulting in a more homogeneous band-gap.

Comparison of results produced with the finite element code show excellent agreement with those produced using other numerical methods, including finite difference time domain and also with experimental data. The accuracy of the finite element code coupled with its efficiency, both in terms of computation and memory requirements make it a very attractive approach to photonic crystal modelling.

6 Photonic Crystal Design Optimisation

The objective so far has been to accurately model a photonic crystal's band structure. However, as stated previously in chapter 5, it is desirable to design a photonic crystal that exhibits a large band gap. There are two approaches to fulfilling this design brief. The first is to analyse the results from a selection of judiciously chosen meshes. By coupling this information with an understanding of the underlying physics one can formulate a hypothesis as to what properties constitute a photonic crystal structure that exhibits a large photonic band gap.

The second approach is to design and implement an optimisation procedure that does its best to find the crystal structure that produces the largest band gap. Essentially, optimisation involves simply finding the parameter set that produces a maximum or minimum value of a function. In this case the parameter set is the photonic crystal definition, the function is the FE code and the value we are aiming to maximise is the size of the photonic band gap.

Implementation of the optimisation procedure involves coding additional software modules to work in conjunction with the FE code. These include an automatic mesh generator capable of producing a domain discretisation from a photonic crystal geometry definition file, a post processing code used to detect and measure the size of any band gaps in the band structure, and a minimisation algorithm to search the parameter space attempting to find the crystal with the largest band gap. The integration of these modules with the FE code constitutes the optimisation procedure. A schematic of this process is shown in Figure 6-4.

The optimisation procedure may need to iterate over many crystal designs in order to converge to a maximum, hence this approach is only feasible subsequent to the development of the FE code which provides a fast and efficient numerical algorithm for photonic crystal modelling.

6.1 Automated Mesh Generation

The optimisation process requires a mesh generation code that can create a domain discretisation from a high-level photonic crystal definition. Matlab functions were developed to act as a front end to the meshing algorithm, Geompack90 (Joe 2001). These allow the specification of crystal structures using a higher level of abstraction, e.g. the structure can be expressed in terms of the lattice vectors that describe the unit cell and the coordinates and radii of the rods within that cell. The code converts this information into the necessary input format for Geompack90. Geompack90 then produces the desired mesh representation of the photonic

crystal. The code also performs any periodic mapping that is necessary for materials that overlap the unit cell boundaries. The mesh generation is not limited to rods in a substrate, any polygonal material structure can be specified within a quadrilateral unit cell. An example of an input file for the automated mesh generation can be seen in Figure 6-1.

```
% mesh name
hexunit_ne_500_ff_83

% lattice vectors
% [x y]
1 0
0.5 0.8660254038

% rod configuration
% [x y r]
0.00 0.00 0.47
```

Figure 6-1 Example photonic crystal geometry definition file.

The data in the file is read and subsequently all photonic crystal features are analysed to see if they intersect the unit-cell boundary. If this occurs (as shown in Figure 6-2) the sections of an intersecting feature are divided and moved to the relevant position on the opposing boundaries to represent tiling of the unit-cells.

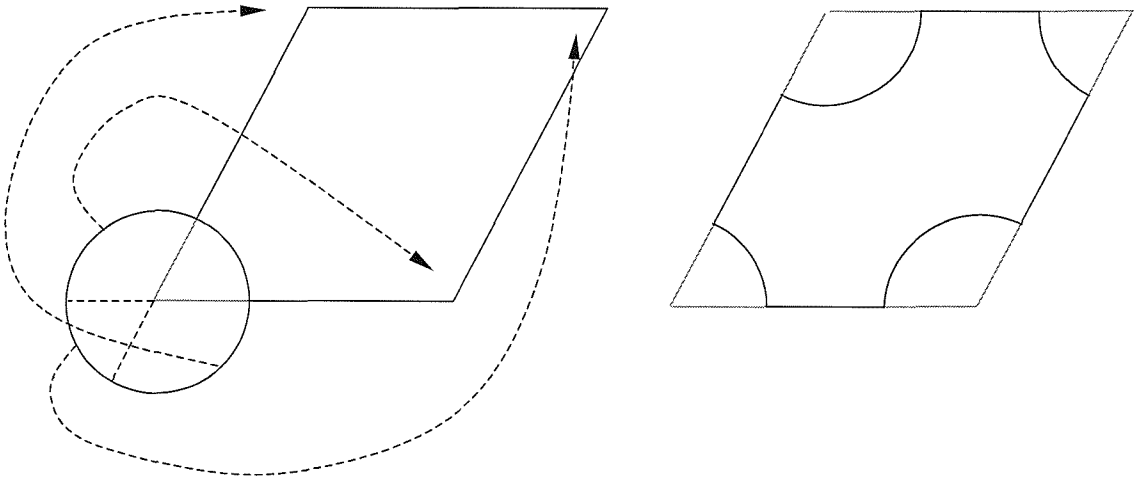

Figure 6-2 Imposition of periodic boundary conditions upon the photonic crystal structure.

Once the periodicity of the structure has been enforced and all features lie within the unit cell the features are discretised into sets of points. These points represent element vertices at the

material boundaries. The number of these points is computed as a function of the total desired number of elements in the final mesh representation. Blue dots represent the vertices along the unit-cell boundary with red dots representing 'cookie-cutter' outlines of the features within the cell. Material markers can be set for regions that are enclosed by a set of points that can subsequently use to specify different material properties in the FE code.

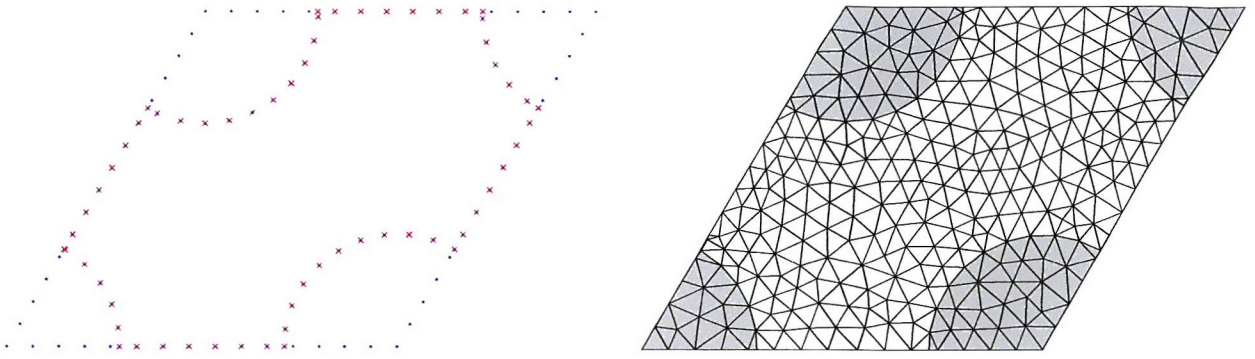

Figure 6-3 Point based representation of the crystal structure and subsequent unstructured triangular mesh based representation of the structure.

The information generated is saved as three separate files; the required input format for Geompack90. These are distinguished by their file extension, `*.m2`, `*.rg2` and `*.cs2`. The `*.m2` file is the initial input file for Geompack90. It specifies the type of meshing operation to be performed, e.g. 2D, 3D, surface mesh, volume mesh, tetrahedral, hexahedral etc. It also specifies the names of the relevant `*.rg2` and `*.cs2` files. A number of other parameters are specified that control factors such as the number of elements and the geometrical properties of those elements. A detailed explanation can be found in '*Geompack90 Meshing Operations*' (Joe 2001). The `*.rg2` file contains all the boundary vertices information including their spatial coordinates, material properties, enclosed region properties and feature topology (a clockwise description of all the points that constitute a feature). The `*.cs2` file describes the edge topology and associated edge properties. A detailed explanation of these two file types can be found in '*Geompack90 File Formats for Regions and Meshes*' (Joe 2001). The output from Geompack90 consists of a single `*.mh2` file which lists all the element vertices and their material markers along with the mesh topology detailing the connectivity of those vertices. This output file can be visualised as shown in Figure 6-3. Note that the '2' in these file extensions refers to the fact that we are dealing with two-dimensional meshes. Geompack90 can also produce three-dimensional meshes with the relevant files being replaced by their '3' extension counterparts, e.g. `*.m3`, `*.rg3`, `*.cs3` and `*.mh3`.

6.2 Eigenvalue Analysis

It is necessary to detect and measure the presence of any band gaps from the set of eigenvalues produced by the FE code. This is achieved by concatenating the set of $n \times k$ eigenvalues into one vector. This vector is then sorted into values of ascending order. Subsequently, the difference between adjacent values is computed. The maximum of these values corresponds to the absolute size of the largest band gap, equation (6.1).

$$\begin{bmatrix} \lambda_{11} & \lambda_{12} & \lambda_{13} & \dots & \lambda_{1n} \\ \lambda_{21} & \lambda_{22} & & & \\ \lambda_{31} & & \lambda_{33} & & \\ \vdots & & & \ddots & \\ \lambda_{k1} & & & & \lambda_{kn} \end{bmatrix} \rightarrow \begin{bmatrix} \lambda_1 < & \lambda_2 < & \lambda_3 < & \dots & \lambda_{k\times n} \end{bmatrix} \tag{6.1}$$

$$d_i = \lambda_{i+1} - \lambda_i$$

$$\text{Largest photonic band gap} = \max \begin{bmatrix} d_1 & d_2 & d_3 & \dots & d_{(k\times n)-1} \end{bmatrix}$$

Comparison of the frequency ranges of photonic band gaps can be misleading due to the scaling properties of Maxwell's equations (see chapter 2.3). For example, simply scaling up a crystal structure's dimensions will increase the frequency range of the band gap. So, to restate our optimisation goal of producing the largest band gap, all we need do is increase the dimensions of the crystal structure. In practice, although the bandwidth of the gap increases, the frequency range in which the gap exists drops. In order to make useful comparisons between photonic band gap devices we need to characterise the gaps in terms independent of scale. This can be done by simply dividing the band gap width, $\Delta\omega$, by the mid-point of the gap, ω_0,to give the gap to mid-gap ratio, $\Delta\omega/\omega_0$. This measure of the band gap is constant, regardless of scaling issues.

6.3 Function Minimisation: The Downhill Simplex Method

To complete the optimisation procedure we need to implement the maximisation algorithm that will attempt to find the crystal with the largest band gap. Although we are trying to maximise the band gap size we actually implement a minimisation algorithm. In reality, the difference between maximisation and minimisation algorithms is a trivial one, as a function, f, could just as easily be posed as the function, $-f$. Our objective is to maximise the normalised frequency range of the photonic band gap hence we aim to minimise the reciprocal of the band gap size. The

independent variables are the values specified in the photonic crystal structure configuration file. The downhill simplex method (Nelder and Mead 1965) is a multidimensional minimisation algorithm allowing one to find the minimum of a function with more than one independent variable. The algorithm is an obvious choice for this purpose, as it requires only function evaluations and not their derivatives. Although not the most efficient of approaches its relative simplicity does allow rapid implementation allowing results to be computed quickly and easily, hence it is particularly suitable when the computational cost is low.

The algorithm takes an initial guess vector, **v**, of length n as input. The vector values v_1 , v_2 , ... v_n contain the photonic crystal definition parameters as contained in the definition file (see Figure 6-1), e.g. the rod radius values and their centre coordinates. The algorithm then iterates through an n-1 dimensional space attempting to find the vector **v** that gives the maximum sized photonic band gap. The algorithm terminates when the convergence tolerance is reached.

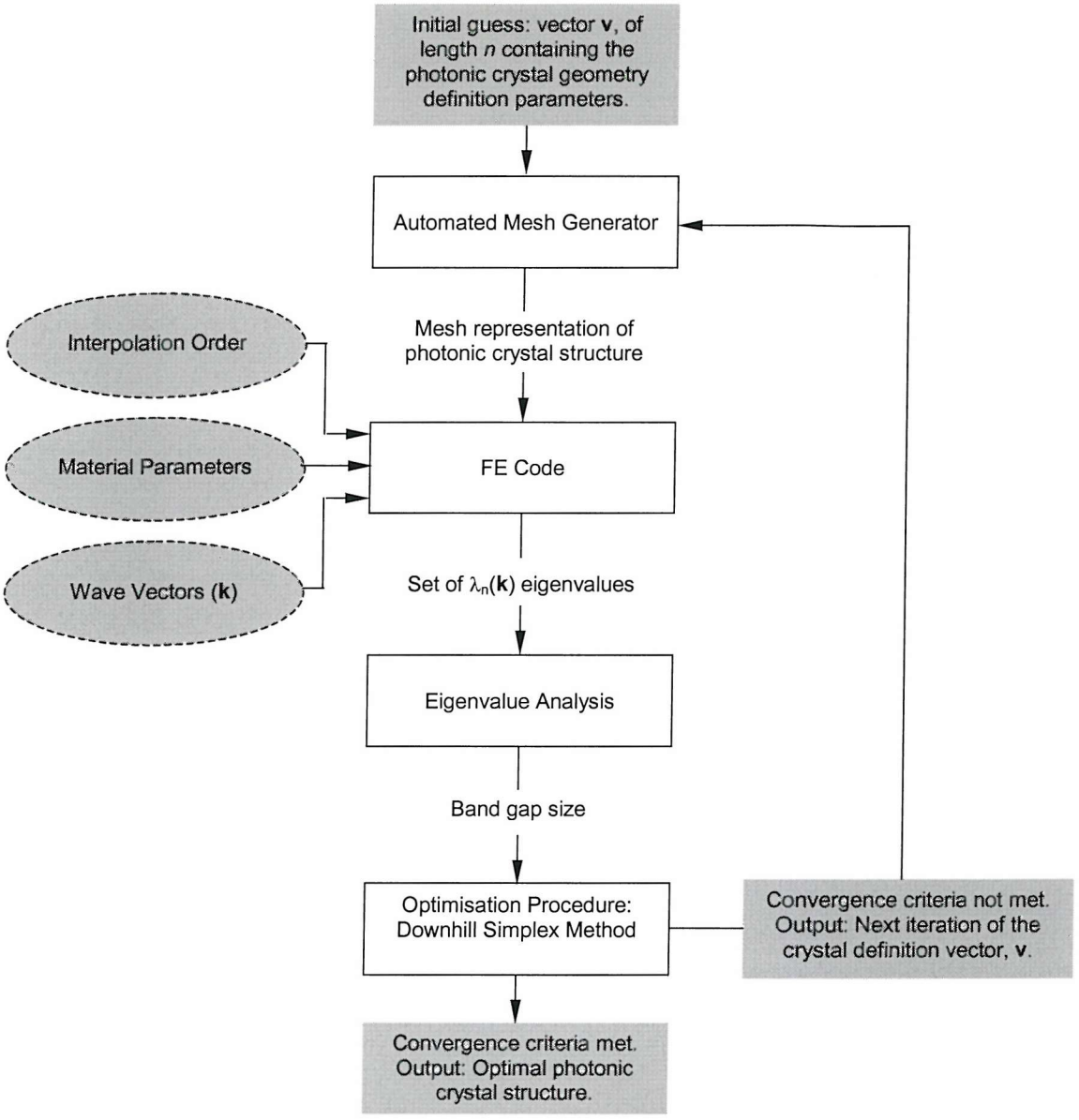

Figure 6-4 Schematic of the photonic crystal optimisation process.

The initial-guess crystal definition is fed into the automated mesh generation module. This produces a mesh representation of the structure in a format that can be input into the FE module. Additional parameters are given including the dielectric constants of the constituent materials and the desired number of eigenvalues and the interpolation order.

The material permittivity parameters are not included in the PBG device definition for two reasons:

1. Whilst the geometry parameters may be varied continuously, the permittivity takes on discrete values corresponding to the physical properties of actual materials; hence optimisation of the material dielectric constants cannot be practically applied to the

manufacturing process. As a general heuristic, the size of the photonic band gap will increase with the dielectric contrast between the constituent materials. In practice, as the permittivity of the materials increases they become more lossy, thereby reducing transmission through the device. Therefore, our model, which is based on the fundamental assumption that we are dealing with lossless materials, becomes less applicable.

2. Permittivity is a difficult property to measure or specify because it depends not only on the intrinsic properties of the material itself but also on the test method, the test frequency and the conditioning of the samples before and during the test.

Therefore, in our analysis, the photonic crystal geometry is optimised but the material properties are chosen to be commonly used optoelectronic materials, for example, silicon nitride and gallium arsenide.

The band structure is computed giving the set of eigenvalues, $\lambda_n(\mathbf{k})$. This data is processed by the eigenvalue analysis module which detects and measures the size of any photonic band gaps. This band gap information is fed back into the downhill simplex method algorithm. This then generates another photonic crystal definition vector in an attempt to improve the band gap. If the algorithm has reached a minimum, e.g. the convergence tolerance has been reached, the process terminates and the resulting crystal structure is a local optimum.

6.4 PBG Device Optimisation: Brute Force Approach

The optimisation procedure needs an 'initial-guess' photonic crystal definition from which to start the function minimisation. The number of iterations necessary before the downhill simplex method converges can be significantly reduced if this initial guess is a good one, e.g. the crystal structure already exhibits a reasonably sized photonic band gap. A brute force approach was used to obtain this initial guess; one thousand unit-cell meshes were generated with random arrangements of rods and random rod radii. Twenty crystal structures exhibiting the largest gap to mid-gap ratios were selected from the initial 1000 and subsequently used as initial guesses for the optimisation procedure.

Table 6-1 presents the optimisation results. The initial and final band gap measurements are given along with the percentage improvement produced by the optimisation procedure. The data clearly shows that in almost all cases the optimisation has significantly improved the size of the

band gap. The best improvement was seen for rand_mesh_2_0.9_28 with an improvement in the band-gap to mid-gap ratio of 264.3%. The mean improvement was 70.3%.

Mesh Name	Initial $\Delta\omega/\omega_0$	Final $\Delta\omega/\omega_0$	% Improvement
quasi_mesh_1_1.7_1	0.118	0.182	53.7
quasi_mesh_3_1_9	0.105	0.157	49.5
quasi_mesh_3_1_12	0.101	0.157	55.9
quasi_mesh_3_1_11	0.109	0.157	43.6
quasi_mesh_3_1_22	0.112	0.156	39.4
quasi_mesh_3_1_38	0.108	0.156	44.3
quasi_mesh_3_1_73	0.106	0.156	47.6
quasi_mesh_3_1_25	0.106	0.156	46.6
quasi_mesh_3_1_13	0.110	0.154	40.1
quasi_mesh_1_1.1_1	0.109	0.110	1.2
rand_mesh_2_0.9_168	0.015	0.053	241.6
rand_mesh_2_0.9_149	0.016	0.051	216.8
rand_mesh_2_0.9_28	0.014	0.051	264.3
rand_mesh_2_1_5	0.037	0.049	33.1
rand_mesh_2_0.9_79	0.022	0.048	120.8
rand_mesh_2_1_37	0.039	0.046	17.0
rand_mesh_4_0.6_132	0.024	0.038	60.0
rand_mesh_4_0.6_52	0.024	0.038	57.9
rand_mesh_2_1_39	0.036	0.037	3.6
rand_mesh_2_0.9_2	0.011	0.012	9.1

Table 6-1 Band-Gap optimisation results for the top twenty meshes.

The two meshes exhibiting the largest band gaps were quasi_mesh_1_1.7_1 and quasi_mesh_3_1_12. Further data for these two meshes can be seen in Figure 6-5 and Figure 6-7 respectively. The density of states diagrams for the crystal structures are plotted before and after the optimisation procedure. This clearly indicates the change in size and position of the TE and TM mode band-gaps. The convergence of the minimisation algorithm is presented by plotting the gap to mid-gap ratio against the number of iterations. There is oscillation in the quality of the band gap through each iteration but the clear trend is that of convergence to an optimum sized band-gap.

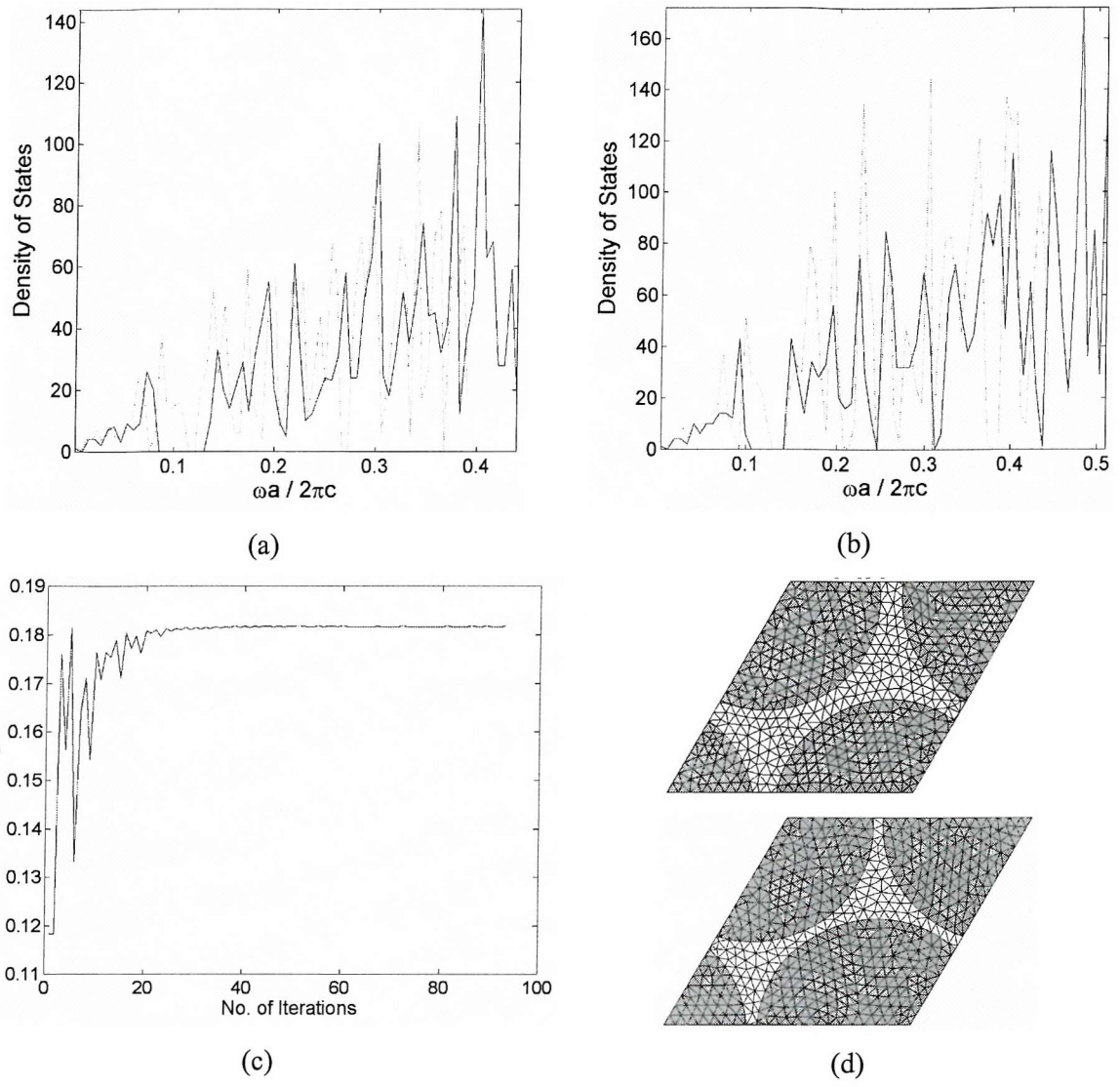

Figure 6-5 Optimisation results for the randomly generated mesh, quasi_mesh_1_1.7_1. The density of states is plotted for the crystal before optimisation (a) and after optimisation (b). The convergence of the minimisation algorithm is shown by plotting the band-gap to mid-gap ratio against the number of iterations (c). The initial (above) and final (below) meshes are shown in (d).

The meshes from before and after the optimisation process are shown and it is clear that they are very similar, the position of the rod centres remains virtually unchanged with the only difference being a slightly increased rod radius for the post-optimisation mesh. This same characteristic is true of the other twenty meshes. Thus we can conclude that slight alterations in the input mesh can lead to large apparent improvements in the size of the resulting photonic band gaps. This could have important consequences in the fabrication of photonic band gap devices. If such small alterations in the crystal geometry lead to large changes in the band structure it is clear that the highly accurate fabrication techniques must be employed if the

resulting crystal is to have the desired optical properties.

It is also of interest that both meshes are very similar in geometry to that of the triangular lattice as presented previously in 3.2. This is the structure that allows the largest filling fraction to be achieved; therefore it seems sensible to propose the heuristic that the size of the photonic band gap increases with the filling fraction of the crystal structure.

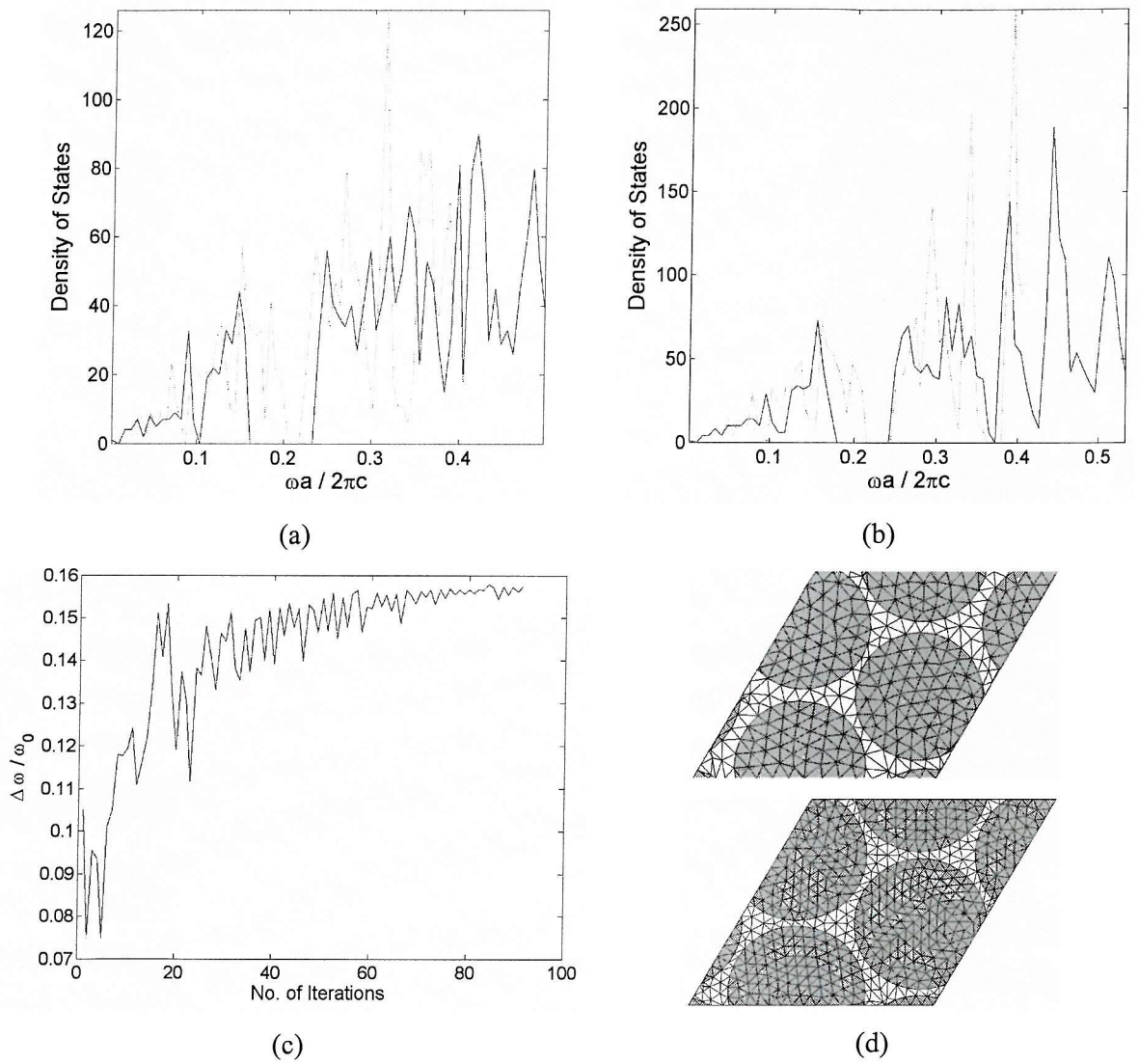

Figure 6-6 Optimisation results for the randomly generated mesh, quasi_mesh_3_1_9. The density of states is plotted for the crystal before optimisation (a) and after optimisation (b). The convergence of the minimisation algorithm is shown by plotting the band-gap to mid-gap ratio against the number of iterations (c). The initial (above) and final (below) meshes are shown in (d).

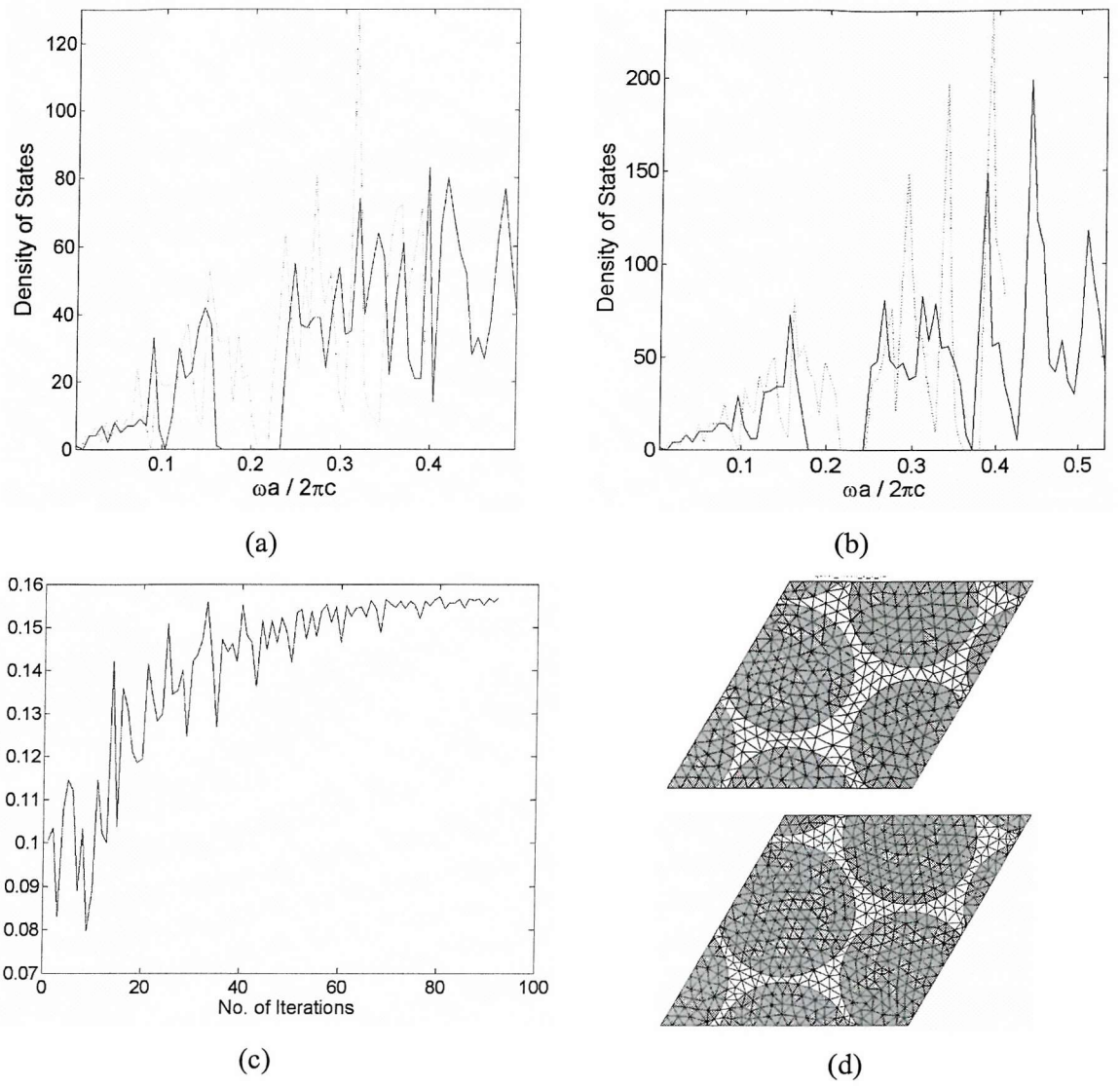

Figure 6-7 Optimisation results for the randomly generated mesh, quasi_mesh_3_1_12. The density of states is plotted for the crystal before optimisation (a) and after optimisation (b). The convergence of the minimisation algorithm is shown by plotting the band-gap to mid-gap ratio against the number of iterations (c). The initial (above) and final (below) meshes are shown in (d).

6.5 PBG Device Optimisation: Canonical Forms Approach

The geometric arrangement of rods in a substrate can be considered simply as dot patterns if one ignores the rod radius. It can be stated that there exist two infinite families of types of non-trivial finite dot patterns, each depending on a positive integer n, seven types of strip dot patterns, and thirty types of periodic patterns (Grünbaum and Shephard 1987). Analysis of these fundamental arrangements of rods has been performed to ascertain if any show particular potential as a basis for a photonic band gap device. This approach increases the efficiency of the generation of the 'initial guess' by significantly reducing the number of analyses that need to be

performed prior to the optimisation procedure. In the same way as the brute force approach, those structures that exhibit the largest photonic band gaps are then further examined using the optimisation codes.

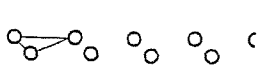
DPS7

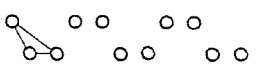
DPS9

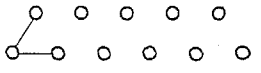
DPS11

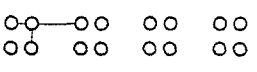
DPS12

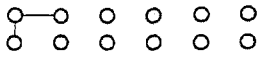
DPS13

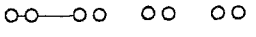
DPS14

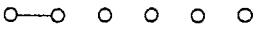
DPS15

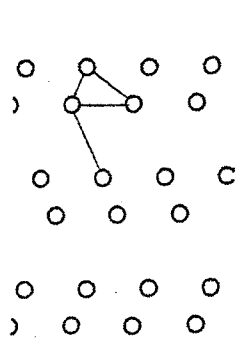
DPP9

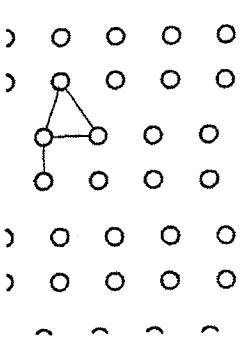
DPP11

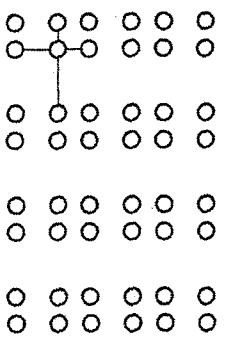
DPP14

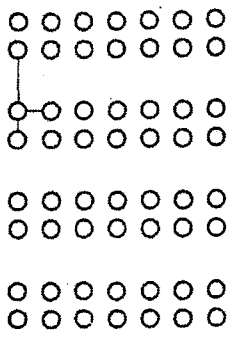
DPP15

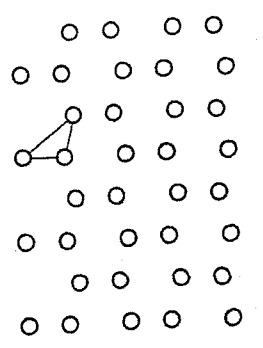
DPP19

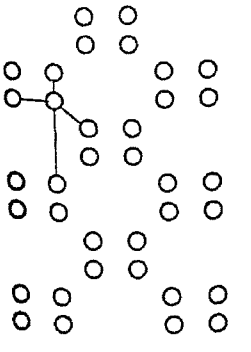
DPP17

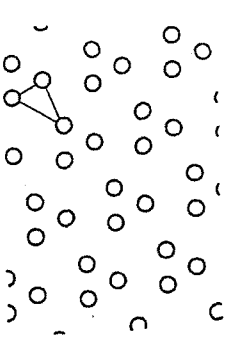
DPP21

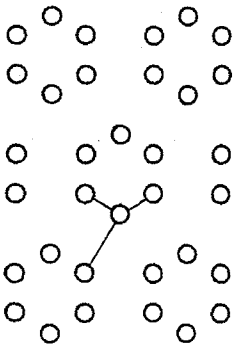
DPP23

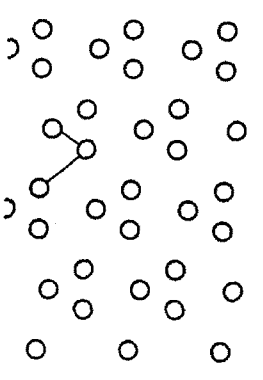
DPP25

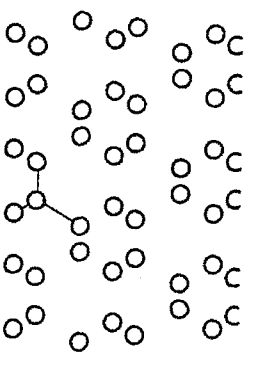
DPP27

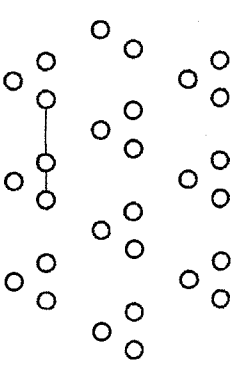
DPP28

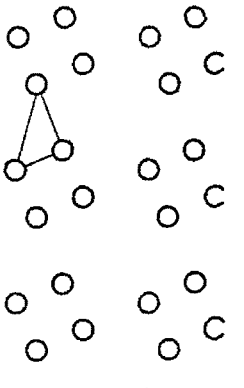
DPP30

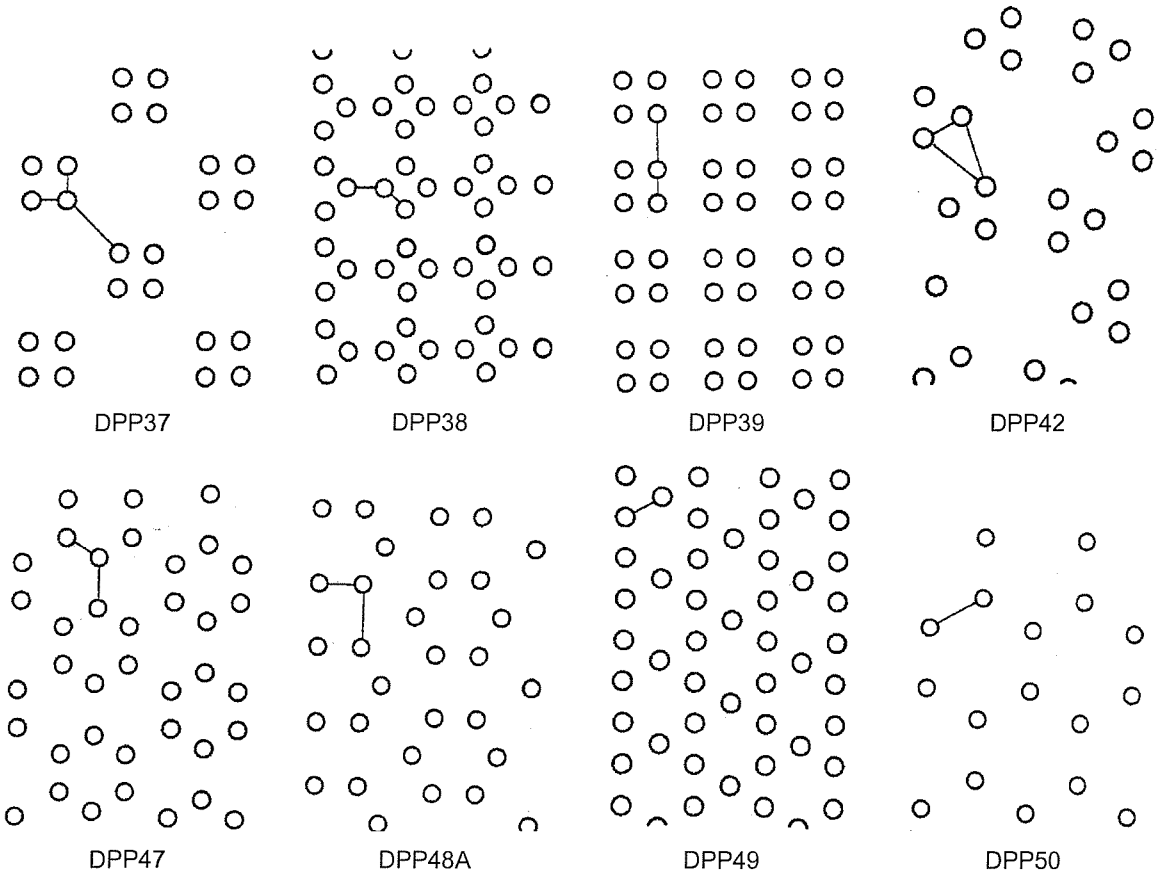

Figure 6-8 Examples of the types of periodic dot patterns, reproduced courtesy of (Grünbaum and Shephard 1987).

Meshes of varying rod radii were generated for each canonical form. They ranged from 0.06 upwards in 0.02 increments until the rods overlapped. These measurements were relative to a unit cell with lattice vectors with a magnitude of 1. Considering air rods in a GaAs substrate each mesh was analysed using a 1000 element mesh and 2nd order interpolation functions. This allowed the generation of band gap map data sets for each canonical form. Two of these data sets are presented in Figure 6-9. They highlight the rod radius corresponding to the largest photonic band gap and also highlight the difference in maximum potential filling fractions for different canonical form geometries.

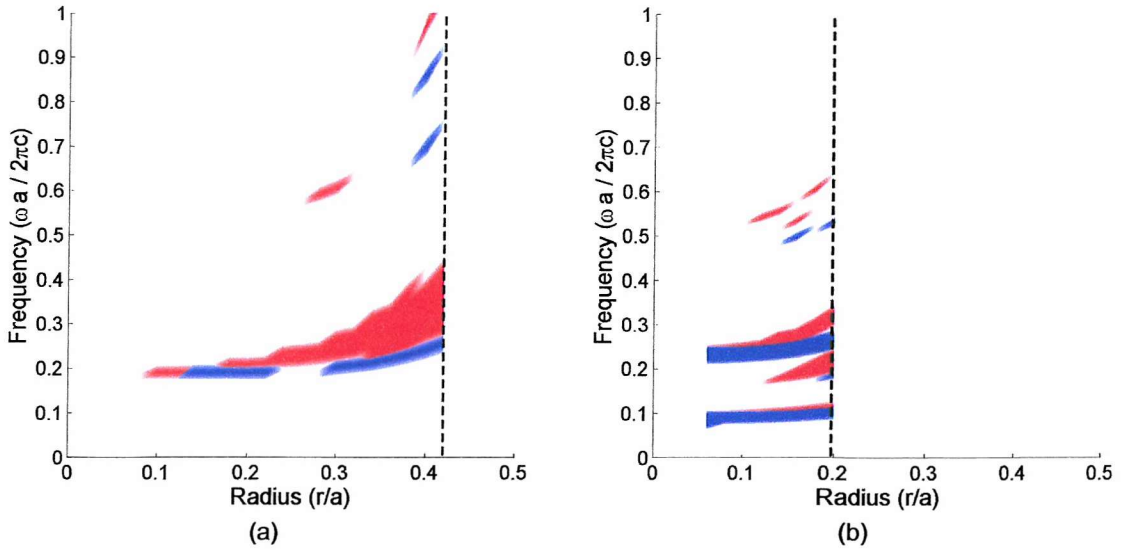

Figure 6-9 Gap-maps for (a) DPS11 and (b) DPP27 canonical forms. The vertical dashed lines represent the maximum rod radius before the rods overlap and the substrate becomes disconnected.

The gap map data for each canonical form was analysed and the ten meshes that produced the largest bad gaps were selected for optimisation, the results of which can be seen in Table 6-2.

Mesh Name	Initial $\Delta\omega/\omega_0$	Final $\Delta\omega/\omega_0$	% Improvement
DPS11_ne_500_r_0.42	0.042	0.110	158.8
DPP47_ne_500_r_0.12	0.071	0.071	0.0
DPP27_ne_1000_r_0.12	0.030	0.070	131.6
DPP49_ne_500_r_0.22	0.060	0.061	0.3
DPP23_ne_500_r_0.14	0.060	0.060	0.0
DPP48A_ne_500_r_0.14	0.055	0.055	0.0
DPP21_ne_500_r_0.22	0.034	0.039	16.0
DPP42_ne_500_r_0.14	0.032	0.038	19.4
DPP30_ne_500_r_0.18	0.013	0.018	45.2
DPP39_ne_500_r_0.18	0.010	0.016	61.2

Table 6-2 Optimisation data for the top-ten canonical forms.

The optimisation procedure has been far less effective with these canonical forms than it was with the brute force approach. Four of the ten optimisations resulted in very little noticeable improvement, less than ± 5%. Three canonical forms showed a significant degradation in the size of band gap with it being reduced by approximately a third in size in each case. However, there were two meshes, DPP27 and DPS11 that did show a large improvement of 132% and 159% respectively.

Further data for the three photonic crystal configurations exhibiting the largest band gaps can be

seen in Figure 6-12, Figure 6-10 and Figure 6-12 respectively. The 'pre' and 'post' optimisation density of states diagrams are compared. The convergence of the optimisation procedure is shown by plotting the band gap to mid gap ratio against the number of iterations of the optimisation loop. Finally the 'pre' and 'post' optimisation crystal meshes are shown so for comparison.

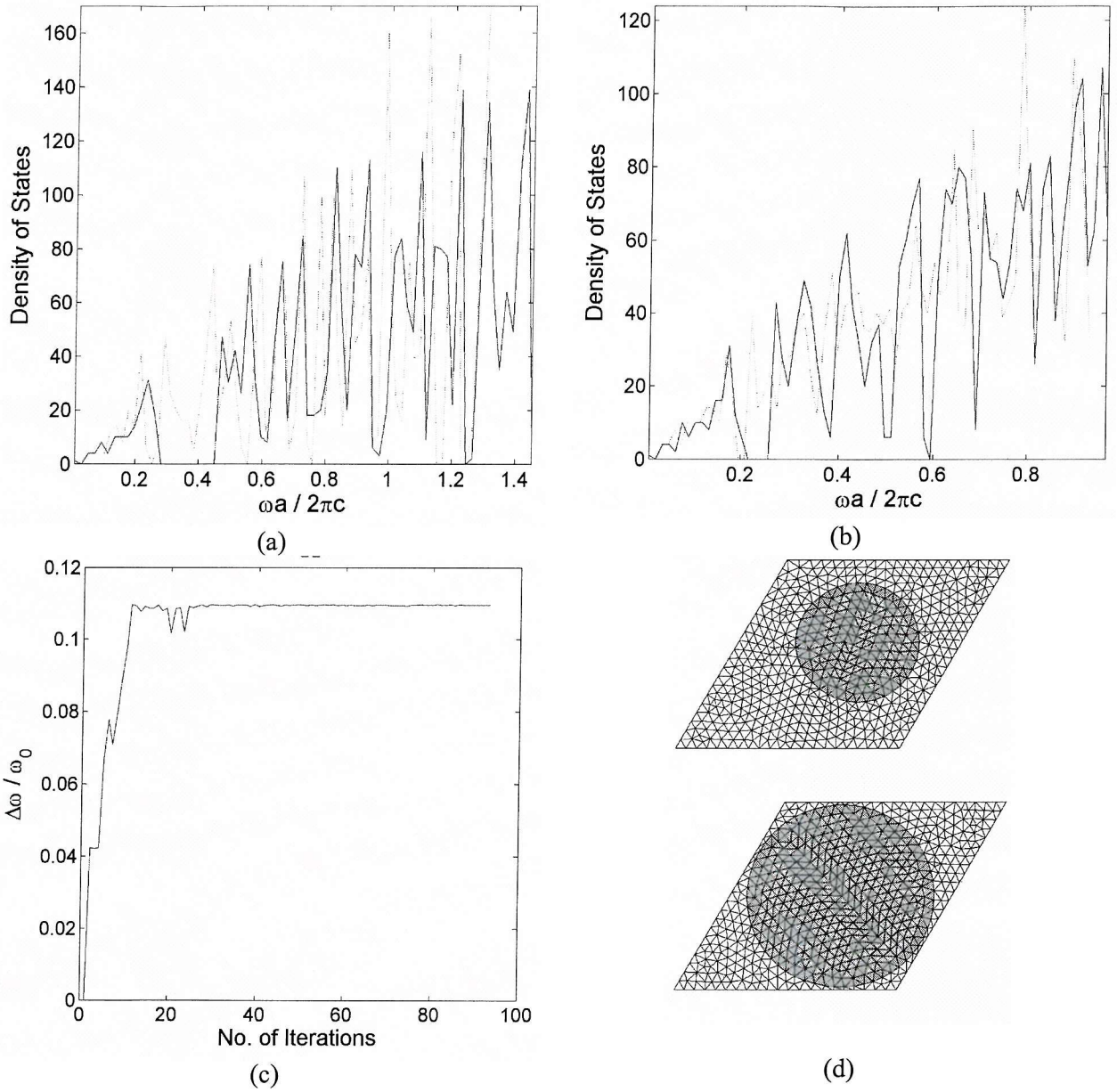

Figure 6-10 Optimisation data for canonical from DPS11. The density of states is plotted for the crystal before optimisation (a) and after optimisation (b). The convergence of the minimisation algorithm is shown by plotting the band-gap to mid-gap ratio against the number of iterations (c). The initial (above) and final (below) meshes are shown in (d).

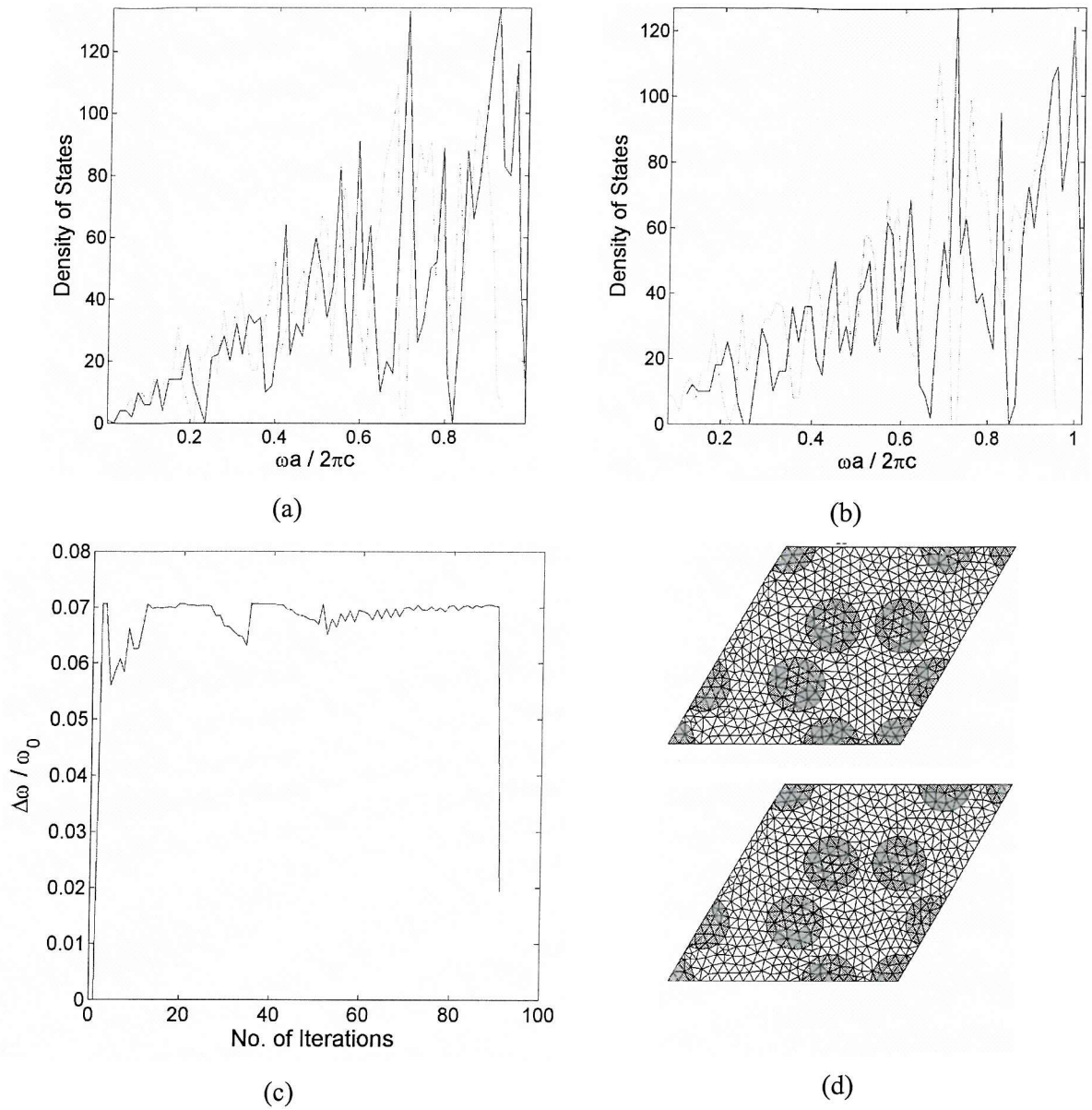

Figure 6-11 Optimisation data for canonical from DPP47. The density of states is plotted for the crystal before optimisation (a) and after optimisation (b). The convergence of the minimisation algorithm is shown by plotting the band-gap to mid-gap ratio against the number of iterations (c). The initial (above) and final (below) meshes are shown in (d).

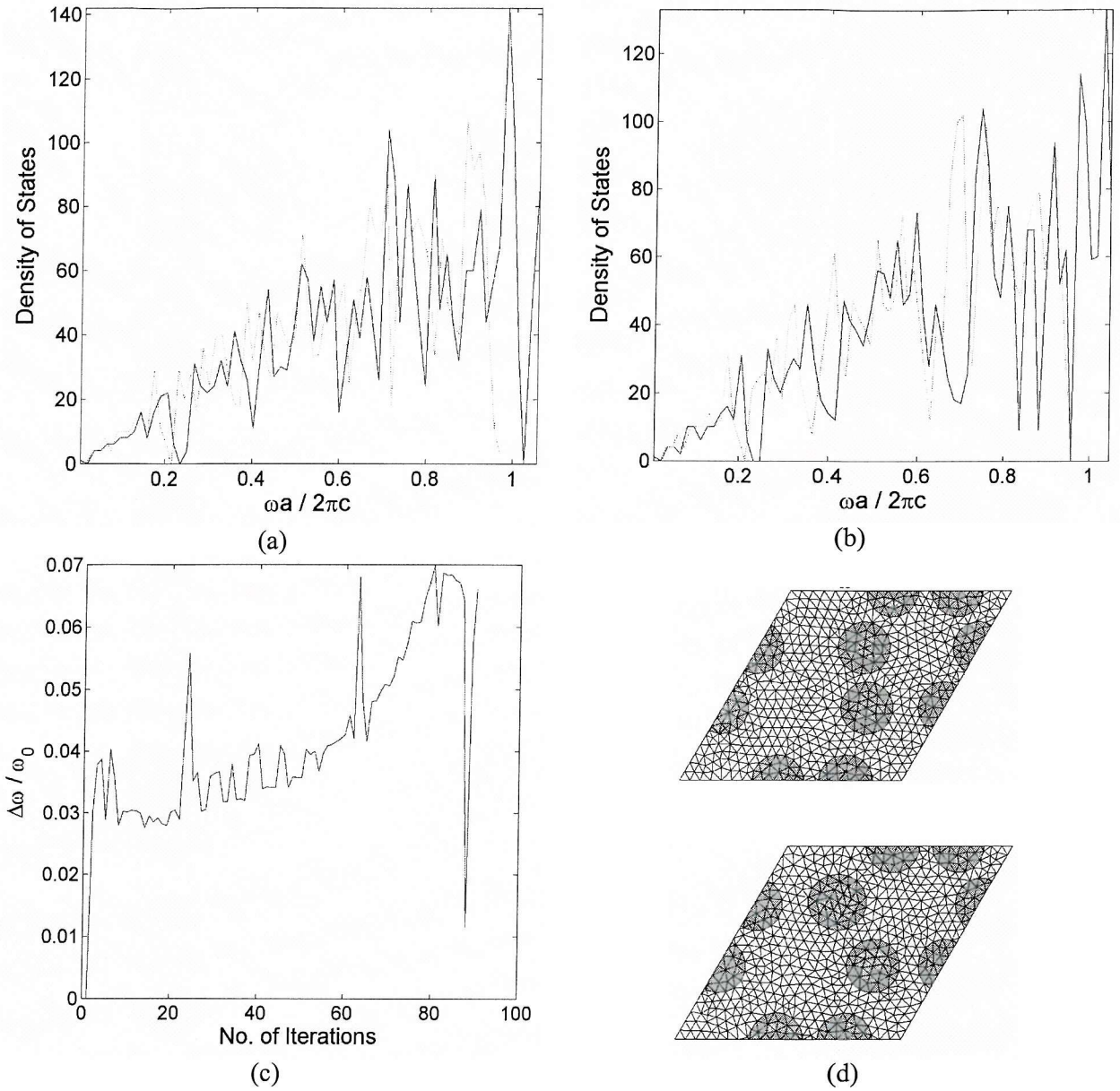

Figure 6-12 Optimisation data for canonical from DPP27. The density of states is plotted for the crystal before optimisation (a) and after optimisation (b). The convergence of the minimisation algorithm is shown by plotting the band-gap to mid-gap ratio against the number of iterations (c). The initial (above) and final (below) meshes are shown in (d).

DPP44 and DPP27 are similar in their geometry therefore it is unsurprising that they exhibit a similar band structure with a similar sized photonic band gap. DPS11 is effectively the triangular lattice as investigated in chapter 3.2. The band gap to mid gap ratio of this structure at 0.110 is approximately 60% larger than the other two canonical forms. Thus we can conclude that the straightforward triangular lattice exhibits a far superior band gap than all the other more exotic canonical form structures. Referring back to chapter 3, the reasons for this are that complete photonic band gaps favour crystal structures in which there are areas of high dielectric constant connected by narrow regions of dielectric.

6.6 Optimisation for a Homogeneous Filling Fraction

Collating the data produced from the optimisation research into groups of meshes with equal filling fractions (Table 6-3) allows one to see which geometries produce the largest band-gaps independently of the filling fraction.

Mesh No.	No. of Rods	Rod Radius	$\Delta\omega/\omega 0$	Filling Fraction
70	7	0.5	0.0108	0.4558
26	7	0.5	0.0097	0.4558
43	7	0.5	0.0096	0.4558
36	7	0.5	0.0091	0.4558
90	7	0.5	0.0075	0.4558
92	7	0.5	0.0071	0.4558
60	7	0.5	0.0062	0.4558
88	4	0.7	0.0279	0.5105
60	4	0.7	0.0272	0.5105
7	4	0.7	0.0235	0.5105
58	4	0.7	0.0228	0.5105
5	4	0.7	0.0200	0.5105
54	4	0.7	0.0167	0.5105
52	4	0.7	0.0165	0.5105
6	4	0.7	0.0106	0.5105
3	4	0.7	0.0092	0.5105
1	4	0.8	0.0630	0.6668
6	4	0.8	0.0417	0.6668
4	4	0.8	0.0328	0.6668
5	4	0.8	0.0281	0.6668
3	4	0.8	0.0158	0.6668
2	4	0.8	0.0125	0.6668

Table 6-3 The set of randomly generated meshes that exhibit a photonic band gap grouped into those of equal filling fraction.

Clearly, as the filling fraction increases, the mean band gap to mid-gap ratio also increases. If we look at the top three meshes for each filling fraction as presented in Table 6-3 then we can also see that as the filling fraction and therefore the band-gap sizes increase, we do indeed see a convergence towards the geometry of the triangular lattice. This is shown in Figure 6-13, Figure 6-14 and Figure 6-15. Looking back at the optimised meshes exhibiting the largest photonic band-gaps (Figure 6-5 - Figure 6-7) it is clear that they are all examples of the triangular lattice with a high-filling fraction.

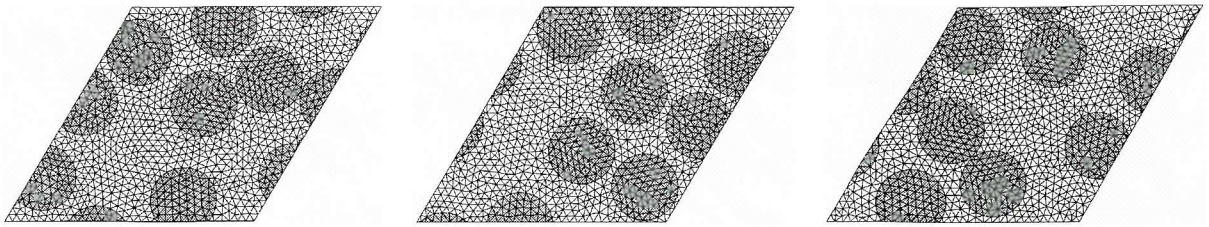

(a) (b) (c)

Figure 6-13 The three meshes exhibiting the largest band gaps for 4 rods in a rhombic unit cell with a filling fraction of 0.46; (a) mesh 70: $\Delta\omega/\omega 0 = 0.0108$, (b) mesh 26: $\Delta\omega/\omega 0 = 0.0097$, (c) 43: $\Delta\omega/\omega 0 = 0.0096$.

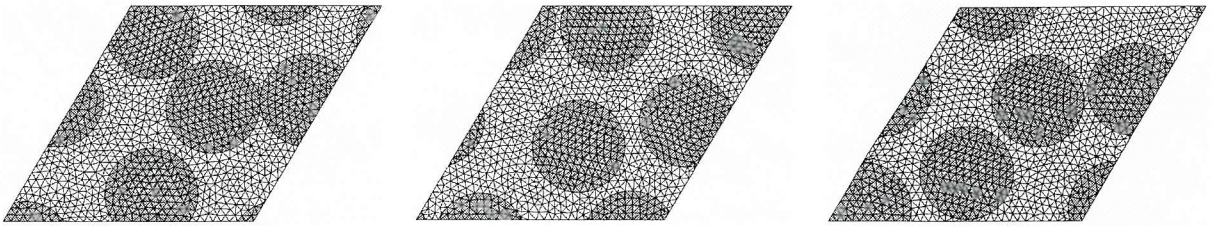

(a) (b) (c)

Figure 6-14 The three meshes exhibiting the largest band gaps for 4 rods in a rhombic unit cell with a filling fraction of 0.51; (a) mesh 88: $\Delta\omega/\omega 0 = 0.0279$, (b) mesh 60: $\Delta\omega/\omega 0 = 0.0272$, (c) 7: $\Delta\omega/\omega 0 = 0.0235$.

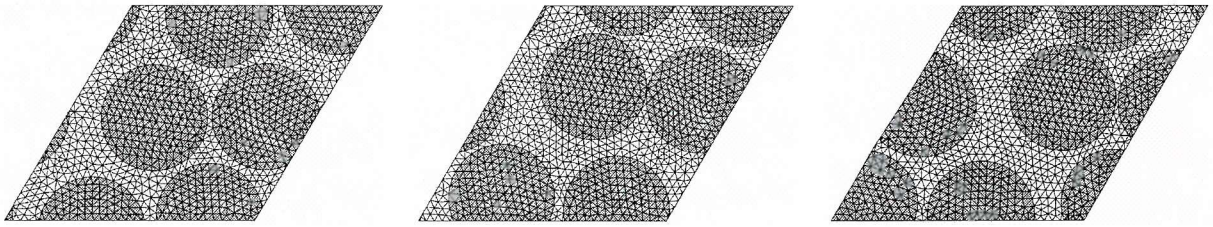

(a) (b) (c)

Figure 6-15 The three meshes exhibiting the largest band gaps for 7 rods in a rhombic unit cell with a filling fraction of 0.67; (a) mesh 1: $\Delta\omega/\omega 0 = 0.0630$, (b) mesh 6: $\Delta\omega/\omega 0 = 0.0417$, (c) 4: $\Delta\omega/\omega 0 = 0.0328$.

6.7 Conclusion

The brute-force and canonical form approaches to photonic crystal design optimisation has highlighted a number of clear trends. First and foremost is that the probability of a certain crystal geometry exhibiting a band-gap increases with the filling fraction. Secondly, the triangular lattice arrangement of rods is still the most successful design when trying to maximise the size of the band-gap. These two points are closely related as if one is to achieve a filling fraction in excess of 78.5% (the maximum filling fraction for a square lattice) then the geometry has to be that of a triangular lattice or at least a very close approximation. The optimum structures produced by the brute force approach and the canonical form approach both

converged to that of the triangular lattice with a relatively high filling fraction. Considering crystal geometries with a homogeneous filling fraction further reinforces this heuristic with the most successful crystal lattices as presented in chapter 6.6 all tending towards the triangular lattice geometry.

7 Conclusion

7.1 Summary

This thesis investigates the application of finite element methods to the modelling of photonic band gap devices. Their physical properties and potential applications are discussed along with the motivation for developing software capable of modelling these devices. The underlying physics governing the propagation of light through these crystal structures is presented and the process of applying the finite element method to the set of governing equations has been shown in detail. The differences between the two-dimensional and three-dimensional models are highlighted and the necessary modifications to the finite element method are explained.

The primary contribution of this work is the library of finite element code and associated optimised eigenvalue solvers. Unlike other computational electromagnetic software packages, this library has been created specifically for the analysis of photonic band gap devices. This has allowed many problem specific optimisations to be incorporated into the design resulting in an accurate and efficient numerical method.

The secondary contribution of this work has been to utilise the library of finite element software. We have studied the effect that fabrication tolerances have on the band structure of photonic crystals and the design optimisation of photonic crystal structures in order to maximise the size of their photonic band gap. Further work has also been carried out including investigation of the properties of a number of commonly modelled photonic crystal structures, along with more exotic, novel structures such as the twelve fold symmetric quasicrystal. The performance of the finite element code is investigated; the accuracy and convergence is examined along with the computation and memory requirements.

As explained in chapter 1.1, a photonic band gap device excludes photons of certain energies, in other words, the propagation of a certain electromagnetic frequency range is prohibited. This phenomena arises due to Bragg like diffraction caused by the structure of the photonic crystal, typically a periodic structure composed of two dielectric materials of different permittivity. This photonic band gap can be thought of as the luminary analogue of the electronic band-gap found in semiconductors.

One has only to consider the impact of semiconductors in the field of electronic engineering to

appreciate the interest that photonic band gap materials generate in the field of optical engineering. Perceived applications for photonic band gap devices include sharp angle wave-guides, highly efficient single mode lasers, integrated optical circuits and high-speed optical communication networks.

Photonic crystals must have a feature size comparable to the wavelength light they are designed to work with. Therefore if a photonic crystal with a band gap in the spectrum of visible light is required the feature size must be of the order of approximately 100 nm. Accurately fabricating these devices on such a small scale is very costly; therefore software capable of accurately and efficiently modelling the behaviour of these crystals is highly desirable.

Modelling the propagation of light involves solving Maxwell's equations given the correct boundary conditions. The specific application to wave propagation through a photonic crystal allows the equations to be refined to give the governing equation as shown in equation (2.6). As we are dealing with a crystal structure, e.g. one that varies periodically through space, we must apply periodic boundary conditions to the governing differential equation. For all but very simple scenarios, such as wave propagation through free-space, one cannot solve the governing equation analytically; thus a numerical method is needed to approximate the true solution. It has been the focus of this research to use finite elements as this numerical method.

The finite element method is based upon a straightforward 'divide and conquer' approach; divide the problem domain into a finite number of sub-domains of simple geometry. Approximate the solution over each of these sub-domains. These approximations are usually based on simple polynomial functions, their coefficients being the unknown variables. These approximations are integrated numerically to give the local elemental matrices. The local matrices are assembled according to the finite element topology to yield the global system of equations. Solving this system of equations gives the unknown parameters corresponding to the approximate solution of the problem. Thus repeatedly performing a number of simple calculations on small portions of the problem and then combining those results gives the solution to a complex problem. Computers are ideal for performing large numbers of simple calculations, hence the wide spread use of finite element software.

In the case of photonic crystal modelling, the governing differential equation is posed as an eigenvalue problem. Allowable electromagnetic modes satisfy the condition that the double curl operation on $\mathbf{H}(\mathbf{r})$ is equal to the product of $\mathbf{H}(\mathbf{r})$ and a scalar constant. When this is true, $\mathbf{H}(\mathbf{r})$

is an eigenvector representing the magnetic field pattern of an allowable mode and the scalar constant is an eigenvalue proportional to the squared frequency of that mode. The finite element method discretises and approximates this eigenvalue problem such that the problem is represented by matrices, equation (2.17), which can be solved using our optimised eigenvalue solver.

Prior to applying the finite element method the crystal structure must be discretised into simplex elements (triangles in 2D, tetrahedra in 3D). As crystals are periodic structures we need only consider the unit-cell, e.g. the area bound by the crystal lattice vectors. Periodic boundary conditions mean that opposing vertices on the boundary of the unit cell effectively represent the same vertex and therefore must meet if the mesh were wrapped on to a torus. A number of public domain third party meshing algorithms were used for this purpose, predominantly Geompack90 but also other packages such as Easymesh, Netgen and Triangle (see chapter 2.1). The output format of these packages varied but the common core information of interest included the coordinates of the element vertices, the topology of the elements and material markers for the elements. These are later used to specify the electrical permittivity of the individual elements.

When formulating the elemental equations, it is necessary to select a suitable interpolation function. This describes how the solution can vary over an element. This is one way in which the quality of the solution can be controlled. In our FE code the end-user can specify a polynomial interpolation function of any order. Using a simple interpolation function leads to small elemental matrices but a coarse representation, a more complex interpolation function generates larger elemental matrices but gives a finer solution. The optimum balance between computational cost and quality of solution with respect to interpolation function complexity was analysed in chapter 4.2 with the conclusion being that 2^{nd} order interpolation functions produced the best performance with 1^{st} order interpolation producing the worst performance by a significant margin.

In order to generate the elemental matrices, elemental equations are derived as a function of the chosen interpolation order and the governing differential equation and boundary conditions. Deriving these equations involves enforcing the periodic boundary conditions on the differential equation. This is done via the application of Floquet-Bloch theory (Kuchment 1993). The differential equation is then formulated in variational weak integral form and approximated using a weighted residual (Galerkin's) method leaving an equation consisting of integrals that

can be computed numerically.

Using mesh data as input, the elemental matrices are computed and subsequently assembled according to the mesh topology. This generates the global matrices that constitute the generalised eigenvalue problem. This eigensystem is then solved using our eigenvalue solver. The resulting eigenvalues correspond to the frequency of the allowable modes of propagation. The corresponding eigenvectors describe the field intensity over the crystal for those modes.

An optimised eigenvalue solver was developed using a subspace iterative technique (Beckett 2002). This method allows a number of simple but effective optimisations to be made. For example, only the physically relevant eigenvalues are computed; typically the pertinent information is contained in the lowest 10 eigenvalues and the vast majority need not be found. Also, when computing the band structure of a photonic crystal a series of similar eigensystems needs to be solved for adjacent **k** vectors. The similarity in the solution for eigensystems with similar **k** vectors can be exploited by feeding in the solution of one eigensystem as the initial guess for the subspace search of the next system. This significantly reduces the number of iterations required for convergence. The subspace iteration converges rapidly to the most dominant eigenvectors in the subspace but struggles to find the least dominant ones. This difficulty in converging to the last components can be avoided by searching a slightly larger subspace and neglecting to find the final, difficult, eigenvectors.

Traditionally, plane wave techniques have been applied to photonic crystal modelling. These have the disadvantages of being slow to converge. They are also computationally and memory intensive. The motivation for applying finite element techniques to the computation of photonic crystal spectra is to allow for flexible, efficient and accurate modelling of crystal structures. Flexibility is provided by the use of a discrete mesh to model the PC structure. Many public domain and commercial packages are available for producing quality meshes making it relatively easy to generate the mesh representations of the photonic crystal structures. This approach also has the advantage of providing an intuitive, real-space representation of the geometry that is easy to work with. Additionally, the meshes allow the sharp discontinuities in dielectric constant inherent in PBG materials to be modelled accurately.

As a direct consequence of the node connectivity of the mesh, the resulting assembled system of equations governing the propagation of light through the PC is very sparse. This results in computation and memory costs of order $O(n)$, e.g. the complexity scales linearly with problem

size. This is opposed to $O(n^d)$ scaling for the plane wave method, where d is the dimensionality of the problem domain. It is this fundamental difference in the way that the method scales that opens up the possibility of modelling complex two-dimensional and even three-dimensional PC structures.

The FEM code has been developed to compute the modes of propagation for two-dimensional and three-dimensional input meshes. In order to test the validity of the results produced by the finite element code a finite element analysis of free-space was computed and compared with the corresponding analytical solution. The results showed excellent agreement with the true solution. Common photonic crystal structures have been modelled including square and triangular lattice arrangements of rods and the 'woodpile' structure. The computed band diagrams agree with those found elsewhere in the literature. The results of our investigation into commonly modelled photonic crystal structures gives further evidence that crystal structures with disconnected areas of high dielectric constant favour band gaps in the TM mode polarisation and crystal structures with connected areas of high dielectric constant favour band gaps in the TE mode polarisation. A complete photonic band gap, where there is a frequency range for which both polarisations are excluded, is exhibited for a crystal structure that combines both of these characteristics. At a first glance it seems the first structural criteria excludes the second and vice versa, however, a compromise between the two in which a structure has areas of high dielectric constant connected by narrow veins can partially satisfy both criteria and such a structure can exhibit a complete photonic band gap. The obvious example of this is the triangular lattice of air rods in a high dielectric substrate.

The performance of the two-dimensional algorithm has been tested with respect to mesh granularity and interpolation order. The results confirm the linear scaling with problem size in memory requirements and computation time. It was also clear that higher order interpolation functions (2^{nd}, 3^{rd} and 4^{th}) gave a better solution accuracy for a given computation time than 1^{st} order.

The novel twelve-fold symmetric quasi-crystal has also been modelled. It has been suggested that this structure has a complete band-gap for very low contrasts in dielectric constant and its high order of rotational symmetry favours the opening of photonic band gaps and also gives the structure very similar propagation characteristics for all angles of incidence. The computed band diagrams for these structures do exhibit band gaps but not for materials of low dielectric contrast, e.g. silicon nitride and glass.

The extension of the code from two to three dimensions requires a significantly different numerical approach. Naïvely incorporating an additional coordinate into the interpolation functions leads to incorrect continuity of fields at dielectric boundaries. This results in the generation of incorrect (spurious) solutions. The implementation of edge-based elements and vector basis functions addresses the problem of divergent solutions and incorrect continuity of fields at dielectric boundaries. This approach uses vector based interpolation functions along each edge such that the tangential component of the field is zero at all element boundaries except one. At this boundary, the tangential component is defined solely by the shape and orientation of that boundary. This approach ensures the desired continuity of tangential component of the field but allows the normal component to be discontinuous. This alternative formulation of the elemental interpolation functions coupled with the full vector form of Maxwell's equations leads to the derivation of completely different elemental equations. However, the key advantages of the FEM remain, e.g. the simple mesh-based input and the resulting sparse eigenvalue matrices.

Whilst we did not produce a fully working version of the three-dimensional vector finite element code. Significant progress towards this goal was made. A front-end capable of reading several popular public-domain meshing algorithm formats was developed, along with the ability to enforce periodic boundary conditions by wrapping opposing external nodes. The correct computation of the Dirichlet, **S**, and metric, **T**, matrices was completed allowing the eigenvalues to be computed at the gamma-point in reciprocal lattice space. Unfortunately, bugs remain in the generation of the **P** and **J** elemental matrices, and when computing the global matrices for **k**-vectors other than the gamma-point.

The decision was taken to halt further development of the vector FE code as the debugging process was taking far longer than expected. The effort was redirected towards using the existing scalar FE code to explore photonic crystal design optimisation and the effect of fabrication tolerances on the band structure of photonic crystals. The recent availability of commercial vector finite element software packages for computational electromagnetics targeted at photonic device modelling further strengthened this decision.

The problem of spurious mode pollution of the eigenspectrum is still present, although the vector FEM can identify the spurious modes correctly (those with a zero eigenvalue) there are still many of these modes present in the spectrum, exactly one for every non-boundary node in

the mesh. Therefore computing the pertinent eigenvalues also requires the computation of many redundant spurious solutions. This puts a penalty on the computation that is proportional to the number of non-boundary nodes in the mesh. This is clearly a highly undesirable situation. The development of a new eigenvalue solver based on the Lanczos method has eliminated the need to compute these spurious modes when trying to generate the eigenvalues of interest corresponding to real physical solutions.

A number of papers have presented theoretical photonic crystal geometries and subsequently computed their band structures. It is often the case that these structures bear little resemblance to what is actually possible to fabricate. For example, it is well known that crystal structures with a high filling fraction are likely to produce large band gaps, however, this can result in very thin areas of substrate material which would be vulnerable to collapsing when fabricated thus destroying the crystal structure. We investigated the effect of fabrication tolerances on the resulting band structure of PBG devices as this has an important bearing upon how one interprets the results from the various numerical models with regard to actually fabricating these devices.

It was surprising just how significant the fabrication tolerance was with respect to the band structure of the PBG device. A relative error of 5% in the rod radius led to a probability that the fabricated device would exhibit a band gap of only 0.42; the corresponding probability for a relative error of 1% is 0.99. Hence a reduction in the relative error of 4% increases the probability of a band gap existing by 50%. This confirms the fact that it is technically difficult to fabricate PBG devices that operate in the visible spectrum. Clearly, current fabrication techniques need to be refined or new techniques developed that can provide the lower tolerances necessary to achieve a reasonable probability of creating a PBG device with a band structure equivalent to that of its numerically modelled counterpart.

Using the finite element method over traditionally used plane wave expansion techniques reduces the computational cost and memory requirements for photonic crystal modelling. This makes the application of photonic crystal design optimisation a feasible proposition. The FE code has been successfully combined with additional software components to create an optimisation tool that attempts to produce a photonic crystal structure that has a photonic band gap of the maximum frequency range. Further benefits of an optimisation tool are that it allows the end user to generate materials with photonic band gaps engineered as required and also alleviates the user from having to produce mesh representations of the crystal structures. The

desired structure is output and then fabricated. This required the creation of additional software modules to be used in conjunction with the finite element code (see chapter 6). An automated mesh generation tool was built to convert a high-level description of the crystal structure into a low-level description that can be understood by the third party public domain meshing software. It also has to enforce the periodic boundary conditions upon the mesh, e.g. if any feature overlaps a unit cell boundary it must be re-mapped on to the opposing boundary (see chapter 6.1). A post-processing tool was also built to analyse the set of eigenvalues produced by the FE code and detect the presence and size of any band gaps.

One component of the optimisation software is the minimisation algorithm. The chosen algorithm was first proposed by (Nelder and Mead 1965) and is known as the downhill simplex method. While it is not the most efficient minimisation algorithm available it is relatively simple to implement and can also deal with multiple optimisation parameters. This was a vital consideration as our input parameters are essentially the geometric description of the crystal structure, each rod radii and position is a separate parameter. The minimisation algorithm aims to minimise the reciprocal of the band gap to mid gap ratio and that maximises the band gap size, hence the computation of the objective function requires the combination of the automated mesh generator, the FE code and the eigenvalue analysis code. The function input is the crystal structure description (see Figure 6-1) and the output is the band gap to mid gap ratio. The optimisation procedure involves repeatedly running the FE code, each time with a hopefully superior crystal structure. This is clearly a computationally intensive task hence the optimisation code was executed on various dedicated commodity cluster computers capable of performing the volume of computation within a reasonable time-scale.

The research into photonic crystal optimisation for both the brute force and canonical form approach has consolidated the conclusions drawn in chapter 3. Namely that the necessary characteristics of a photonic crystal exhibiting a complete photonic band gap are areas of high dielectric constant connected by narrow veins of substrate material. The investigation into many thousands of different photonic crystal structures has not produced band gaps any better than those exhibited by the common triangular lattice, in fact, the largest band-gap we computed had a gap to mid-gap ratio, $\Delta\omega/\omega_0$, of 0.19. This was exhibited by a triangular lattice of air rods in a GaAs substrate with a rod to pitch length ratio, r/a , of 0.48. The formula is simple – large dielectric contrast plus a high filling fraction equals a large photonic band gap. For a two-dimensional crystal the arrangement of rods that allows the highest filling fraction is the triangular lattice, hence it is not surprising that this structure provides the largest photonic band

gap.

7.2 Future Work

The difficulty in implementing the 3D vector based FE code has left scope for further work to take place in the investigation of fully three-dimensional structures. The formulation of the elemental equations for the three-dimensional vector finite elements is significantly more difficult than the two-dimensional case and as a result we have not generated correct eigenvalues for **k** vectors other than the gamma point. It would be of interest to compare the 3D analogues of the 2D structures so that the resulting density of states and dispersion relations can be compared. In addition, more interesting structures that are fully periodic in 3 dimensions could be investigated.

The construction of three-dimensional meshes is significantly more difficult than those in two-dimensions, hence the development of an easy to use front end in which one can specify common geometries at a high level of abstraction, as has been built for two-dimensional meshes, would be a very useful. It is common in the field of finite element modelling that the majority of time taken to perform a simulation is spent in the production of a quality input mesh. An intuitive and easy to use front-end to a three dimensional meshing package would save considerable time for the end user of the software.

The implementation of a more sophisticated minimisation algorithm as a basis for the optimisation process may well lead to performance gains in this area. There are two other main families of algorithms for multi-dimensional minimisation that could be investigated; these are the conjugate gradient methods (Polak 1971) and the variable metric methods (Gill, Murray et al. 1981). The optimisation code could also be coupled to commercially available photonic device design codes as these currently provide only limited optimisation features.

References

Ansoft (2002). Ansoft Corporation. http://www.ansoft.com.

Axmann, W. and P. Kuchment (1999). "An efficient finite element method for computing spectra of photonic and acoustic band-gap materials - I. Scalar case." Journal of Computational Physics **150**(2): 468-481.

Axmann, W., P. Kuchment, et al. (1999). "Asymptotic methods for thin high-contrast two-dimensional PBG materials." Journal of Lightwave Technology **17**(11): 1996-2007.

BandSOLVE (2002). RSoft Design Group. New York. http://www.rsoftdesign.com/products/component_design/BandSOLVE/.

Bathe, K. J. and E. L. Wilson (1976). Numerical Methods in Finite Element Analysis. New Jersey, Prentice Hall Inc.

BeamPROP (2002). RSoft Design Group. New York. http://www.rsoftdesign.com/products/component_design/BeamPROP/.

Beckett, D. H. (2002). Calculating Eigenvalues: Algorithms and Applications. Department of Electronics and Computer Science. Southampton, Univeristy of Southampton.

Beowulf (2002). The Beowulf Project. http://www.beowulf.org/.

Bossavit, A. and J. C. Verite (1982). "A Mixed FEM-BEM Method to Solve 3-D Eddy-Current Problems." Ieee Transactions on Magnetics **18**(2): 431-435.

Calvetti, D., L. Reichel, et al. (1994). "An Implicitly Restarted Lanczos Method for Large Symmetric Eigenvalue Problems." Electronic Transactions on Numerical Analysis **2**: 1-21.

Campbell, M., D. N. Sharp, et al. (2000). "Fabrication of photonic crystals for the visible spectrum by holographic lithography." Nature **404**: 53-56.

Charlton, M. D. B. and G. J. Parker (1998). "Nanofabrication of advanced waveguide structures incorporating a visible photonic band gap." Journal of Micromechanics and Microengineering **8**(2): 172-176.

Charlton, M. D. B., G. J. Parker, et al. (1999). "Recent developments in the design and fabrication of visible photonic band gap waveguide devices." Journal of Materials Science-Materials in Electronics **10**(5-6): 429-440.

Charlton, M. D. B., M. E. Zoorob, et al. (2000). "Experimental investigation of photonic crystal waveguide devices and line-defect waveguide bends." Materials Science and Engineering B-Solid State Materials for Advanced Technology **74**(1-3): 17-24.

Comsol (2002). Femlab. www.femlab.com.

Condor (2002). Condor: High Throughput Computing. Wisconsin, University of Wisconsin. http://www.cs.wisc.edu/condor/.

Csendes, Z. J. and S. H. Wong (1987). "C^1 Quadratic Interpolation over Arbitrary Point Sets." IEEE Comp. Graphics Appl. **7**: 8-16.

Dobson, D. C. (1999). "An Efficient Method for Band Structure Calculations in 2D Photonic Crystals." Journal of Computational Physics **149**(2): 363-376.

EASY (2002). EASY Job Scheduler. University of Southampton, Computing Services. http://www.soton.ac.uk/~sucsweb/Research/Easy/.

Fagan, M. J. (1992). Finite Element Analysis Theory and Practice. Essex, Addison Wesley Longman Ltd.

FullWAVE (2002). RSoft Design Group. New York. http://www.rsoftdesign.com/products/component_design/FullWAVE/.

Gill, P. E., W. Murray, et al. (1981). Practical Optimization. New York, Academic Press.

Golub, G. H. and C. F. Van Loan (1996). Matrix Computations. Baltimore, John Hopkins University Press.

Grünbaum, B. and G. C. Shephard (1987). Tilings and Patterns. New York, W. H. Freeman and Company.

Halliday, D., R. Resnick, et al. (1992). Physics. New York, John Wiley & Sons.

Iridis (2002). Iridis: Linux Beowulf Cluster, University of Southampton Computing Services. http://www.sucs.soton.ac.uk/research/iridis/.

Jennings, A. (1977). Matrix Computation for Engineers and Scientists. London, New York, Wiley.

Jin, J. (1993). The Finite Element Method in Electromagnetics. New York, Wiley.

Joannopoulos, J. D., R. D. Meade, et al. (1995). Photonic Crystals: Molding the Flow of Light. New Jersey, Princeton University Press.

Joe, B. (2001). Geompack mesh generating software. www.netcom.ca/~bjoe/index.htm.

Kittel, C. (1986). Introduction to Solid State Physics. New York, John Wiley & Sons, Inc.

Kuchment, P. (1993). Floquet theory for partial differential equations. P.O. Box 133, CH-4010 Basel, Switzerland, Birkhauser Verlag.

Lutz, M. (1996). Programming Python. 101 Morris Street, Sebastapol, CA 95472, O'Reilly & Associates, Inc.

MAUI (2002). MAUI Job Scheduler. http://supercluster.org/projects/maui/index.html.

Molinari, M., S. J. Cox, et al. (2001). "Adaptive mesh refinement techniques for electrical impedance tomography." Physiological Measurement **22**(1): 91-96.

Nedelec, J. C. (1986). "Mixed Finite-Element in 3d in H(Div) and H(Curl)." Lecture Notes in Mathematics **1192**: 321-325.

Nedelec, J. C. (1986). "A New Family of Mixed Finite-Elements in R3." Numerische Mathematik **50**(1): 57-81.

Nelder, J. A. and R. Mead (1965). "The Downhill Simplex Method." Computer Journal **7**: 308-

313.

Netti, M. C., M. D. B. Charlton, et al. (2000). "Visible photonic band gap engineering in silicon nitride waveguides." Applied Physics Letters **76**(8): 991-993.

Newman, M. E. J. and G. T. Barkema (1999). Monte Carlo Methods in Statistical Physics. New York, Oxford University Press.

Niceneco, B. (2000). Easymesh quality mesh generator. http://www-dinma.univ.Trieste.it/~nirftc/research/easymesh.

Parker, G. and M. Charlton (2000). "Photonic crystals." Physics World **13**(8): 29-34.

Pissanetsky (1984). Sparse Matrix Technology. London, Academic Press Inc.

Polak, E. (1971). Computational Methods in Optimization. New York, Academic Press.

Press, W. H., S. A. Teukolsky, et al. (1999). Numerical Recipes in Fortran 77 - The art of scientific computing, Cambrdige University Press.

Rahman, B. M. A., F. A. Fernandez, et al. (1991). "Review of finite element methods for microwave and optical waveguides." Proceedings IEEE **79**: 1442-1448.

Remski, R. (2000). "Analysis of photonic bandgap surfaces using Ansoft HFSS." Microwave Journal **43**(9): 190 -.

Salazar-Palma, M., T. K. Sarkar, et al. (1998). Iterative and self-adaptive finite-elements in electromagnetic modelling, Artech House, Inc.

Schöberl, J. (2001). NETGEN. http://www.sfb013.uni-linz.ac.at/~joachim/netgen/.

Sehmi, N. S. (1989). Large Order Structural Eigenanalysis Techniques. Chichester, Ellis Horwood.

Shewchuk, J. R. (1996). Triangle. http://www.cs.cmu.edu/~quake/triangle.html.

Silvester, P. P. and R. L. Ferrari (1996). Finite Elements for Electrical Engineers. Cambridge, University Press.

Stroustroup, B. (1997). The C++ Programming Language. Reading, Massachusetts, Addison-Wesley.

Sun, D., J. Manges, et al. (1995). "Spurious Modes in Finite-Element Methods." Ieee Antennas and Propagation Magazine **37**(5): 12-24.

Taflove, A. and S. C. Hagness (2000). Computational Electromagnetics: the finite-difference-time-domain method. Norwood, Artech House, Inc.

The MathWorks, I. (1999). Using Matlab. `http://www.mathworks.com/`.

Thompson, J. F., B. K. Soni, et al. (1999). Handbook of Grid Generation. Washington DC, CRC Press LLC.

VectorFields (2002). "Concerto."

Villeneuve, P. R. and M. Piche (1991). "Photonic Band-Gaps of Transverse-Electric Modes in 2- Dimensionally Periodic Media." Journal of the Optical Society of America a-Optics Image Science and Vision **8**(8): 1296-1305.

Villeneuve, P. R. and M. Piche (1994). "Photonic Bandgaps - What Is the Best Numerical Representation of Periodic Structures." Journal of Modern Optics **41**(2): 241-256.

Villeneuve, P. R. and M. Piche (1994). "Photonic Bandgaps in Periodic Dielectric Structures." Progress in Quantum Electronics **18**(2): 153-200.

Webb, J. P. (1993). "Edge Elements and What They Can Do for You." Ieee Transactions on Magnetics **29**(2): 1460-1465.

Webb, J. P. and B. Forghani (1993). "Hierarchical Scalar and Vector Tetrahedra." Ieee Transactions on Magnetics **29**(2): 1495-1498.

Wong, S. H. and Z. J. Csendes (1988). "Combined Finite Element-Modal Solution of Three-Dimensional Eddy Current Problems." IEEE Transactions on Magnetics **25**: 3019-3021.

Xiangdong, Z., Z. Zhao-Qing, et al. (2001). Absolute photonic band gaps in 12-fold symmetric photonic quasicrystals. Clear Water Bay, Kowloon, Hong Kong, China, Department of Physics, The Hong Kong Universoty of Science and Technology.

Yablonovitch, E. (1987). "Inhibited Spontaneous Emission in Solid-State Physics and

Electronics." Physical Review Letters **58**(20): 2059-2062.

Yablonovitch, E. (1993). "Photonic Band-Gap Structures." Journal of the Optical Society of America B-Optical Physics **10**(2): 283-295.

Yablonovitch, E. (1994). "Photonic Crystals." Journal of Modern Optics **41**(2): 173-194.

Yablonovitch, E. (2000). "Applied physics - How to be truly photonic." Science **289**(5479): 557-+.

Yablonovitch, E., T. J. Gmitter, et al. (1992). "3-Dimensional Photonic Band-Structure." Optical and Quantum Electronics **24**(2): S273-S283.

Zienkiewicz, R. L. and R. L. Taylor (1989). The Finite Element Method. New York, McGraw Hill.

Zoorob, M. E., M. D. B. Charlton, et al. (2000). "Complete and absolute photonic bandgaps in highly symmetric photonic quasicrystals embedded in low refractive index materials." Materials Science and Engineering B-Solid State Materials for Advanced Technology **74**(1-3): 168-174.

Zoorob, M. E., M. D. B. Charlton, et al. (2000). "Complete photonic bandgaps in 12-fold symmetric quasicrystals." Nature **404**(6779): 740-743.

Appendix A: Galerkin's Method

Boundary-value problems (BVP's) arise in the mathematical modelling of physical systems and their solution has long been a major topic in mathematical physics.

A BVP is typically defined by a governing differential equation in a domain Ω:

$$\Im\phi = f, \tag{A.1}$$

where: $\Im$ differential operator

ϕ unknown quantity

f forcing function

Together with boundary conditions on the boundary Γ that encloses the domain.

Galerkin's method approximates the true solution of a BVP. It is used for problems of practical importance that cannot be solved analytically. This is a weighted residual method, which seeks the solution by weighting the residual of the differential equation. Assume $\tilde{\phi}$ is an approximate solution to equation (A.1). Substitution of $\tilde{\phi}$ for ϕ in equation (A.1) results in a non-zero residual.

$$r = \Im\tilde{\phi} - f \neq 0. \tag{A.2}$$

The best approximation for $\tilde{\phi}$ is that which reduces the residual r to the least value at all points in the domain Ω. The weighted residual method enforces the condition

$$R_i = \int_\Omega w_i r \, d\Omega = 0. \tag{A.3}$$

R_i is the weighted residual integral and w_i is the weighting function. In Galerkin's method, the weighting function is chosen to be the same as the expansion of the approximate solution. Hence, if $\tilde{\phi}$ is approximated by the expansion

$$\tilde{\phi} = \sum_{j=1}^{N} c_j v_j \,, \tag{A.4}$$

where v_j are the expansion functions and c_j are the coefficients to be determined, then the weighting functions are selected as

$$w_i = v_i \qquad i = 1,2,3...,N \,. \tag{A.5}$$

Therefore equation (A.3) becomes

$$R_i = \int_\Omega \left(v_i \Im \sum_{j=1}^{N} c_j v_j - v_i f \right) d\Omega = 0 \qquad i = 1,2,3...,N \,. \tag{A.6}$$

This can be broken down into the form $\boldsymbol{Ax} = \boldsymbol{b}$ where

$$A_{ij} = \int_\Omega v_i \Im v_j \; d\Omega \,, \tag{A.7}$$

$$b_i = \int_\Omega v_i f \; d\Omega \,, \tag{A.8}$$

$$x_i = c_i \,. \tag{A.9}$$

This resulting expression can be solved as a simultaneous linear equation.

Appendix B: Simplex Elements

A simplex element in *N*-dimensions is defined as the minimal possible non-trivial geometric figure in that space having *N+1* vertices.

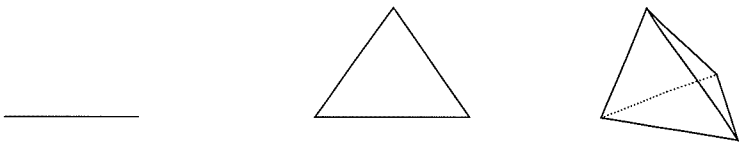

1-D Simplex *2-D Simplex* *3-D Simplex*

Figure B-1 N-*dimensional simplex elements.*

B.1 Simplex Coordinates

The position of any point P in a simplex element can be expressed in terms of simplex coordinates such that

$$\xi_m = \sigma(S_m)/\sigma(S), \tag{B.1}$$

where ξ is the simplex coordinate, $\sigma(S)$ is the size of the simplex and $\sigma(S_m)$ is the size of a sub-simplex, e.g. in Figure B-2, the simplex coordinate, ξ_1 of $P = \sigma(S_1)/\sigma(S)$.

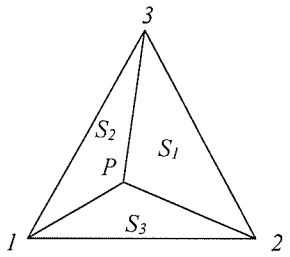

Figure B-2 Simplex coordinates.

The size of a simplex element is defined as

$$\sigma(S)=\frac{1}{N!}\begin{vmatrix}1 & x_1^{(1)} & x_1^{(2)} & \dots & x_1^{(N)}\\ 1 & x_2^{(1)} & & & \\ \vdots & & & & \\ 1 & x_{N+1}^{(1)} & x_{N+1}^{(2)} & \dots & x_{N+1}^{(N)}\end{vmatrix}, \tag{B.2}$$

Where N is the dimensionality of the simplex and the elements are the positions of the vertices. The subscripts denote the vertex number and the superscripts denote the spatial direction.

B.2 2-Dimensional Cartesian-Simplex Conversion

Using (2.5) global Cartesian coordinates can be converted to local simplex coordinates by calculating the determinant of the sub-simplex divided by the determinant of the simplex. For example, if a point P lies within a 2-simplex (triangle) with Cartesian coordinates *(x ,y)* the 1st simplex coordinate can be calculated as

$$\xi_1=\frac{\begin{vmatrix}1 & x & y\\ 1 & x_2 & y_2\\ 1 & x_3 & y_3\end{vmatrix}}{\begin{vmatrix}1 & x_1 & y_1\\ 1 & x_2 & y_2\\ 1 & x_3 & y_3\end{vmatrix}}, \tag{B.3}$$

expansion of the determinants for all three simplex coordinates gives the following conversion equation

$$\begin{bmatrix}\xi_1\\ \xi_2\\ \xi_3\end{bmatrix}=\frac{1}{2A}\begin{bmatrix}x_2y_3-x_3y_2 & y_2-y_3 & x_3-x_2\\ x_3y_1-x_1y_3 & y_3-y_1 & x_1-x_3\\ x_1x_2-x_2y_1 & y_1-y_2 & x_2-x_1\end{bmatrix}\cdot\begin{bmatrix}1\\ x\\ y\end{bmatrix}, \tag{B.4}$$

where each simplex coordinate has the linear form $\xi_m=a_m+b_mx+c_my$. A represents the area of the simplex and can be computed using equation (B.2).

B.3 3-Dimensional Cartesian-Simplex Conversion

$$\begin{bmatrix}\xi_1\\ \xi_2\\ \xi_3\\ \xi_4\end{bmatrix}=\frac{1}{6V}\begin{bmatrix}a_1 & a_2 & a_3 & a_4\\ b_1 & b_2 & b_3 & b_4\\ c_1 & c_2 & c_3 & c_4\\ d_1 & d_2 & d_3 & d_4\end{bmatrix}\begin{bmatrix}1\\ x\\ y\\ z\end{bmatrix} \tag{B.5}$$

Where:

	1	*2*	*3*	*4*
a	*1*	*1*	*1*	*1*
b	x_1	x_2	x_3	x_4
c	y_1	y_2	y_3	y_4
d	z_1	z_2	z_3	z_4

Table B-1 3-dimensional simplex coordinate coefficients

In order to compute the coefficients, a_1, b_2, c_3, d_4, etc., using Table B-1, take the determinant of the remaining values after the relevant row and column have been excluded, e.g.

$$a_1=-1^{i+j}\times\begin{vmatrix}x_2 & x_3 & x_4\\ y_2 & y_3 & y_4\\ z_2 & z_3 & z_4\end{vmatrix} \tag{B.6}$$

$$b_2=-1^{i+j}\times\begin{vmatrix}1 & 1 & 1\\ y_1 & y_3 & y_4\\ z_1 & z_3 & z_4\end{vmatrix} \tag{B.7}$$

i and j represent the row and column number respectively. The volume is computed from the tetrahedral vertices as shown below

$$V=\frac{1}{6}\begin{vmatrix}1 & 1 & 1 & 1\\ x_1 & x_2 & x_3 & x_4\\ y_1 & y_2 & y_3 & y_4\\ z_1 & z_2 & z_3 & z_4\end{vmatrix}. \tag{B.8}$$

B.4 Differentiation in Simplex Coordinates

If the approximate solution across an element is represented as

$$\psi = \sum_{m=1}^{M} \psi_m \alpha_m \,. \tag{B.9}$$

The x directed partial derivative can be represented as

$$\frac{\partial \psi}{\partial x} = \sum_{m=1}^{M} \psi_{(x)m} \alpha_m \,. \tag{B.10}$$

Where $\psi_{(x)m}$ is the value of $\frac{\partial \psi}{\partial x}$ at interpolation node m. If the nodal values ψ_m are represented by the vector $\Psi = [\psi_1, \psi_2 ... \psi_M]^T$, and the nodal values $\psi_{(x)m}$ similarly represented as $\Psi_{(x)} = [\psi_{(x)1}, \psi_{(x)2} ... \psi_{(x)M}]^T$ then the differentiation operator $\partial/\partial x$ can be replaced by a matrix $\mathbf{D}$ such that $\Psi_{(x)} = \mathbf{D}_{(x)} \Psi$.

It remains to calculate the matrix $\mathbf{D}$. This is performed via the following steps. Starting with the formal differentiation

$$\frac{\partial \psi}{\partial x} = \sum_{m=1}^{M} \psi_m \frac{\partial \alpha_m}{\partial x} \tag{B.11}$$

the derivative on the right can be rewritten as

$$\frac{\partial \alpha_m}{\partial x} = \sum_{i=1}^{3} \frac{\partial \alpha_m}{\partial \xi_i} \frac{\partial \xi_i}{\partial x} \tag{B.12}$$

$\partial \xi_i / \partial x$ is a constant and can be written as

$$\frac{\partial \xi_i}{\partial x} = \frac{y_{i+1} - y_{i-1}}{2A} = \frac{b_i}{2A} \tag{B.13}$$

and likewise, the y-directed derivative can be written as

$$\frac{\partial \xi_i}{\partial y} = \frac{x_{i+1} - x_{i-1}}{2A} = \frac{c_i}{2A} \tag{B.14}$$

hence the derivative of the polynomial is now expressed with respect to simplex coordinates. It remains to calculate the **D** matrix such that

$$\frac{\partial \alpha_m}{\partial \xi_i} = \sum_k D_{mk}^{(i)} \alpha_k \tag{B.15}$$

the elements of **D** are found by performing the formal differentiation of the basis function with respect to a given simplex coordinate at every nodal point *P*. e.g.

$$D_{mk}^{(i)} = \frac{\partial \alpha_m}{\partial \xi_i}\bigg|_{P_k}, \tag{B.16}$$

therefore to evaluate an *x*-directed derivative it is necessary to piece together (B.14) and (B.15) as follows

$$\begin{aligned} \frac{\partial \psi}{\partial x} &= \sum_{m=1}^{M} \psi_m \frac{\partial \alpha_m}{\partial x}, \\ &= \sum_{m=1}^{M} \psi_m \sum_{i=1}^{3} \frac{b_i}{2A} \frac{\partial \alpha_m}{\partial \xi_i}, \\ &= \sum_{m=1}^{M} \psi_m \sum_{i=1}^{3} \frac{b_i}{2A} \sum_k D_{mk}^{(i)} \alpha_k, \end{aligned} \tag{B.17}$$

this can be simplified into matrix form

$$\Psi_{(x)} = \sum_{i=1}^{3} \left(\frac{b_i}{2A} \mathbf{D}^{(i)T} \right) \Psi. \tag{B.18}$$

B.5 Integration in Simplex Coordinates

Deriving the elemental equations involves integration of the basis functions. The use of simplex coordinates allows the use of integration formulae to perform this calculation. It is necessary to

evaluate the definite integral

$$I(i,j,k) = \int \xi_1^i \xi_2^j \xi_3^k \frac{d\Omega}{A}. \tag{B.19}$$

Providing the Jacobian of the coordinate transformation allows the area element to be written in whatever coordinates that may be convenient

$$d\xi_1 d\xi_2 = \frac{\partial(\xi_1,\xi_2)}{\partial(x,y)} dxdy \tag{B.20}$$

2D simplex coordinates are related to Cartesian coordinates via the following equations

$$\begin{aligned} \xi_1 &= (a_1 + b_1 x + c_1 y)/2A \\ \xi_2 &= (a_2 + b_2 x + c_2 y)/2A \end{aligned} \tag{B.21}$$

Where A is the simplex area, the Jacobian can be evaluated thus

$$\frac{\partial(\xi_1,\xi_2)}{\partial(x,y)} = \left(\frac{1}{2A}\right)^2 \begin{vmatrix} b_1 & c_1 \\ b_2 & c_2 \end{vmatrix} = \frac{1}{2A}. \tag{B.22}$$

The integral *I(I,j,k)* may therefore be written as an iterated integral

$$I(i,j,k) = 2\int_0^1 \int_0^{1-\xi_1} \xi_1^i \xi_2^{j+1} (1-\xi_1-\xi_2)^k \, d\xi_2 d\xi_1 \, . \tag{B.23}$$

Integrating by parts, one obtains

$$I(i,j,k) = \frac{2k}{j+1} \int_0^1 \int_0^{1-\xi_1} \xi_1^i \xi_2^{j+1} (1-\xi_1-\xi_2)^{k-1} \, d\xi_2 d\xi_1 \, . \tag{B.24}$$

Therefore

$$I(i,j,k) = \frac{j!k!}{(j+k)!} I(i,j+1,k-1)\,. \tag{B.25}$$

Repeated application of (B.25) results in

$$I(i,j,k) = \frac{j!k!}{(j+k)!} I(i,j+k,0)\,, \tag{B.26}$$

and

$$I(i,j,k) = \frac{i!\,j!k!}{(i+j+k)!} I(0,i+j+k,0)\,. \tag{B.27}$$

But only one of the simplex coordinates appears in the integral $I(0,i+j+k,0)$. Evaluation is therefore straightforward, yielding

$$I(i,j,k) = \frac{i!\,j!k!2!}{(i+j+k+2)!} \tag{B.28}$$

The method extends to three dimensions with tetrahedral elements with the addition of a fourth simplex coordinate and substituting 2! for 3! (2! in the above equation can effectively be replaced by $d!$ where d is the dimensionality), i.e.

$$\int \xi_1^i \xi_2^j \xi_3^k \xi_4^l dV = \frac{i!\,j!k!l!3!}{(i+j+k+l+3)!} V\,. \tag{B.29}$$

Appendix C: 2D Elemental Matrices

C.1 Derivation of $\int_\Omega \alpha_m \alpha_n d\Omega$

It was shown in chapter 2.2 how to formulate the interpolation polynomials in terms of simplex coordinates. Appendix B.5 demonstrated how to compute the integral of simplex coordinates. Combining these two techniques gives all the tools necessary to compute the **T** (or metric) matrix. For example, in two dimensions, the **T** matrix for a triangular element of order 1 can be computed as follows

$$T_{mn} = \int \alpha_m \cdot \alpha_n d\Omega . \tag{C.1}$$

For 1st order the interpolation functions are equal to the simplex coordinates,

$$\alpha_i = \xi_i , \tag{C.2}$$

hence,

$$\int \alpha_m \alpha_n d\Omega = \int \xi_m \xi_n d\Omega . \tag{C.3}$$

From (B.28) we know that

$$\int \xi_1^i \xi_2^j \xi_3^k \frac{d\Omega}{A} = \frac{i!\, j!\, k!\, 2!}{(i+j+k+2)!}, \tag{C.4}$$

therefore the 1st element in the matrix can be calculated as

$$T_{11} = \int \alpha_1 \alpha_1 d\Omega = \int \xi_1^{\,2} d\Omega = \frac{2! \times 2!}{(2+2)!} = \frac{1}{6}, \tag{C.5}$$

and the 2nd

$$T_{12} = \int \alpha_1 \alpha_2 d\Omega = \int \xi_1 \xi_2 d\Omega = \frac{1! \times 1! \times 2!}{(1+1+2)!} = \frac{1}{12}. \tag{C.6}$$

The remaining elements of **T** can be calculated in the same fashion, the resulting matrix being as follows

$$\mathbf{T} = \frac{1}{12}\begin{bmatrix} 2 & 1 & 1 \\ 1 & 2 & 1 \\ 1 & 1 & 2 \end{bmatrix}. \tag{C.7}$$

It is important to note that the integral is independent of element size or shape as it is expressed purely in simplex coordinates. Therefore, **T** matrices for various interpolation orders need only be computed once. It is for this reason that FEMLIB stores the **T** matrices in tabulated form in a data-file.

C.2 Derivation of $\int_\Omega \nabla \alpha_m . \nabla \alpha_n d\Omega$

The **S** or Dirichlet matrix is defined as the following integral

$$S_{mn} = \int \nabla \alpha_m \cdot \nabla \alpha_n d\Omega \tag{C.8}$$

The integrand can be written out in terms of Cartesian coordinates

$$S_{mn} = \int \left(\frac{\partial \alpha_m}{\partial x}\frac{\partial \alpha_n}{\partial x} + \frac{\partial \alpha_m}{\partial y}\frac{\partial \alpha_n}{\partial y} \right) d\Omega \tag{C.9}$$

and using the chain-rule of differentiation the partial derivative of the basis functions with respect to x can be recast as

$$\frac{\partial \alpha_m}{\partial x} = \sum_{i=1}^{3} \frac{\partial \alpha_m}{\partial \xi_i}\frac{\partial \xi_i}{\partial x} \tag{C.10}$$

the derivative of the simplex coordinate can be expressed in geometrical terms, thus

$$\frac{\partial \xi_i}{\partial x} = \frac{y_{i+1} - y_{i-1}}{2A} = \frac{b_i}{2A} \tag{C.11}$$

combining (C.10) and (C.11) adding the derivatives with respect to the y component allows (C.9) to be stated in terms of simplex coordinates

$$S_{mn} = \frac{1}{4A^2} \sum_i \sum_j (b_i b_j + c_i c_j) \int \frac{\partial \alpha_m}{\partial \xi_i} \frac{\partial \alpha_n}{\partial \xi_j} d\Omega \tag{C.12}$$

The integral above can be evaluated by using the differentiation matrices as described previously in Appendix B.4.

$$\int \frac{\partial \alpha_m}{\partial \xi_i} \frac{\partial \alpha_n}{\partial \xi_j} d\Omega = \sum_k \sum_l D_{mk}^{(i)} \left(\int \alpha_k \alpha_l \right) D_{nl}^{(j)} \tag{C.13}$$

The bracketed quantity is the **T** matrix, hence **S** can be expressed as

$$\mathbf{S} = \frac{1}{4A} \sum_i \sum_j (b_i b_j + c_i c_j) \mathbf{D}^{(i)} \mathbf{T} \mathbf{D}^{(j)T} \tag{C.14}$$

The double summation can be reduced to a single if the following identities are used

$$b_i b_j + c_i c_j = -2A \cot \theta_k \qquad i \neq j \tag{C.15}$$

$$b_i^2 + c_i^2 = -2A(\cot \theta_j + \cot \theta_k) \tag{C.16}$$

The proof of these identities can be found in (Silvester and Ferrari 1996), p.458.

Substituting (C.15) and (C.16), expanding then collecting terms, the double summation is reduced to a single summation, thus

$$S_{mn} = \sum_{k=1}^{3} \cot \theta_k \int \left(\frac{\partial \alpha_m}{\partial \xi_{k+1}} - \frac{\partial \alpha_m}{\partial \xi_{k-1}} \right) \left(\frac{\partial \alpha_n}{\partial \xi_{k+1}} - \frac{\partial \alpha_n}{\partial \xi_{k-1}} \right) \frac{d\Omega}{2A} \tag{C.17}$$

the integral above is dimensionless involving quantities expressed in terms of simplex coordinates. Therefore, **S** can be written as

$$S_{mn} = \sum_{k=1}^{3} Q_{mn}^{(k)} \cot\theta_k \tag{C.18}$$

where **Q** is defined as

$$Q_{mn}^{(k)} = \frac{1}{2}\sum_i \sum_j \left(D_{mi}^{(k+1)} - D_{mi}^{(k-1)}\right) T_{ij} \left(D_{nj}^{(k+1)} - D_{nj}^{(k-1)}\right) \tag{C.19}$$

or in matrix form

$$\mathbf{Q}^{(k)} = \frac{1}{2}\left(\mathbf{D}^{(k+1)} - \mathbf{D}^{(k-1)}\right) \mathbf{T} \left(\mathbf{D}^{(k+1)} - \mathbf{D}^{(k-1)}\right) \tag{C.20}$$

C.3 Derivation of $\int_\Omega \alpha_m \nabla \alpha_n d\Omega$

The derivation of this elemental matrix is performed as follows:

$$P_{mn} = \int \alpha_m \nabla \alpha_n d\Omega \tag{C.21}$$

the integral is split into its Cartesian components

$$P_{mn} = \int \alpha_m \mathbf{i} \frac{\partial \alpha_n}{\partial x} + \alpha_m \mathbf{j} \frac{\partial \alpha_n}{\partial y} d\Omega \tag{C.22}$$

the derivative of the basis functions can be restated using the chain rule, hence allowing the derivative to be expressed with respect to a simplex coordinate multiplied by a value based purely on the geometry of the element

$$\frac{\partial \alpha_n}{\partial x} = \frac{\partial \alpha_n}{\partial \xi_i}\frac{\partial \xi_i}{\partial x} = \frac{\partial \alpha_n}{\partial \xi_i}\frac{b_i}{2A} \tag{C.23}$$

the equivalent process for the y-directed derivative

$$\frac{\partial \alpha_n}{\partial y} = \frac{\partial \alpha_n}{\partial \xi_i}\frac{\partial \xi_i}{\partial y} = \frac{\partial \alpha_n}{\partial \xi_i}\frac{c_i}{2A} \tag{C.24}$$

differentiating a basis function with respect to a simplex coordinate is equivalent to the sum over k of the product of the **D** matrix and the basis function

$$\frac{\partial \alpha_m}{\partial \xi_i} = \sum_k D_{mk}^{(i)} \alpha_k \tag{C.25}$$

bringing this together, (C.22) can be expressed as

$$P_{mn} = \int \alpha_m \mathbf{i} \frac{\partial \alpha_n}{\partial \xi_i}\frac{b_i}{2A} + \alpha_m \mathbf{j} \frac{\partial \alpha_n}{\partial \xi_i}\frac{c_i}{2A} d\Omega \tag{C.26}$$

substituting (C.25) into the equation gives

$$P_{mn} = \int \alpha_m \mathbf{i} \sum_{k=1}^{3} D_{nk}^{(i)} \alpha_k \frac{b_i}{2A} + \alpha_m \mathbf{j} \sum_{k=1}^{3} D_{nk}^{(i)} \alpha_k \frac{c_i}{2A} d\Omega \tag{C.27}$$

this can be split into two separate integrals

$$P_{mn} = \int \alpha_m \mathbf{i} \sum_{k=1}^{3} D_{nk}^{(i)} \alpha_k \frac{b_i}{2A} d\Omega + \int \alpha_m \mathbf{j} \sum_{k=1}^{3} D_{nk}^{(i)} \alpha_k \frac{c_i}{2A} d\Omega \tag{C.28}$$

$\mathbf{i}\sum_{k=1}^{3} D_{nk}^{(i)} \frac{b_i}{2A}$ can commute outside the integral as it is simply a constant; to give

$$P_{mn} = \mathbf{i}\sum_{k=1}^{3} D_{nk}^{(i)} \frac{b_i}{2A} \int \alpha_m \alpha_k d\Omega + \mathbf{j}\sum_{k=1}^{3} D_{nk}^{(i)} \frac{c_i}{2A} \int \alpha_m \alpha_k d\Omega \qquad \text{(C.29)}$$

$\int \alpha_m \alpha_k d\Omega$ is a common factor in both the left and right parts of the above summation, hence (C.29) can be reduced to

$$P_{mn} = \left(\mathbf{i}\sum_{k=1}^{3} D_{nk}^{(i)} \frac{b_i}{2A} + \mathbf{j}\sum_{k=1}^{3} D_{nk}^{(i)} \frac{c_i}{2A} \right) \int \alpha_m \alpha_k d\Omega \qquad \text{(C.30)}$$

recognising that $\int \alpha_m \alpha_k d\Omega$ is simply the **T** matrix the equation can be rewritten as (C.32)

$$T_{mk} = \int \alpha_m \alpha_k d\Omega \qquad \text{(C.31)}$$

$$P_{mn} = \left(\mathbf{i}\sum_{k=1}^{3} D_{nk}^{(i)} \frac{b_i}{2A} + \mathbf{j}\sum_{k=1}^{3} D_{nk}^{(i)} \frac{c_i}{2A} \right) T_{mk} \qquad \text{(C.32)}$$

dropping the explicit $\sum$ notation and switching to Einstein's summation convention gives

$$P_{mn} = \left(\mathbf{i} D_{nk}^{(i)} \frac{b_i}{2A} + \mathbf{j} D_{nk}^{(i)} \frac{c_i}{2A} \right) T_{mk} \qquad \text{(C.33)}$$

therefore in matrix form

$$\mathbf{P} = \mathbf{i}\mathbf{D}^{(i)}\mathbf{T}\frac{b_i}{2A} + \mathbf{j}\mathbf{D}^{(i)}\mathbf{T}\frac{c_i}{2A} \qquad \text{(C.34)}$$

this is then easily computed from the already defined **D** and **T** matrices and the element geometry.

Appendix D: Analytical Solution in Free-space

Working from the scalar form of Maxwell's equations, the permittivity coefficient can be removed (ε of air equals 1)

$$-\nabla^2\psi = \lambda\psi \tag{D.1}$$

As stated in chapter 2.3, Floquet-Bloch theory permits the following expression

$$\psi = e^{i\mathbf{k}\mathbf{x}}u(x) \tag{D.2}$$

Where *u(x)* is a function with the periodicity of the crystal lattice. $e^{i\mathbf{G}\cdot\mathbf{x}}$ has the required periodicity, where **G** represents a reciprocal lattice point, therefore

$$u(x) = e^{i\mathbf{G}\cdot\mathbf{x}} \tag{D.3}$$

Combining (D.2) and (D.3) and the summing and factorising the indices gives

$$\psi = e^{i\mathbf{k}\cdot\mathbf{x}} \cdot e^{iG\cdot\mathbf{x}} = e^{i(\mathbf{G}+\mathbf{k})\cdot\mathbf{x}} \tag{D.4}$$

Differentiating the wave function twice gives

$$\nabla^2 e^{i(\mathbf{G}+\mathbf{k})\cdot\mathbf{x}} = \frac{d^2}{dx^2}e^{i(\mathbf{G}+\mathbf{k})\cdot\mathbf{x}} = \left[i(\mathbf{G}+\mathbf{k})\right]^2 e^{i(\mathbf{G}+\mathbf{k})\cdot\mathbf{x}} \tag{D.5}$$

This can then be substituted back into (D.1) as follows

$$\left[i(\mathbf{G}+\mathbf{k})\right]^2 e^{i(\mathbf{G}+\mathbf{k})\cdot\mathbf{x}} = \lambda e^{i(\mathbf{G}+\mathbf{k})\cdot\mathbf{x}} \tag{D.6}$$

The $e^{i(\mathbf{G}+\mathbf{k})\cdot\mathbf{x}}$ terms on both sides of the equation cancel to give the analytical solution

$$\lambda = \left[i(\mathbf{G}+\mathbf{k})\right]^2 = (\mathbf{G}+\mathbf{k})^2 \tag{D.7}$$

Appendix E: The Levi-Civita Tensor

The Levi-Civita Tensor (totally anti-symmetric tensor) is defined as follows

$$\varepsilon^{ijk} = \begin{cases} +1 & \text{if } ijk \text{ are different and in order (cyclic permutation)} \\ -1 & \text{if } ijk \text{ are different and in order (anti-cyclic permutation)} \\ 0 & \text{if } i = j,\ i = k \text{ or } k = j \end{cases} \qquad \text{(E.1)}$$

It can be used to represent the determinant of a set of vectors as shown below.

$$\varepsilon^{ijk}\mathbf{a}_i\mathbf{b}_j\mathbf{c}_k = \begin{vmatrix} a_1 & a_2 & a_3 \\ b_1 & b_2 & b_3 \\ c_1 & c_2 & c_3 \end{vmatrix} \qquad \text{(E.2)}$$

Appendix F: 3D Elemental Matrices

In order to evaluate these integrals firstly we restate the linear Lagrange interpolation functions in their Cartesian form.

$$L_i = \frac{1}{6V}\left(a_i + b_i x + c_i y + d_i z\right) = \frac{1}{6V}\left(a_i + c_i^j x_j\right) \tag{F.1}$$

The equation on the right uses Einstein's summation convention over j with the vector, $\mathbf{c}$, representing the b, c and d coefficients. The grad of L can be written as follows.

$$\underline{\nabla} L_i = \frac{1}{6V}\mathbf{c}_i \tag{F.2}$$

Combining equations (F.1) and (F.2) gives an alternate representation of the vector basis function. It is important to note that i now represents the i^{th} edge, with i_1 and i_2 representing the vertices at either end of that edge (in (F.1) i represented a vertex). Using equation (F.1) and (F.2) in (2.23) yields:

$$\begin{aligned}\mathbf{N}_i &= l_i\left(L_{i_1}\underline{\nabla} L_{1_2} - L_{i_2}\underline{\nabla} L_{1_1}\right) = \frac{1}{6V} l_i\left(L_{i_1}\mathbf{c}_{1_2} - L_{i_2}\mathbf{c}_{1_1}\right) \\ &= \frac{1}{6V} l_i\left[\frac{1}{6V}\left(a_{i_1} + c_{i_1}{}^j x_j\right)\left(\mathbf{c}_{i_2}\right) - \frac{1}{6V}\left(a_{i_2} + c_{i_2}{}^j x_j\right)\left(\mathbf{c}_{i_1}\right)\right].\end{aligned} \tag{F.3}$$

The curl of the vector basis function can now be evaluated analytically as follows, where ε represents the Levi-Civita tensor (see Appendix E:) and $\mathbf{e}$ represents the unit vector in each dimension. The $1/6V$ term is taken outside the brackets to give $1/(6V)^2$ and the partial derivative is taken with respect to ∂_b.

$$\begin{aligned}\underline{\nabla}\times\mathbf{N}_i &= \frac{l_i}{(6V)^2}\varepsilon^{abc}\hat{\mathbf{e}}\partial_b\left[\left(a_{i_1} + c_{i_1}{}^j x_j\right)\left(c_{i_2}{}^c\right) - \left(a_{i_2} + c_{i_2}{}^j x_j\right)\left(c_{i_1}{}^c\right)\right] \\ &= \frac{l_i}{(6V)^2}\varepsilon^{abc}\hat{e}_a\left[c_{i_1}{}^b c_{i_2}{}^c - c_{i_2}{}^b c_{i_1}{}^c\right]\end{aligned} \tag{F.4}$$

This equation can be reduced to:

$$= \frac{2l_i}{(6V)^2}\mathbf{c}_{i_1} \times \mathbf{c}_{i_2} \equiv \frac{2l_i}{(6V)^2}\mathbf{X}_i \qquad \text{(F.5)}$$

$$\mathbf{X}_i \equiv \mathbf{c}_{i_1} \times \mathbf{c}_{i_2}$$

The last step of the derivation is based on the following equality.

$$\varepsilon^{abc}\hat{\mathbf{e}}_a\left[c_{i_1}{}^b c_{i_2}{}^c - c_{i_2}c_{i_1}{}^c\right] = 2\left(\mathbf{c}_{i_1} \times \mathbf{c}_{i_2}\right) \qquad \text{(F.6)}$$

This can be proven by expanding the left hand side of (F.6) for cyclic permutations of *a*, *b* and *c*.

$$\begin{vmatrix} \hat{\mathbf{e}}^1 & \hat{\mathbf{e}}^2 & \hat{\mathbf{e}}^3 \\ c_{i_1}{}^1 & c_{i_1}{}^2 & c_{i_1}{}^3 \\ c_{i_2}{}^1 & c_{i_2}{}^2 & c_{i_2}{}^3 \end{vmatrix} = \begin{matrix} \hat{\mathbf{e}}^1\left(c_{i_1}{}^2 c_{i_2}{}^3 - c_{i_1}{}^3 c_{i_2}{}^2\right) \\ +\hat{\mathbf{e}}^2\left(c_{i_1}{}^3 c_{i_2}{}^1 - c_{i_1}{}^1 c_{i_2}{}^3\right) \\ +\hat{\mathbf{e}}^3\left(c_{i_1}{}^1 c_{i_2}{}^2 - c_{i_1}{}^2 c_{i_2}{}^1\right) \end{matrix} \qquad \text{(F.7)}$$

which is clearly equal to $\mathbf{c}_{i_1} \times \mathbf{c}_{i_2}$. The anti-cyclic permutations of the tensor yield the same result hence the factor of 2 is introduced.

F.1 Derivation of $\int_\Omega (\nabla \times \mathbf{N}_i) \cdot (\nabla \times \mathbf{N}_j)\, d\Omega$

The body of the integral can be equated to:

$$S_{ij} = \left(\underline{\nabla} \times \mathbf{N}_i\right) \cdot \left(\underline{\nabla} \times \mathbf{N}_j\right) = \frac{4l_i l_j}{(6V)^4}\mathbf{X}_i \cdot \mathbf{X}_j . \qquad \text{(F.8)}$$

Computing the integral with respect to the element volume yields equation (F.9). Using this a six by six elemental matrix is computed with the subscripts *i* and *j* corresponding to the element edge numbers.

$$S_{ij} = \iiint_V (\underline{\nabla} \times \mathbf{N}_i) \cdot (\underline{\nabla} \times \mathbf{N}_j) dV = \frac{4 l_i l_j V}{(6V)^4} \mathbf{X}_i \cdot \mathbf{X}_j \qquad \text{(F.9)}$$

F.2 Derivation of $\int_\Omega \mathbf{N}_i \cdot \mathbf{N}_j \, d\Omega$

The body of the **T** matrix integral can be expressed as follows.

$$T_{ij} = N_i \cdot N_j = \frac{l_i l_j}{(6V)^2} \begin{pmatrix} L_{i_1} L_{j_1} \mathbf{c}_{i_2} \cdot \mathbf{c}_{j_2} \\ - L_{i_1} L_{j_2} \mathbf{c}_{i_2} \cdot \mathbf{c}_{j_1} \\ - L_{i_2} L_{j_1} \mathbf{c}_{i_1} \cdot \mathbf{c}_{j_2} \\ + L_{i_2} L_{j_2} \mathbf{c}_{i_1} \cdot \mathbf{c}_{j_1} \end{pmatrix} \qquad \text{(F.10)}$$

Using the integration formula as described in chapter B.5 the linear interpolation functions can be integrated to give,

$$\iiint_V L^2 dV = \frac{V}{10} \quad \text{and} \quad \iiint_V L_1 L_2 dV = \frac{V}{20} \qquad \text{(F.11)}$$

Hence T_{ij} can be computed as follows:

$$\iiint_V \mathbf{N}_i \cdot \mathbf{N}_j dV = \frac{l_i l_j V}{20(6V)^2} \begin{bmatrix} \left(1 + \delta_{j_1}^{i_1}\right) \mathbf{c}_{i_2} \cdot \mathbf{c}_{j_2} \\ - \left(1 + \delta_{j_2}^{i_1}\right) \mathbf{c}_{i_2} \cdot \mathbf{c}_{j_1} \\ - \left(1 + \delta_{j_1}^{i_2}\right) \mathbf{c}_{i_1} \cdot \mathbf{c}_{j_2} \\ + \left(1 + \delta_{j_2}^{i_2}\right) \mathbf{c}_{i_1} \cdot \mathbf{c}_{j_1} \end{bmatrix} \qquad \text{(F.12)}$$

F.3 Derivation of $\int_\Omega (\mathbf{N}_i \times \nabla \times \mathbf{N}_j) - (\mathbf{N}_j \times \nabla \times \mathbf{N}_i) d\Omega$

The P_{ij} matrix is formulated and integrated as shown in equations (F.13) through to (F.14).

$$P_{ij} = (\mathbf{N}_i \times \underline{\nabla} \times \mathbf{N}_j) - (\mathbf{N}_j \times \underline{\nabla} \times \mathbf{N}_i) \qquad \text{(F.13)}$$

$$= \frac{2l_i l_j}{(6V)^3}\left[\left(L_{i_1} c_{i_2} - L_{i_2} c_{i_1}\right) \times X_j - \left(L_{j_1} c_{j_2} - Ljc_{j_1}\right) \times X_i\right]$$

$$\iiint_V \left(\mathbf{N}_i \times \underline{\nabla} \times \mathbf{N}_j\right) - \left(\mathbf{N}_j \times \underline{\nabla} \times \mathbf{N}_i\right) dV$$

$$= \frac{l_u l_j V}{10(6V)^3}\left[\left(c_{i_2} - c_{i_1}\right) \times X_j - \left(c_{j_2} - c_{j_1}\right) \times X_i\right] \qquad \text{(F.14)}$$

$$= \frac{l_u l_j V}{10(6V)^3}\left[D_i \times X_j - D_j \times X_i\right] \quad \text{where} \quad D_i \equiv c_{i_2} - c_{i_1}$$

F.4 Derivation of $\int_\Omega (\mathbf{k} \cdot \mathbf{N}_i)(\mathbf{k} \cdot \mathbf{N}_j) d\Omega$

The fourth elemental matrix, **J**, is derived via the following steps:

$$let \quad I_{ij} = \int_\Omega (\mathbf{k} \cdot \mathbf{N}_i)(\mathbf{k} \cdot \mathbf{N}_j) d\Omega \qquad \text{(F.15)}$$

Substituting the Lagrange interpolation function formulation of the vector interpolation functions gives:

$$= \int_\Omega \left(\mathbf{k} \cdot l_i \left(L_{i_1} \nabla L_{i_2} - L_{i_2} \nabla L_{i_1}\right)\right)\left(\mathbf{k} \cdot l_j \left(L_{j_1} \nabla L_{j_2} - L_{j_2} \nabla L_{j_1}\right)\right) d\Omega \qquad \text{(F.16)}$$

The grad L terms are replaced with the **c** notation:

$$= \int_\Omega \left[\mathbf{k} \cdot l_i \left(L_{i_1} \mathbf{c}_{i_2} - L_{i_2} \mathbf{c}_{i_1}\right)\right]\left[\mathbf{k} \cdot l_j \left(L_{j_1} \mathbf{c}_{j_2} - L_{j_2} \mathbf{c}_{j_1}\right)\right] \qquad \text{(F.17)}$$

Multiplying out the values within the parenthesis allows the constant factors to commute outside the integral. This leaves integrals in terms of only the Lagrange interpolation functions:

$$= \begin{array}{l} l_i l_j \left(\mathbf{k}\cdot\mathbf{c}_{i_2}\right)\left(\mathbf{k}\cdot\mathbf{c}_{j_2}\right)\int_\Omega L_{i_1} L_{j_1}\, d\Omega \\ -l_i l_j \left(\mathbf{k}\cdot\mathbf{c}_{i_2}\right)\left(\mathbf{k}\cdot\mathbf{c}_{j_1}\right)\int_\Omega L_{i_1} L_{j_2}\, d\Omega \\ -l_i l_j \left(\mathbf{k}\cdot\mathbf{c}_{i_1}\right)\left(\mathbf{k}\cdot\mathbf{c}_{j_2}\right)\int_\Omega L_{i_2} L_{j_1}\, d\Omega \\ +l_i l_j \left(\mathbf{k}\cdot\mathbf{c}_{i_1}\right)\left(\mathbf{k}\cdot\mathbf{c}_{j_2}\right)\int_\Omega L_{i_2} L_{j_2}\, d\Omega \end{array} \tag{F.18}$$

These integrals can be evaluated numerically using the formula presented in Appendix B.5 to give:

$$I_{ij} = \frac{V l_i l_j}{20}\begin{bmatrix} \left(\mathbf{k}\cdot\mathbf{c}_{i_2}\right)\left(\mathbf{k}\cdot\mathbf{c}_{j_2}\right)\left(1+\delta_{j_1}^{i_1}\right) \\ -\left(\mathbf{k}\cdot\mathbf{c}_{i_2}\right)\left(\mathbf{k}\cdot\mathbf{c}_{j_1}\right)\left(1+\delta_{j_2}^{i_1}\right) \\ -\left(\mathbf{k}\cdot\mathbf{c}_{i_1}\right)\left(\mathbf{k}\cdot\mathbf{c}_{j_2}\right)\left(1+\delta_{j_1}^{i_2}\right) \\ +\left(\mathbf{k}\cdot\mathbf{c}_{i_1}\right)\left(\mathbf{k}\cdot\mathbf{c}_{j_2}\right)\left(1+\delta_{j_2}^{i_2}\right) \end{bmatrix} \tag{F.19}$$

Thus we can compute the matrix, **I**, for each element. However, having **k** as a term within the matrix necessitates re-computation of the elemental matrices for each **k** step. This is clearly inefficient, and avoidable if one judiciously rearranges the initial equation as shown in equation (F.20).

$$\left(\mathbf{a}\cdot\mathbf{b}\right)\left(\mathbf{a}\cdot\mathbf{c}\right) = a_i b_i a_j c_j = a_i\left(b_i c_j\right)a_j = a_i\left(b\otimes c\right)_{ij} a_j = \mathbf{a}^T\mathbf{J}\,\mathbf{a} \tag{F.20}$$

Therefore we can restate **I** as:

$$\mathbf{I} = \mathbf{k}^T\mathbf{J}\,\mathbf{k}\,, \tag{F.21}$$

where:

$$\mathbf{J} = \mathbf{b}\otimes\mathbf{c} \tag{F.22}$$

This formulation allows the elemental matrix, **J**, to be computed only once. **I** can subsequently be computed by simply post-multiplying **J** by **k** and its transpose. **J** can be explicitly stated as:

$$J_{ij} = \frac{V l_i l_j}{20}\begin{bmatrix} \mathbf{c}_{i_2}\otimes\mathbf{c}_{j_2}\left(1+\delta_{j_1}^{i_1}\right) \\ -\mathbf{c}_{i_1}\otimes\mathbf{c}_{j_2}\left(1+\delta_{j_1}^{i_2}\right) \\ -\mathbf{c}_{i_2}\otimes\mathbf{c}_{j_1}\left(1+\delta_{j_2}^{i_1}\right) \\ +\mathbf{c}_{i_1}\otimes\mathbf{c}_{j_1}\left(1+\delta_{j_2}^{i_2}\right) \end{bmatrix} \tag{F.23}$$

Note that the operation, $\mathbf{c}_1\otimes\mathbf{c}_2$, results in a matrix, hence **J** is a matrix-valued matrix or matrix of matrices.

Appendix G: FEMLIB Class Diagrams

A short description if each class including its data members and methods, laid out as shown below

Class Name
Encapsulated Data: • Etc.
Encapsulated Methods: • Etc.

Element
• Element geometry data • Element material data
• Elementary Dirichlet, metric and Ben matrix calculation • Specification of interpolation polynomial order • Mapping of local and global node numbers

Side
• Reference to sides element and vertex objects • Boundary marker • Node numbers
• Generate global node numbers • Map local to global node numbers

Vertex
• Position object (stores Cartesian coordinate of vertex) • Node number • Boundary marker

• Specification of interpolation polynomial order • Generation of global node numbers • Mapping of local to global node numbers • Boolean equality operator to compare two vertex objects

Position
• Cartesian coordinate (stored as a vector of floating point numbers) • Tolerance, used in relation to the equality operator
• Addition, subtraction, multiplication, division and equality operators • Specification of the tolerance value

Mesh
• References to element, side and vertex objects that comprise the mesh • Number of nodes • Interpolation order • Nodes per element
• Set the interpolation order • Assemble the global matrices for the mesh

MeshDoc
• References to element , side and vertex objects that comprise the mesh
• Read in mesh data from files • Map mesh geometry on to a torus, e.g. enforce periodic boundary conditions

Matrix
• Matrix Elements • Number of rows and columns
• Element extraction via *(x,y)* row, column format • Matrix multiplication, division, addition and subtraction • Similarity transform • Cholesky decomposition • Reduction to tridiagonal form

Zonepath
• Definition of the path of the quasimomentum vector k around the Brillouin zone
• Specification of the number of legs the path has • Specification of the step size for each leg • Calculation of the k vector at each position along the path